Clasificación y cuantificación basada en aprendizaje automático de aceros de dos fases

Estudiante: Lautaro Elbio Gonzalez Santucho
(gonzalezsantucholautaro@gmail.com)

Director: Juan Ignacio Moran
(jmoran@fi.mdp.edu.ar)

Co-Director: Björn Ivo Bachmann
(bjoernivo.bachmann@uni-saarland.de)

Proyecto final para optar al grado de Ingeniero en Materiales

Universidad Nacional de Mar del Plata
Facultad de Ingeniería
Departamento de Ingeniería en Materiales

Universität des Saarlandes

Mar del Plata, 09 de agosto de 2024

Clasificación y cuantificación basada en aprendizaje automático de aceros de dos fases

Estudiante: Lautaro Elbio Gonzalez Santucho
(gonzalezsantucholautaro@gmail.com)

Director: Juan Ignacio Moran
(jmoran@fi.mdp.edu.ar)

Co-Director: Björn Ivo Bachmann
(bjoernivo.bachmann@uni-saarland.de)

Proyecto final para optar al grado de Ingeniero en Materiales

Universidad Nacional de Mar del Plata
Facultad de Ingeniería
Departamento de Ingeniería en Materiales

Universität des Saarlandes

Mar del Plata, 09 de agosto de 2024

This project is the result of a collaboration between the National University of Mar del Plata in Argentina, the University of Saarland in Germany, and the AG der Dillinger Hüttenwerke located in Germany.

Confidentiality clause

The present work is to be treated as confidential due to an agreement between the Aktien-Gesellschaft der Dillinger Hüttenwerke and the author. It may not be disclosed without explicit permission. The duration is five years, starting from the date mentioned here.

_____	_____
Lautaro Elbio Gonzalez Santucho	Date, place

Acknowledgments

I want to express my deepest gratitude to all the people who made it possible for me to carry on this project:

Björn Bachmann, my advisor in Germany, for his patience, guidance and trust from the first day of the project.

Dr. Juan Moran, my director in Argentina, for his support and guidance in the final stages of writing and preparation for the defense.

Der Aktiengesellschaft der Dillinger Hütte for supplying me with the equipment and samples required for the project, specially Dr. Thorsten Staudt for his supervision and encouragement during my internship at the company.

The chair of Functional Materials at Saarland University for providing me with the first insights into the world of machine learning.

Mar del Plata National University and their excellent people for providing me with the tools necessary to carry on this project during my years of education.

The coordinators of the IDEAR exchange program Dr. Flavio Soldera, Dr. Silvia Simison and Dr. Maria Andrea Camerucci who made it possible for me to have the outstanding experience of studying abroad.

Roberto Rocca Foundation for their generous scholarship support throughout my studies.

My colleagues and friends, who have shown unconditional support and understanding throughout my university path, in particular Ivan Buldrini, who made our time in Germany even more enjoyable.

My family, above all my parents Elbio and Andrea, and my siblings Abril and Alejo, for always having my back through the ups and downs of my journey.

This wouldn't have been possible without all of you; this work is as much yours as it is mine.

Thank you!

Contents

Abstract

This project presents an iterative approach for upscaling a machine learning model for microstructural semantic segmentation of two-phase steels light optical micrographs. Several deep learning models have been trained, using a U-NET architecture with DenseNet-201 pretrained weights on ImageNet as backbone.

Metallographic samples from rolled plates have been produced and analyzed in different microscopes to collect data for training and testing, aiming to specifically increase the manageable variance as well as the model's robustness. The results from previous models were then used as masks to train the final one.

The incorporation of a higher variance in the model through different acquisition conditions images resulted in a more robust model, that can consistently segment images at various magnifications, from different microscopes, and taken under suboptimal conditions.

The utilization of previous segmentation results as masks allowed to introduce more data to the training data set. This allowed to minimize the need to produce hand annotated masks, which are time consuming to make and often constitute a bottle neck for model training.

The relevance of these results lies in the possibility to correlate the results from the model (second phase fraction and morphological parameters of the particles) with mechanical properties and manufacturing parameters. Moreover, light optical micrographs are inexpensive, fast to produce and already implemented in quality control at an industrial scale, thus making the implementation of this analysis technique in the industry feasible.

Resumen

En las últimas décadas, se ha observado un cambio de paradigma en el diseño de los aceros. Desplazándose desde un enfoque empírico, donde se buscaba relacionar las propiedades mecánicas con los parámetros de procesamiento, a poner la microestructura un lugar central, como nexo entre el proceso y las propiedades.

En este sentido, el desarrollo de nuevas tecnologías y técnicas de caracterización juega un rol fundamental en el desarrollo de la industria. Con el surgimiento de microestructuras más complejas, la realización de un análisis microestructural cuantitativo consistente y confiable es cada vez más necesario y a la vez más difícil.

Previamente, se han implementado exitosamente modelos de inteligencia artificial para caracterización microestructural. En este trabajo, se han utilizado específicamente redes neuronales convolucionales, un tipo de algoritmo de aprendizaje automático, como herramienta de análisis.

Sin embargo, algunas de las limitaciones actuales están relacionadas a la sensibilidad de los modelos a las condiciones de preparación de las muestras y a los parámetros de adquisición de las imágenes. Técnicas de microscopia correlativa, que combinan la información de diferentes fuentes para asignar la verdad fundamental para el entrenamiento de modelos, han demostrado ser efectivas para conseguir buenos resultados. No obstante, este enfoque requiere de equipamiento costoso y un alto grado de experiencia.

El objetivo de este trabajo es escalar modelos de segmentación y clasificación de micrografías ópticas de aceros de dos fases incorporando muestras de acero de grado industrial. En este sentido, se utilizaron microscopios ópticos para obtener imágenes de muestras atacadas con nital. Las micrografías ópticas de muestras atacadas con nital se emplean actualmente en control de calidad a nivel industrial debido a su sencillez y bajo costo, lo que permite analizar un gran volumen de muestras.

Las muestras utilizadas son de aceros de grado industrial provenientes de la planta de Dillinger Hütte, ubicada en Saarland, Alemania. Esta empresa se especializa en la producción de chapas de acero. Su planta cuenta con altos hornos, colada continua y trenes laminadores, permitiendo así un control integral sobre el proceso de producción del acero. El principal destino de su producción es la fabricación de tuberías, pero sus productos también se utilizan en plataformas de perforación, barcos, puentes, etc.

La gran variedad de grados de acero, producto de distintas combinaciones de aleantes y tratamientos termo mecánicos, genera una complejidad adicional en la microestructura de los productos, que muchas veces dista de las estructuras típicas observadas en bibliografía.

Por este motivo, se realizaron micrografías complementarias con un microscopio electrónico de barrido, cuyo mayor poder de resolución permite una mejor identificación de las fases presentes. Los parámetros de procesamiento y la composición química también fueron tenidos en cuenta al momento de caracterizar manualmente las microestructuras.

Se entrenaron varios modelos de aprendizaje profundo, usando la arquitectura U-NET y los

pesos preentrenados en ImageNet de la arquitectura DenseNet 201 como codificador. Todos los modelos fueron entrenados para segmentar las micrografías ópticas en tres clases: matriz, segunda fase perlítica y segunda fase bainítica/martensítica. La combinación de bainita y martensita en una clase responde a la limitación intrínseca de resolución de la microscopía óptica, que no es suficiente para diferenciar consistentemente estos dos constituyentes, especialmente debido a que ambos pueden estar presentes en la misma muestra a distintas profundidades en el espesor de la plancha.

Los modelos desarrollados son alimentados con micrografías ópticas y producen como resultado una máscara que contiene la clase asignada a cada píxel de la imagen. A partir de esto se puede conocer la naturaleza y porcentaje de la segunda fase y calcular parámetros morfológicos de las partículas.

La caracterización manual de las microestructuras en primera instancia permite elaborar las máscaras necesarias para el entrenamiento de los modelos. Estas mascaras, conocidas como "verdad fundamental" o "ground truth" en inglés, contienen la asignación de clases píxel a píxel de cada micrografía. Este proceso es extremadamente lento, y a menudo constituye un cuello de botella en el desarrollo de modelos de aprendizaje profundo.

Para aumentar la robustez del modelo, es decir, la varianza que es capaz de manejar manteniendo resultados satisfactorios, se tomaron imágenes con varios microscopios y en diferentes condiciones de adquisición (magnificación, tiempo de exposición, apertura, entre otros). Estas variables fueron tenidas en cuenta al momento de analizar el desempeño de los modelos. La elevada varianza es inevitable en los procesos de control de calidad, debido a que intervienen varias personas y equipos y a que se analiza un gran número de muestras.

Se realizaron indentaciones de dureza en diferentes posiciones de la probeta. Cerca de la superficie, a un cuarto del espesor y a la mitad del espesor. Esto responde a dos propósitos. En primer lugar, analizar si es posible establecer correlaciones entre los resultados del modelo y la dureza del material. Y, en segundo lugar, para posibilitar la adquisición de imágenes de la misma región con los diferentes equipos.

El enfoque del trabajo se centró en la mejora iterativa de los modelos, que se dividieron en tres generaciones. En cada iteración, el desempeño de los modelos fue evaluado con imágenes que no habían sido utilizadas durante el entrenamiento, y nuevas máscaras fueron incorporadas al conjunto de entrenamiento. En su mayoria, estas máscaras no fueron realizadas en forma manual, sino que se utilizaron los resultados de generaciones anteriores del modelo para retroalimentar su mejora. De esta forma, se logró reducir al mínimo la necesidad de producir mascaras manualmente, ahorrando tiempo de manera considerable.

El análisis de la primera generación de modelos se centró en la resolución de imagen más adecuada tanto para su entrenamiento como para su funcionamiento. Cabe destacar que debido a restricciones de capacidad computacional y de la disponibilidad de máscaras, las imágenes utilizadas para entrenamiento se dividen en mosaicos. Así, se logra aumentar la cantidad de imágenes disponibles y reducir la capacidad de cómputo necesaria durante el entrenamiento. Durante el funcionamiento, en cambio, las imágenes se procesan completas, aunque deben ser re escaladas debido a la naturaleza de funcionamiento de las redes neuronales. Se observó un mejor desempeño usando un mayor tamaño de mosaico de entrenamiento y una resolución de funcionamiento cercana a la resolución nativa de la cámara de cada microscopio.

También se analizó la posibilidad de incluir un paso de preprocesamiento para corrección de sombras mediante el algoritmo de bola rodante. Sin embargo, el costo computacional de este paso resultó demasiado elevado y las mejoras de desempeño fueron inconsistentes. Por lo tanto, se decidió eliminarlo en las generaciones posteriores.

El desempeño del mejor modelo de esta generación fue satisfactorio en imágenes capturadas bajo condiciones óptimas, pero el reconocimiento de los bordes de los objetos de segunda fase y las partículas pequeñas fue deficiente, así como también su desempeño en imágenes no óptimas. Aun así, de los resultados se pudieron extraer máscaras para el entrenamiento de los modelos de segunda generación.

Se entrenaron dos modelos de segunda generación utilizando mayores tamaños de mosaico. En esta iteración, se observó el punto de equilibrio, con mosaicos de 768 x 768 px, que resultaron en un desempeño superior a los de mayor resolución. Esto puede deberse al menor numero de mosaicos de mayor resolución que se pueden producir a partir de las imágenes, así como también a las limitaciones en la capacidad computacional para procesarlos simultáneamente al entrenar el modelo.

La varianza introducida mediante las máscaras de la anterior generación se tradujo en un mejor desempeño en condiciones no óptimas. Esto permitió incorporar más mascaras para el entrenamiento de la tercera generación de modelos.

El modelo final, de la tercera generación, mostró una nueva mejora de desempeño. Se logró segmentar de manera consistente micrografías de muestras que no habían sido utilizadas durante el entrenamiento tomadas en distintas condiciones.

Aun así, el modelo final todavía cuenta con limitaciones, mostrando un desempeño inferior en micrografías capturadas con una magnificación de 1000x o con bajo contraste. En base a lo observado durante el desarrollo actual, es posible que la incorporación de los resultados del último modelo al conjunto de entrenamiento para un modelo posterior resulte en una mejora adicional del rendimiento.

Los resultados del último modelo se utilizaron para establecer correlaciones entre la fracción de segunda fase y el área promedio de las partículas con la dureza Vickers a lo largo de la sección transversal de las muestras. Se pudo observar la influencia del gradiente de temperatura durante el proceso de enfriamiento y de la segregación en la microestructura y cuantificarlo mediante los resultados obtenidos con el modelo.

La relevancia de estos resultados yace en la posibilidad de correlacionar los resultados del modelo (fracción de segunda fase y parámetros morfológicos de las partículas) con propiedades mecánicas y parámetros de procesamiento. Además, las micrografías ópticas son baratas, fáciles de producir, y ya están implementadas como control de calidad en escala industrial, lo que hace que la implementación de esta técnica de análisis en la industria sea factible.

La implementación de modelos de inteligencia artificial en la ciencia de materiales ya ha probado ser útil en numerosas tareas y aún tiene un gran potencial de desarrollo. Al automatizar el análisis de microestructuras complejas estos modelos también tienen potencial de ser aplicados en la industria, contribuyendo a desarrollar mejores productos a un menor costo.

Chapter 1

Introduction

Steel is a widely used material and has an uncountable amount of applications in different fields, ranging from heavy machinery to jewellery. This is possible because of the equally wide range of properties that can be achieved by introducing different alloying elements and thermomechanical treatments into the steel.

There are over 3500 different grades of steels, that summed up to a production of more than 1800 million tons worldwide only in 2023 [1]. Besides its versatility, the employment of steel for such a wide range of applications is related to its availability, as its main element, iron, is abundant on the earth's crust. Moreover, steel is recyclable and on average, new steel products contain 30 % recycled steel [1].

The development of new technologies and characterization techniques plays a fundamental role in the constant development of the industry. More complex microstructures arise, making reliable and objective microstructural analysis more difficult to achieve with traditional techniques. Furthermore, stricter tolerance margins necessary to fulfil quality standards require to test a large number of samples, making it a costly and time-consuming task.

Another reason that motivates the development of modern microstructural characterization techniques is the paradigm shift in the steel design process. Moving from an empirical approach, where a direct link between the processing steps and the mechanical properties was established, to one where microstructure itself plays a key role, as a link between process and properties. In this context, microstructure engineering is supported by a broad range of technologies, from widely implemented methods such as electron scanning microscopy (SEM) and electron backscatter diffraction (EBSD) to more novel techniques such as atom probe tomography [2], or computational simulations [3].

The rise of artificial intelligence has opened a new world of possibilities in many research fields, and materials science is not the exception. Artificial intelligence models have already been successfully employed for microstructural characterization [4], [5], [6]. It is an emerging technology, with lots of potential applications yet to be discovered.

Microstructural classification and segmentation have already been carried out using artificial intelligence techniques via machine learning models [7], [8]. This sub-field of artificial intelligence focuses on the development of algorithms that mimic the human decision-making process by learning features from data through statistical modelling to predict future values [9]. These efforts aim to provide reliable tools for automatic microstructural analysis. This can save both the time and the resources needed for manual analysis while ensuring a higher degree of consistency and objectivity. However, some of the limitations encountered so far are related to the sensitivity of the results to the sample preparation and image acquisition parameters.

Correlative microscopy techniques have proven to be effective for these tasks [10]. They combine data from different sources to assign the ground truth (expected output) in an objective way and generate masks to train the machine learning algorithms. However, this approach requires costly equipment and a high level of expertise. Therefore, the objective of this work is to upscale the classification and segmentation of light optical micrographs from two-phase steels by incorporating data from industrial grade samples. By using the segmentation results from previously trained models as masks, time and resources can be saved at the moment of training new models. Moreover, light optical micrographs are inexpensive to produce and already implemented for quality control at large-scale thus providing a practical solution.

The methodology of the work consists of the preparation of metallographic samples, acquisition of images, and analysis of the performance of the models to identify their strengths and weaknesses and produce more data to iteratively improve the performance. As a secondary objective, the correlation between the quantitative microstructure analysis based on the segmentation results and mechanical properties will be studied.

Chapter 2

Theoretical background

2.1 Steel

Steels are among the most utilized materials because of its wide range of properties and availability. It is an iron-based alloy, whose main alloying element is carbon. The versatility of steel is closely related to iron's crystalline structure.

Pure Iron exists in different crystalline structures or allotropes. Body centered cubic (BCC) also known as ferrite (α); Face centered cubic (FCC) known as austenite (γ) and hexagonal closed packed (ϵ). High temperature ferrite, known as delta ferrite (δ) exists at high temperature and is considered as a fourth allotrope, although its crystalline structure is not different from (α)-ferrite [11]. However, only austenite and ferrite are of technological relevance, as the hexagonal allotrope exclusively exists at very high pressure. Both (γ) and (α) have tetrahedral and octahedral interstices. In steel, some of these places are occupied by carbon, which acts as an interstitial solute.

The wide variety of steel grades available is the result of decades of research and development. There are dozens of alloying elements that combined with carefully designed thermomechanical treatments make it possible to achieve application tailored properties. The chemical composition and the manufacturing process determine the microstructure, which is linked to the behaviour of the material. Second phases and lattice strain, for example, act as barriers for dislocation movement and thus result in increased strength [12]. Therefore, it is important to be able to characterize the microstructure precisely and objectively. To do so, the different phase transformations and typical microstructures found on steel must be understood.

2.1.1 Phases and phase transformations

During cooling, the primary solid phase to form in steel is austenite. Although (δ)-ferrite may also be formed, it is less relevant in the steel production processes. In autenite's FCC structure, carbon occupies the octahedral holes. It is important to note that although the austenite has a more compact packing than ferrite, it also has larger interstices, which results in a higher carbon solubility. Starting from the austenitic field, different solid state phase transformations might take place, depending on the chemical composition of the steel and cooling conditions. These can be classified according to the atomic movement mechanism. In reconstructive transformations, the atomic bonds are broken, and the atoms then rearrange in a different pattern through diffusion. However, diffusion is a thermally activated process and its rate shows an exponential dependence with temperature. As a consequence, reconstructive phase transformations are only possible at high temperatures, where thermal energy provides enough atomic mobility to rearrange

the atoms. Displacive phase transformations are instead difussionless and occur as a consequence of coordinated atom motion without breaking the bonds [11]. The difference between these two mechanisms is schematized in figure 2.1. Different transformation mechanisms lead to different phases and microstructures, which consequently define the properties of the material.
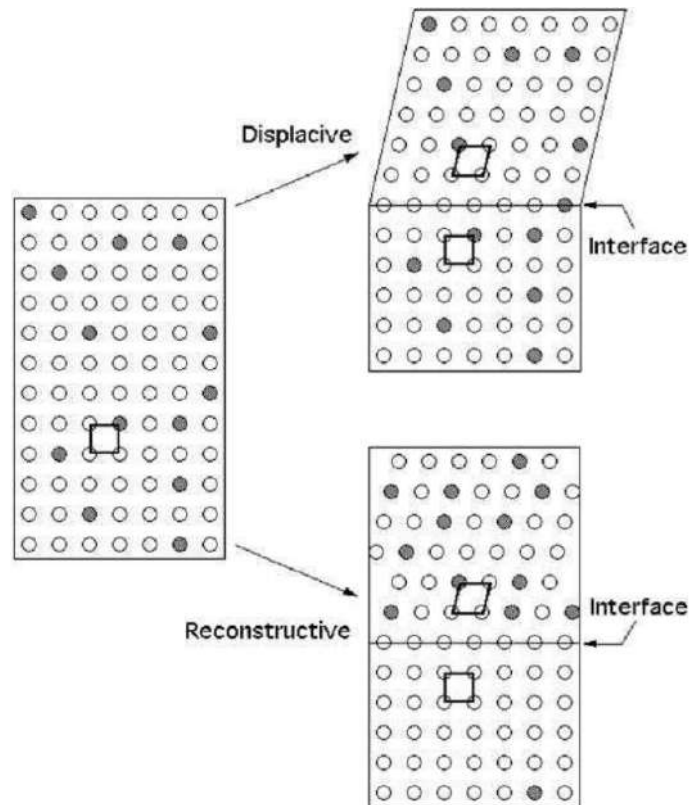

Figure 2.1: Reconstructive and displacive phase transformation mechanisms [11].

The phases that are formed by slow cooling of steel can be seen in the Iron-Carbon diagram shown in the figure 2.2. This is a metastable equilibrium diagram between pure iron and the iron carbide known as cementite (Fe_3C) instead of the thermodynamic equilibrium with graphite. True equilibrium is not typically reached in steels because the time needed for diffusion and precipitation of graphite is too long. Cementite has an orthorhombic crystalline structure and a composition of 6.67 wt% carbon. It is very hard but also brittle.

The iron-carbon system has an eutectoid point (S) at 0.76 wt% and 727 °C (also known as Ae_1 temperature). In an eutectoid transformation, one solid decomposes into two different phases. In steels, the eutectoid microstructure is known as pearlite, a lamellar mixture of ferrite and cementite. This is a reconstructive reaction that initiates mostly at austenite grain boundaries but can also start at other energetic sites such as inclusions. Nucleation of ferrite leads to carbon enrichment of the surroundings, which induces nucleation of cementite. As the process repeats, the lamellar structure is formed [13]. It is important to note that at lower temperatures or faster cooling rates, the interlamellar spacing is reduced because of the limited diffusion. This generates a harder pearlitic phase. Another characteristic temperature in the phase diagram is Ae_3 which indicates the transformation from austenite to ferrite. Ae_3 for pure iron is 912 °C (G) and decreases as the carbon content increases.
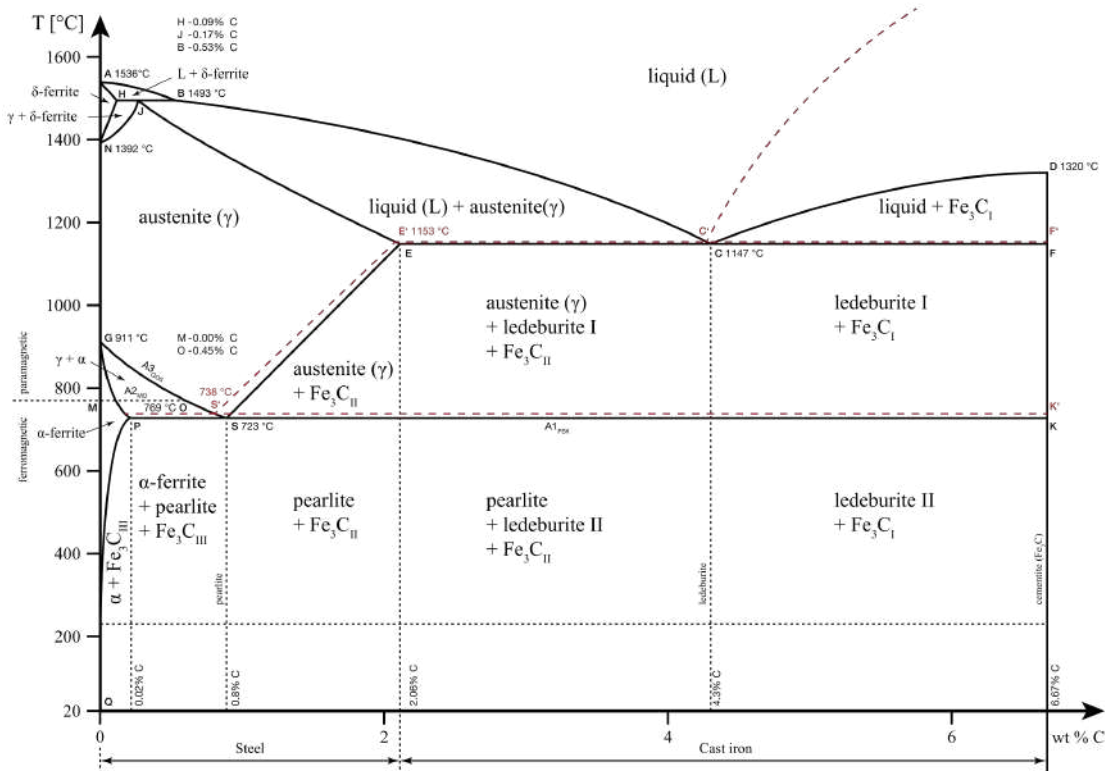
Figure 2.2: Iron - carbon equilibrium phase diagram. Solid black lines represent the metastable equilibrium with cementite and red dotted lines the thermodynamic equilibrium with graphite [14].

Regarding their carbon content, steels can be classified as hypoeutectoid, eutectoid or hypereutectoid. After slow cooling, hypoeutectoid steels (less than 0,76 wt% C) exhibit a combination of ferrite and pearlite, eutectoid steels are fully pearlitic and hypereutectoid steels constituents are pearlite and cementite. When hypoeutectoid steels are slowly cooled from the austenitic field, proeutectoid ferrite nucleates at austenite grain boundaries and grows into them [11]. Carbon is then rejected to the remaining austenite until it reaches the eutectoid composition. Subsequently, the remnant austenite transforms into pearlite, resulting in a ferritic-pearlitic microstructure. As the carbon solubility of ferrite at ambient temperature is very low, ferrite is almost pure iron and thus soft and ductile.

The materials utilized in this work can be classified as low carbon steel, which is a sub type of hypoeutectoid steel characterized by a carbon content lower than 0.25 wt% [11]. Within this group, a wide range of properties can be achieved, ranging from cost effective plain-carbon steels to high performance high strength low alloy steels [11].

There are other phases that can exist in steel because of non-equilibrium conditions. A time-temperature-transformation (TTT) diagram (see figure 2.3) can be used to predict non equilibrium constituents. These plots show the isothermal phase transformations of a given material as a function of temperature and time. In the case of steels, bainite and martensite are the two most important non equilibrium microstructures.
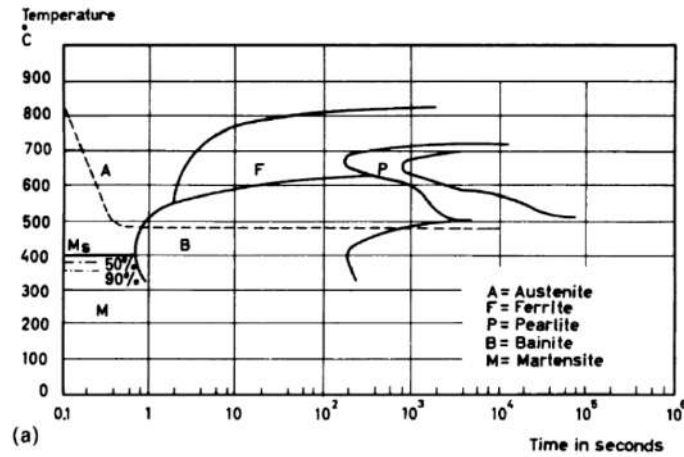
Figure 2.3: Steel TTT diagram [13].

Bainite forms at temperatures in which diffusion of iron and substitutional alloying elements is very limited, yet carbon diffusion still takes place. Its growth initiates as carbon supersaturated ferrite forms at austenite grain boundaries through a displacive mechanism. Due to its complex nature, the classification of bainitic microstructures is still a topic of debate. The most classical approach distinguishes two bainite types depending on the formation mechanism, as it is shown in the figure 2.4. In upper bainite (UB), the carbon partitions into the surrounding austenite and then precipitates as cementite between the bainitic ferrite plates. In the lower bainite (LB), instead, the ferrite supersaturates in carbon, followed by cementite precipitation within and between the sub-units [15]. Because of this, UB is stronger than LB [13]. However, there are more complex classification systems that also consider the nature of the second phase as well as the precipitates distribution in the microstructure, resulting in up to 5 bainitic subclasses: granular bainite, upper bainite, degenerate upper bainite, lower bainite and degenerate lower bainite [16].
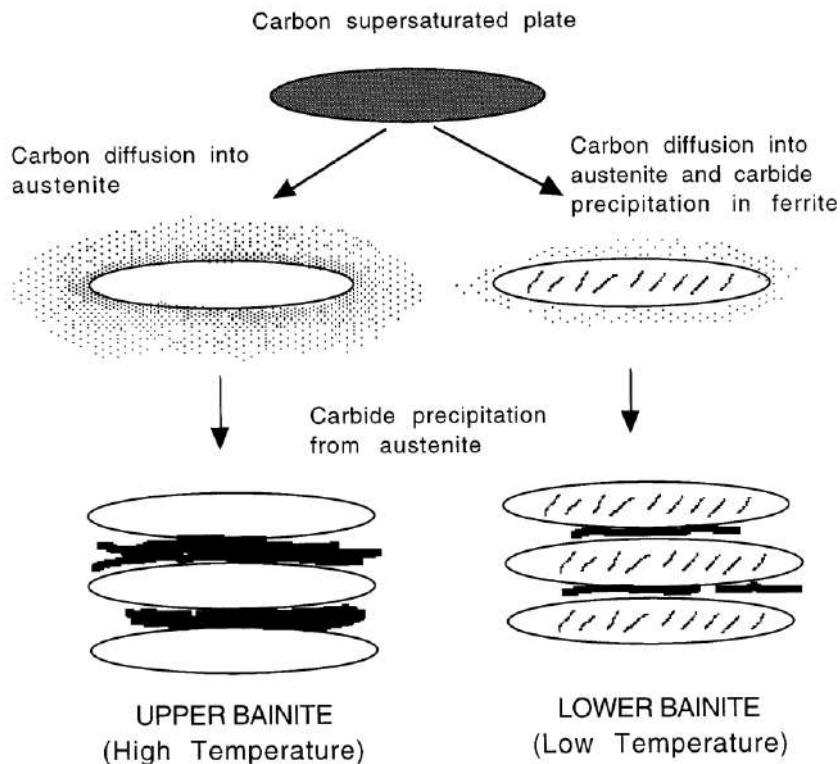

Figure 2.4: Upper and lower bainite growth mechanism [17].

14

Martensitic microstructure is the result of the martensitic displacive transformation that takes place in steel at lower temperatures, in which diffusion of either interstitial or substitutional solutes is not possible. Martensite is a supersaturated solution of carbon in ferrite [13] that has a body centered tetragonal (BCT) structure. Two types of martensite can be distinguished, depending on the carbon content of the austenite from which it is formed. Lath martensite in low carbon steels and plate martensite in high carbon steels, as it is shown in the figure 2.5. It is important to note that the martensitic transformation is very fast and diffusionless. In technological processes, the percentage of austenite that converts into martensite does not depend on the time, but only on the temperature. There is a well-defined temperature at which the transformation starts (M_s) which decreases as the carbon content of the austenite increases [11]. Under certain conditions, if the carbon content is high enough so that the temperature for complete transformation (M_f) lies below ambient temperature, retained austenite might be present in the microstructure. In this context, retained austenite refers to a metastable austenitic phase, that can exist at room temperature due to kinetics restrictions and strain constrains as a consequence of the martensitic transformation [18]. The martensitic transformation generates elastic strain in the atomic lattice, which restricts the dislocation movement and contributes to martensite's high hardness. However, as it is too brittle for most technological applications, a heat treatment known as tempering can be applied to increase toughness through carbide precipitation and elastic strain relief [13].
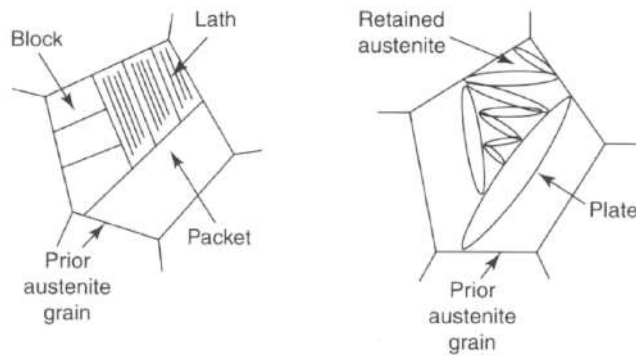

Figure 2.5: Low carbon Lath martensite (left) and high carbon Plate martensite (right) microstructures [12].

2.1.2 Thermomechanical treatments

Thermomechanical treatments are used in steel to alter their mechanical properties. This is achieved by applying heat and mechanical deformation to the material in a controlled manner. As a consequence, microstructural parameters such as the grain size, phases present and precipitate distribution can be modified.

For example, after cold working the defect concentration on the material increases, as the grains become more elongated due to the plastic deformation. This results in work hardening and reduced ductility [11]. If the material is then heated, a recrystallization process takes place. The defects introduced during cold working increase the internal energy (U) of the material and act as the driving force for nucleation and growth of new grains. This process can be used to achieve grain refinement and partially regain the original ductility [19].

An example of the application of these principles is thermomechanical rolling. Rolled steels are extensively used and the object of study of this work. During the rolling process, steel slabs produced by continuous casting are reduced in thickness by passing them through pairs of rolls

with a gap smaller than the original thickness. The process starts by heating the slabs to the austenitic range. This allows the homogenization of the chemical composition and the dissolution of alloying elements while increasing the workability of the steel. Recrystallization might also take place and results in a grain size refinement which leads to better mechanical properties [20].

As shown in the figure 2.6, there are different rolling procedures characterized by their rolling temperatures and thermal cycles, that lead to different microstructures and properties.
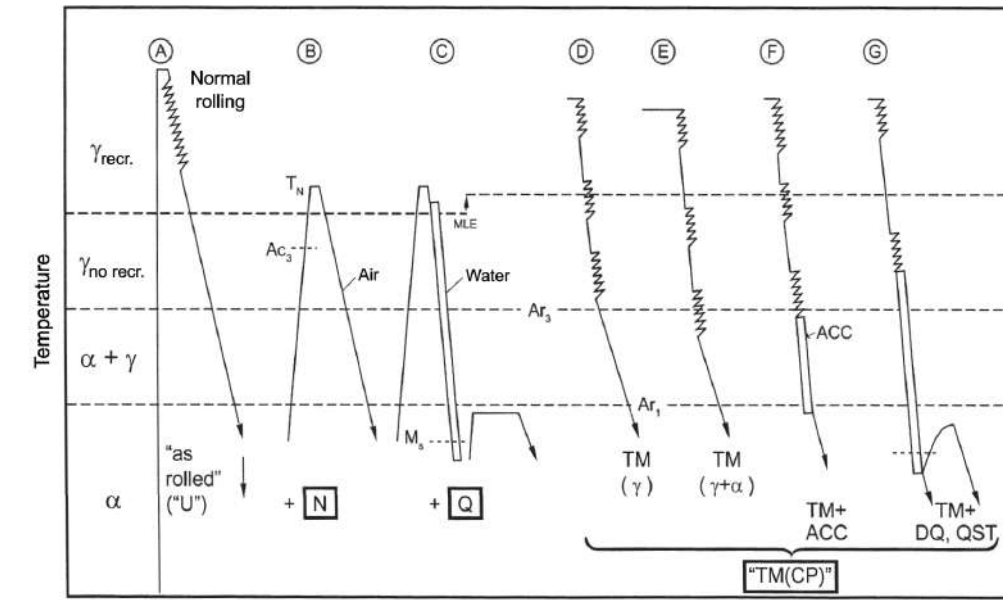

Figure 2.6: Rolling procedures [20]. N = normalized, Q = quenched, TM = thermomechanical, ACC = Accelerated cooling, DQ = direct quenched, QST = Q + self tempered.

Traditional rolling, shown in 2.6 A, takes place at a temperature in the recrystallization range $\gamma_{recr.}$ and is followed by cooling in air. This procedure only aims to achieve the desired geometry of the plate, without a controlled change in microstructure. The plate can then be reheated and normalized (N) (2.6 B). This treatment leads to a ferritic-pearlitic microstructure because of the slow cooling in air.

Another option is to quench (Q) the steel. This refers to the process of heating it to the austenitic range and then cooling it rapidly in water, reaching M_s temperature before the austenite transforms into ferrite and resulting in a martensitic microstructure. The quenching is often followed by an annealing stage that results in carbide precipitation and increased toughness.

The procedures known as thermomechanical rolling (TM) are shown in 2.6 D, E, F and G. Here, the rolling temperature is carefully chosen to achieve a specific combination of properties by the end of the process. By rolling below the recrystallization temperature, the deformation is accumulated in the material, resulting in work hardening.

In treatments F and G, an additional step known as Accelerated Cooling (ACC) is applied. This process involves cooling down the plates using a system of high-pressure water jets. The modification of the water flow results in different cooling rates and temperature gradients across the plate's thickness, leading to differences in the microstructure.

An important consideration regarding rolled plates is their microstructural gradient. When the plates are cooled down, temperature decreases faster near the surface, generally leading to a finer microstructure with low temperature transformation products and higher strength in this region [21]. However, another characteristic of rolled plates is the presence of centerline segregation as a consequence of the solidification process during the continuous casting. Segregation occurs

because most of the alloying elements have a lower solubility in the solid than in the liquid phase. Therefore, as solidification takes place from the surface of the slab towards the core, the alloying elements are rejected to the remaining liquid, increasing its solute concentration in the center [22]. While this phenomenon can be controlled by optimizing the parameters of the continuous casting process and the thermal treatments during rolling, it is often not completely avoided. The center line segregation usually leads to a higher strength and hardness on the center of the plate, accompanied by a lower fracture toughness [23].

One example of the application of thermomechanical rolling is the production of dual phase steels. The microstructure of these steels consists of a mixture of a softer (usually ferrite) and a harder (usually martensite) phase. This can be achieved by inter-critical annealing between Ae_1 and Ae_3. During this process, a portion of the austenite is allowed to transform into ferrite and the remaining austenite is then converted into martensite. The main advantage of these steels is their combination of high formability with elevated strength [11].

To ensure the quality of the products and achieve consistent results the process parameters must be closely monitored and samples from the finished plates must be regularly analyzed in a metallography laboratory.

2.2   Metallography

Quantitative microstructural evaluation plays a pivotal role in quality control. With the advance of microstructural complexity and more strict specification requirements, the microstructure of materials must be closely analyzed to ensure the desired performance. The different phases and microstructures present on steel can be analyzed using different metallography techniques.

To do so, samples are mirror polished, etched using an acidic solution and observed under a microscope. Etching can be understood as a process of controlled corrosion used to contrast the different microstructural constituents [24]. Every constituent in the sample is attacked at a different rate, therefore creating a raised relief on the surface. There are different etching solutions that can be used to highlight different aspects of the microstructure. Nital is one of the most popular etchants for steels, as it can be used to reveal the different phases and grain boundaries [24]. It is usually a solution of 1 to 5% nitric acid in ethanol. It is important to be aware that the etching results are influenced by the quality of the polishing, the concentration of the solution, the time of exposure, the environmental conditions, and the microstructure itself. This makes it difficult to achieve consistent results for different samples. Once the sample is etched, it is observed on the light optical microscope (LOM).

Metallographic light optical microscopes generate an image from the sample by reflecting light on its surface (see figure 2.7 (a)). During structural etching, the solution removes material from the different regions at different rates, thus revealing the microstructure, as it is shown in figure 2.7 (b). For example, as discussed before, grain boundaries will be preferentially attacked by nital etching. As a result, when observed in the microscope, they appear darker because a higher fraction of the incident light is scattered. However, grains of uniform composition such as ferrite or cementite have a smooth surface after etching, reflect a big fraction of the incident light and appear bright under the microscope [19]. Therefore, to be able to differentiate them, morphological features such as the size or aspect ratio must be considered.
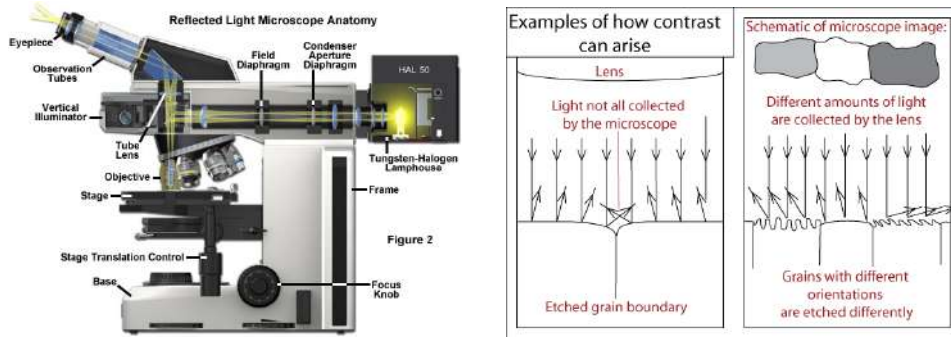
(a) Reflexion light optical microscope schema [25]

(b) Etching generated contrast in LOM [26]

Figure 2.7: Light optical microscope light path and contrasting mechanism.

Microscopes are complex devices that offer a wide range of configurations that affect the way the microstructure is shown. The optical system of a LOM is composed of the objectives and the eye piece. Different objectives are used for different magnifications and have different working distance, numerical aperture, resolving power and depth of field [24].

Resolving power represents the minimum distance at which two points can be perceived as separated. According to abbe's theory (eq. 2.1), it is limited by the wavelength of the visible light used (λ) and by the numerical aperture of the lens (NA), which depends on the refractive index of the medium (n) and the collection angle of the lens (Θ) [27]. Taking this into account, resolving power (d) in optical microscopy cannot be higher than 0.2 μm.

$$d = \frac{\lambda}{2n \cdot sin(\theta)} = \frac{\lambda}{2 \cdot NA} \tag{2.1}$$

This can be a problem when trying to differentiate microstructures such as pearlite if the interlamellar spacing is too small or bainite as the individual plates within the sheaves are also irresolvable. In these cases, the nodular appearance of the pearlite compared to the sheaf structure of the bainite can help to distinguish them [15].

Another crucial aspect of light optical microscopy is the illumination system, whose main components are the light source, aperture diaphragm, and field diaphragm. The intensity of the light as well as the opening of both diaphragms must be set by the metallographer and can severely affect the quality of the results. The aperture diaphragm affects the resolution and contrast in the micrograph, and its optimal value is related to the numerical aperture of the objective. If the aperture is too small, there is a loss in resolution and if it is too large there is a loss in contrast. The field diaphragm instead controls the field of view and must be carefully set to minimize glare.

The topography of the sample also must be considered as it affects the diffraction and scattering of the incident light. Etching intensity plays an important role in it, as more etched samples exhibit a bigger height difference between the constituents. However, if the topography features are too small, like the carbide distribution in lower bainite, for example, it is not possible to resolve them with the LOM. While LB usually has a darker etching response because of this [15], consistent classification is not always possible.

Lastly, there are also several software-controlled parameters that add one more layer of complexity, as it is necessary to transform the photons reflected from the sample into a digital representation. White balance allows the calibration of the different color channels intensity to reduce color bias [28], gain amplifies the signal from the camera sensor, exposure time controls the amount of light that the sensor receives from the sample and gamma correction adapts the camera output

to the way the human eye perceives light [29]. All these parameters also influence the appearance of the microstructure in the images that are later used for analysis.

All the above-mentioned variables contribute to a very high variance in micrographs, which makes even more complex the task of consistent and reliable microstructural characterization. The expertise and criteria of the metallographer also comes into play and the subjectivity of the results is even bigger for complex structures, such as different classes of bainite to which there is no clear consensus for labeling and classifying [7].

A way to complement optical microscopy is the utilization of electron microscopy. The scanning electron microscope (SEM) uses a beam of electrons that generates several signals that can be used to characterize the sample, as it is shown in the figure 2.8. The main advantage of the SEM over the LOM is the increase in resolution. As the wavelength of the electrons is much shorter than that of the visible light, the resolution power increases, making it possible to distinguish small features that are irresolvable in the optical microscope. The combination of different sources of data to characterize a sample is known as correlative microscopy and constitutes a powerful tool to assign the ground truth (expected output) for machine learning models [30].

Secondary electrons detectors are particularly useful in this context, as they reveal the surface topography from the sample. There are two main variants: the conventional Everhart-Thornley detector and the In-Lens detector. While both target the electrons generated from the primary electron beam interaction with the sample and reveal surface topography, the In-Lens detector provides a better signal to noise ratio and higher spatial resolution [31].
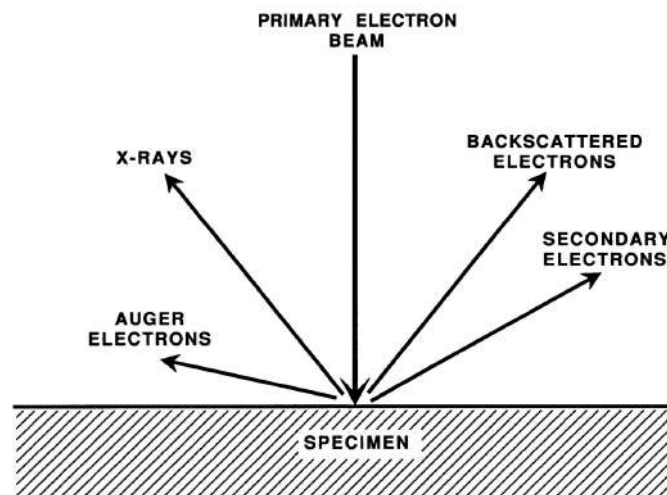

Figure 2.8: Signals generated by the scanning electron microscope [24].

Quantitative evaluation of microstructures from micrographs has the intrinsic complexity of viewing only a 2D section of a 3D microstructure. In consequence, factors such as anisotropy from the rolling need to be considered at the moment of the analysis. The appearance of the same microstructural component may be completely different depending on the plane from which it is viewed.

Several techniques have been developed to achieve a consistent quantitative microstructural analysis, however, the subjectivity of the metallographer cannot be eliminated. As it has been shown in other studies [32], the variation in expert judgment of microstructures can be significant.

On top of the challenges associated with constituent identification, the determination of second phase fraction is a very time-consuming process. Before computational analysis was feasible, this was done by hand according to the ASTM E562 standard by means of point counting [33]. This method consists of superimposing a grid of points over the micrograph and counting the amount

of them that are over the constituent of interest. Variables such as the magnification, the number of fields (micrographs) and points on the grid determine the compromise between the effort needed and the precision of the results.

The same approach is used by image analyzers [34]. These softwares can save time and resources, but if the contrast between the phases is not enough or if the second phase is not correctly identified, the results are not representative of the sample.

To use an image analyzer, the image needs to be segmented, that means that the pixels need to be assigned to a class. The simplest way to achieve this is through a threshold (see figure 2.9). A threshold is an intensity value that serves as a criterion for distinguishing the classes on the image. There are several methods to define this value. It can be manually selected or using an algorithm that considers the histogram distribution of the pixel intensity values for its computation. In more complex approaches, the neighbors' pixels might also be considered, or different thresholds applied to different regions of the same image [35]. The result of the threshold segmentation is a binary image where all the pixels with a gray value lower than the threshold are set to black and all the pixels with a higher value are set to white.

However, thresholding techniques fail to deliver good results when the gray values of the classes overlap, the intra class variance is too high, or if there are shadings in the picture. This motivates the utilization of artificial intelligence techniques, that can consider several features of the picture to give an objective and reproducible quantification of the microstructural features of a sample.

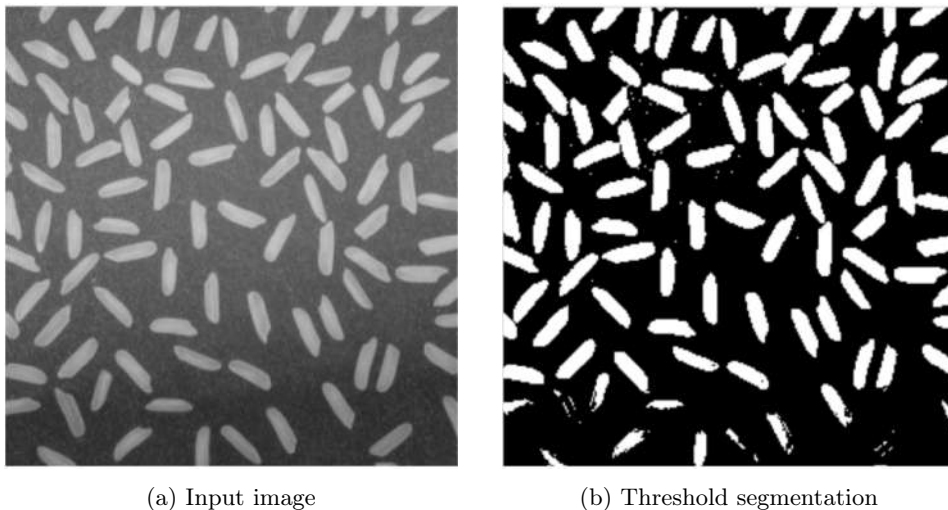(a) Input image   (b) Threshold segmentation

Figure 2.9: Threshold segmentation results on rice grains [36]. Undetected grains at the bottom are a consequence of the threshold techniques limitations.

2.3   Machine learning

Machine learning is a sub-field of artificial intelligence, framed in the field of computer science, which includes a set of techniques that involve the use of data and empirical information to build models without these being explicitly programmed [37]. However, traditional coding remains essential for tasks such as defining the model's architecture and processing data. The absence of explicit programming refers to the way machine learning algorithms mimic human decision-making by learning features from data through statistical modelling to predict future values, rather than following explicit commands for specific tasks [9]. In recent years, these techniques have experienced an exponential increase in popularity, which has led to their implementation in different fields, including materials science.

Machine Learning algorithms can be classified according to the information used to create the model. The models are trained with a data set, which consists of data points known as instances. Each instance has associated features or properties. The target is the feature to be predicted [38]. In supervised learning techniques, learning is done from annotated data. This means that the algorithm is provided with the expected output for each instance, which is known as the ground truth. In unsupervised learning, on the other hand, the algorithm is responsible for identifying the patterns in the data to produce an output [9]. In general, supervised learning is used when the outcomes are known, and the model learns the relationship between the input variables and the expected output. Unsupervised learning, on the other hand, is useful to discover the structure of the data and its underlying connections [9].

Another way to classify machine learning algorithms is based on the type of task they perform. In regression problems, the model predicts the value for a continuous variable. The simplest example of this is linear regression, that assumes a linear relationship between the input and the target variable. However, regression models can also be used to identify more complex relationships between the features. The goal in every case is to find the best trend line to fit the data [9].

Classification algorithms on the other hand predict a category or class for each instance of the data, from a finite number of classes [39]. The task concerning this work is semantic image segmentation. Segmentation techniques are used to divide images into meaningful regions, setting the boundaries between them and the background [40]. Segmentation models perform a pixel-wise classification. In other words, every pixel is assigned to a class. In semantic segmentation, no distinction is made between objects belonging to the same class, but this problem is addressed by instance segmentation models. A summary of the object recognition techniques can be seen in the figure 2.10.
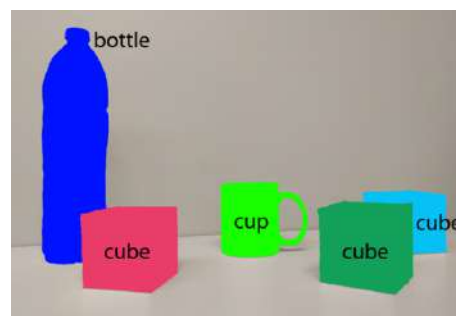

(a) Image classification
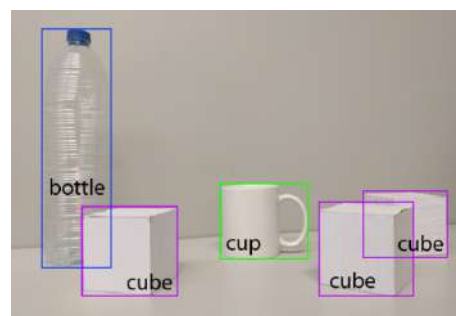
(b) Object localization
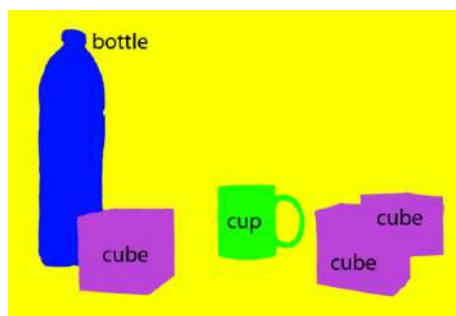
(c) Semantic segmentation

(d) Instance segmentation

Figure 2.10: Image recognition techniques [41].

2.3.1 Artificial neural networks (ANN)

Artificial neural networks are machine learning algorithms that mimic the functioning of biological neurons. The neurons are arranged in layers, where the first one holds the input data; the last one the output, and the layers in between are known as hidden layers. There are different types of artificial neural networks. The simplest ones are fully connected feed forward neural networks. In these, all neurons from one layer are connected to every neuron of the next one, as shown in figure 2.11.
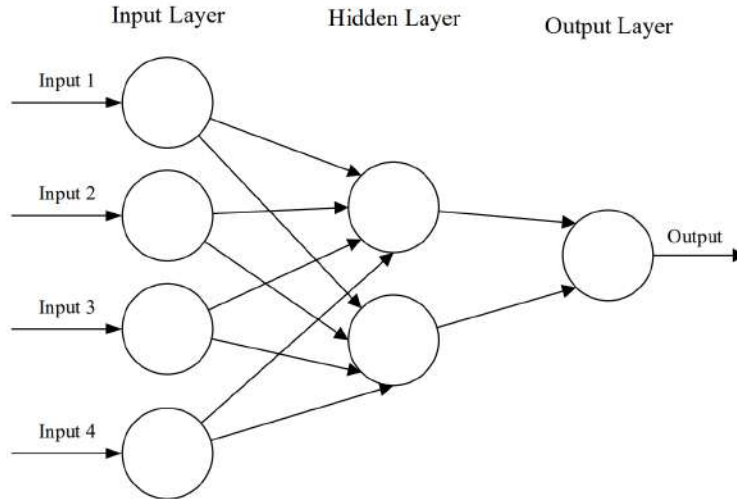
Figure 2.11: Feed forward neural network schema [42]

The information transmission from one layer to the next one takes place in two steps. First, the input 'X' is affected by a weight and a bias, to give the output of the neuron z_i (eq. 2.2). The output is then transformed by an activation function $f(z_i)$ (eq 2.3), and the activation value 'a' is transferred to the next layer neuron z_{i+1} (eq. 2.4). The weights (W_i) and biases (b_i) are the trainable parameters that are iteratively optimized during the training of the network in order to achieve the best possible fit to the expected output.

$$z_2 = W_1 \cdot X + b_1 \tag{2.2}$$

$$a_2 = f(z_2) \tag{2.3}$$

$$z_3 = W_2 \cdot a_2 + b_2 \tag{2.4}$$

When an input image is run through the network the output is compared to the ground truth (expected output) and a cost function is computed. There are different cost functions, but all accomplish the same task: determining how far away is the model's prediction from the expected output. The gradient of the cost function with respect to the parameters is then used to update the weights and biases of the network. This is done using a backpropagation algorithm that computes the derivatives of the cost function with respect to the trainable parameters through partial derivatives from the last layer to the first one according to the chain rule. The bigger the gradient, the bigger the modification to the parameter, as shown in the equations 2.5 and 2.6. Where C is the cost function, ϵ the learning rate and the superscript indicates the iteration number. The bigger the learning rate the bigger the changes to the parameters on every iteration.

A bigger learning rate may lead to a faster convergence of the model. However, if it is too big, the minimum of the cost function may never be reached. This problem is known as overshooting.

$$W^{j+1} = W^j - \epsilon \cdot \frac{\partial C}{\partial W_j} \tag{2.5}$$

$$b^{j+1} = b^j - \epsilon \cdot \frac{\partial C}{\partial b_j} \tag{2.6}$$

The same principle applies to convolutional neural networks, which are used for image processing and computer vision tasks. In contrast with fully connected neural networks that take vectors as inputs, convolutional neural networks are designed to work with matrices. As the natural representation of an image is a matrix with its pixels values, the use of convolutional neural networks makes it possible to maintain the spatial correlation of the features from the images across the layers.

A convolution is a mathematical operation that consists of element-wise matrix multiplication. The convolutional filter is a much smaller matrix that multiplies the image matrix, giving a feature map as a product. By doing this, the spatial relationship between the pixels in the image can be detected and used to extract relevant features for the segmentation [9]. The convolutional filters are iteratively optimized during the network training to extract relevant features that improve the performance on the given task.

Deep learning architectures

Deep learning techniques use several layers of neurons, with multiple filters on each one. The feature maps created are fed into the next layer and the last one performs the segmentation [9]. The two relevant deep learning architectures for this project are DenseNet-201 and U-NET.

DenseNet-201 [43] is a convolutional neural network architecture, schematized in figure 2.12, that introduces dense blocks in which all the layers are interconnected with each other, rather than just the adjacent ones. This way, all the feature maps from previous layers are fed as input to the next one. This approach proved to reduce the number of trainable parameters needed in the network by reducing the number of filters in each layer. Moreover, as the earlier feature maps are concatenated to the later layers, feature propagation is improved. The network includes a total of 201 layers and achieved an outstanding performance on the Image-Net classification data set [44].
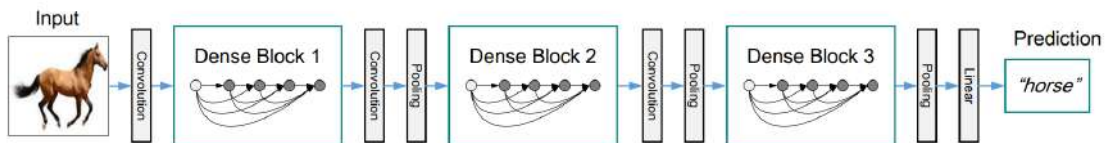

Figure 2.12: DenseNet architecture [43].

U-NET is a popular architecture for image segmentation schematized in the figure 2.13. It has 23 convolutional layers. As there is no fully connected layer, it can be classified as a fully convolutional neural network [45]. Its name comes from the shape of the architecture that resembles an U, where the left side is the contracting path or encoder and the right side the expansive path or decoder.
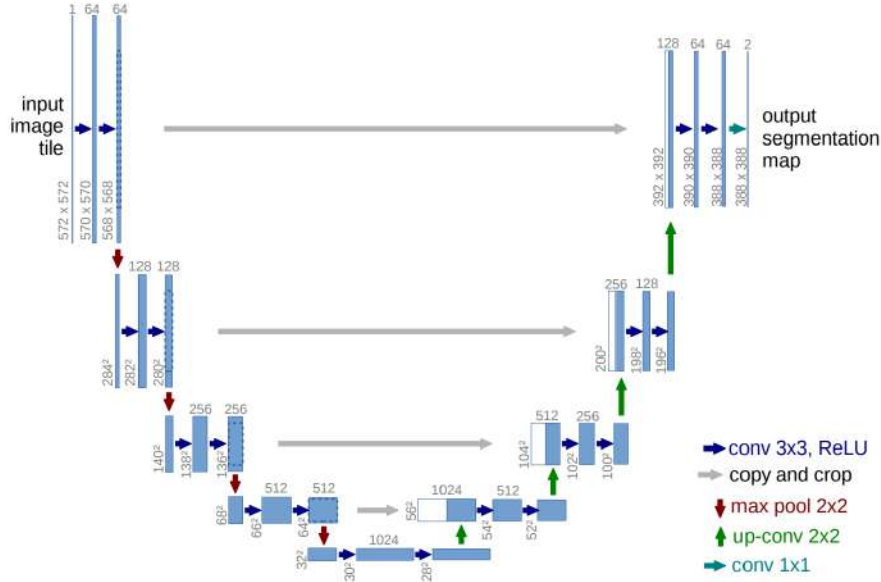
Figure 2.13: U-NET architecture [45].

Each arrow represents a step in the architecture. The different types of operations shown are:

- Convolution 3x3, ReLU: it is a convolutional operation, where 3x3 refers to the size of the convolutional filter matrix. Rectified linear unit (ReLU) is the activation function of the neurons. The activation function defines the final activation for the node. In this case, the ReLu can be expressed as:

$$ReLu(x) = max(0, x) \tag{2.7}$$

This means that if the convolution results in a number lower than 0, then the neuron output is equal to 0 and if the result is positive, then the neuron activation is equal to the convolution result.

- Copy and crop: These steps are known as skip connections and copy the early activation maps into deeper blocks. This is the most distinctive characteristic of the network and results in a more efficient segmentation due to the utilization of different levels of abstraction in the same layer. [40]

- Max pool 2x2: The max pooling operation consists in the compression of a region of the Input matrix (2x2 in size in this case) by taking its maximum value [40]. This process is known as down-sampling because the size of the feature maps is reduced. As a result, the kernel of the next layer covers a bigger section of the original image, allowing it to detect features on a bigger scale [40].

- Up-convolution 2x2: it is an up-sampling convolution operation, which results in an increase in the size of the feature maps. The number of upsampling convolutions needs to match the convolutions in the encoder or contracting path so that the final size of the feature maps matches the input size of the image and gives a pixel wise classification as output.

- Convolution 1x1: It is the last step of the architecture which condenses the feature maps into the probability of each pixel to belong to an specific class. This is done through the SoftMax activation function, shown in eq. 2.8.

24

$$Softmax(z_i) = \frac{\exp(z_i)}{\sum_{j=1}^{K} \exp(z_j)} \qquad (2.8)$$

Where z_i is the output from the neural network corresponding to the ith class, and $\sum_{j=1}^{K} \exp(z_j)$ is the sum of the exponentiated outputs over all classes K. The exponentiation ensures that each output is positive, and the summation normalizes the result, giving the probabilities.

2.3.2   Network training

One challenge when working with deep learning models is the availability of training data. This can be because of limited access to source images or because the annotation process is too time consuming.

Annotation is the way to produce the masks needed for model training. These masks are the ground truth or expected output for the model prediction. In segmentation tasks, the masks consist of pixel-wise classified images, a process that can be highly time consuming when done manually. Moreover, due to the complex nature of the microstructures and the high number of second phase objects, achieving a 100 % accuracy is not feasible. Moreover, identifying the nature of the second phase is already a challenging task. That is the reason why correlative microscopy approaches are often used to address this issue [30].

Depending on the architecture of the network and the nature of the task, several thousand images might be needed to train a model. There are two useful tools to mitigate this problem: Transfer learning and data augmentation.

Transfer learning means taking the weights of a pre-trained network to start the training of the new one. This has been proven to reduce the number of pictures required to converge and to reduce the computational cost of the training. Furthermore, it is desirable but not necessary that the tasks of both networks are similar. For example, Napel et al successfully used the trained weights from ImageNet to classify malignant and benignant tumours [46]. Even using weights from classification networks has been proven useful for segmentation models [41].

To take advantage of the Image-Net trained weights of DenseNet-201 while maintaining the architecture of U-NET, transfer learning using the segmentation models library [47] can be utilized. It allows the importation of the DenseNet-201 encoder as backbone with the trained weights. By setting these weights as non-trainable, the amount of computational power needed to train the network is reduced, as only the weights of the decoder or expansive path need to be updated.

Data augmentation on the other hand is the process of applying transformations to the images in the data set to increase the amount of data that is available to train the model. There are different types of transformations that include translation, shearing, distortion, crop, etc. These can be implemented using the 'Albumentations' open source library available for Python [48]. The intensity and amount of augmented data influences the performance of the model. In most cases, leading to faster convergence and better generalization capabilities. Furthermore, it can help to balance the classes representation in the dataset to avoid favoring the most frequent class [49].

Once the dataset, network architecture, backbone for transfer learning and data augmentation parameters are established, the data set is divided into training, validation, and testing sets and the training of the network takes place.

The training dataset consists of input images and their corresponding masks, which are used during training to update the model parameters, aiming to minimize the difference between the predictions and the ground truth. Similarly, the validation dataset also consists of input images and their masks, which are used during training as a measure of the model's performance on unseen

data, as it is not used to update the model's parameters [38].

This data splitting aims to detect and reduce overfitting problems, where the model learns the features of each instance from the training data set but has no generalization capabilities. Therefore, while achieving optimal metrics in the training dataset may be a good indicator, poor performance on the validation data set can be a sign of overfitting [38].

During training, the training dataset is further divided into batches, which are run through the network. At the end of every batch, the cost function is calculated, and the weights updated. Every time the whole data set runs through the model, one epoch is completed. The batch size, number of epochs and learning rate are hyperparameters that are set before starting the training of the network. They are experimentally tuned to achieve the best results, but they are also constrained by the computational power available.

As the loss function itself is not easily interpreted, training metrics are calculated to estimate the performance of the model. One of the most popular metrics is intersection over union (IoU), also known as Jaccard Index. If A is the segmentation mask and B the ground truth, then IoU is defined as the quotient between the overlay area and the union area of both [50], as shown in equation 2.9. It can take values between 0 and 1, where 0 is completely wrong prediction and 1 perfect prediction.

$$IoU = J(A, B) = \frac{|A \cap B|}{|A \cup B|} \tag{2.9}$$

Lastly, the testing dataset consists of images that were not used during training and are employed to evaluate the final model performance. At this instance, masks can still be utilized but are no longer necessary. While quantification of deep learning predictions uncertainty is still a challenging problem [51], a practical approach to evaluate the model robustness is to analyze the performance on non-optimal images [6]. If the model shows a satisfactory and consistent performance despite the introduced variance, it is an indicator of robustness. Manageable variance is critical in machine learning models, especially for complex task such as segmentation of similar microstructures. The variance the model can handle is mostly determined by its representation in the training data, which should be aligned with the variance expected during model implementation [52].

2.3.3 Machine learning in materials science

Machine learning techniques have numerous applications in materials science, covering a wide range of topics.

For example, deep learning methods have been employed to correlate atomic structures with properties such as interatomic potentials [53] and formation energies [54]. Schmidt et al. published a detailed review of property predictions using machine learning techniques, ranging from band gap to melting temperature [55].

Other machine learning applications include structural information prediction from x-ray diffraction patterns [56], automatic segmentation of dislocation in nickel superalloys [57], multicomponent alloy design optimization [58] and warpage prediction of 3D printed parts [59].

Moving into steel microstructure characterization, machine learning has also been extensively used to process microscopy images.

Tsutsui et al. developed a classification model based on textural parameters to classify low carbon steel microstructures including martensite, upper and lower bainite. They used two different SEM microscopes and found that the models trained on one didn't have a good performance on the other, as the relevant features on the images changed [4].

Gola et al. combined SEM and LOM (correlative microscopy) images to extract textural, morphological, and substructural parameters of second phase objects for classification [10]. On the same line of work, Jaime et al. developed classification algorithms based on textural and morphological parameters from SEM and LOM images capable of successfully classifying pearlitic, bainitic and martensitic constituents through support vector machines [60]. One step further, Vega developed a series of machine learning algorithms for classification of bainitic and martensitic objects using random forest, support vector machine and convolutional neural networks, using correlative microscopy as data source [61].

Müller et al. achieved high accuracy for classification of different bainitic microstructures using textural parameters from SEM images with a support vector machine [7]. One step further, Müller et al also developed a classification model based on a support vector machine for classification of seven microstructural classes: pearlite, martensite and 5 bainitic subclasses. To do so, SEM images, textural features and morphological parameters were used, achieving an 82.9% correct classification [5].

Bachmann et al. used several machine learning techniques both for classification and segmentation of steel microstructures and was able to successfully use the results for correlation with processing parameters and mechanical properties. Correlative microscopy and different contrasting techniques were employed to characterize the samples [62]. Bachmann et al. also developed a deep learning model for segmentation of prior austenite grains from nital etched light optical micrographs [6].

Müller et al. provided a comprehensive overview of the state of the art in machine learning image processing for steel microstructures [52].

The different approaches differ both on the type of algorithms utilized and the information employed as input. For support vector machines and random forest models, the features must be previously selected (feature engineering), and they can either be morphological, textural or a combination of both. Whereas for deep learning algorithms, the feature extraction is done inside the neural network, without any external influence.

The main advantage of the conventional machine learning algorithms is that the relevant features can be traced back to the images and thus correlated with the results. However, deep learning approaches make it possible to incorporate patterns in the data that might be unseen to the person training the model.

Chapter 3

# Experimental procedure

3.1 Workflow and overview

The experimental work of this project was carried out in the research and development division of the AG der Dillinger Hüttenwerke, a steel mill located in Germany, using materials and equipment provided by them. The main product of this company are heavy plates, which are employed in different industries including piping, ships, heavy machinery, etc [63]. The facilities of the company include blast furnaces, continuous casting and rolling mills, which allows an integral control of the product. A quality control department performs metallographic analysis to probes cut-out from the plates, using mainly light optical microscopes and nital etched samples.

The main objective of the project is to upscale a computational tool to perform a quantitative microstructural analysis of dual phase steels. This model should be capable of performing consistently on an industrial scale to be implemented in quality control processes.

The models perform multi-class semantic segmentation. Taking LOM as input and producing a mask that contains the assigned class for every pixel (matrix, pearlite, and bainite/martensite) as output. From this data, the nature of the second phase, its percentage and morphological parameters of the particles can be estimated.

In order to upscale the existing models, an iterative approach was employed. This resulted in three generations of models, that were tested using images from industrial grade steel samples. Finally, the results from the last model were used to perform a quantitative microstructural analysis and to establish hardness correlations with the model output. These concepts will be further explained in the following sections.

To analyze the results from the models, different visualizations were produced, shown in figure 3.1. Figure 3.1 (a) shows the light optical micrography as it is used for input. The output from the network, visualized in figure 3.1 (b), is a probability map. As suggested by its name, probability maps contain the probability of each pixel belonging to every class. As there are three segmented classes, the probabilities are shown on a single color channel: green for matrix, blue for pearlite and red for bainite and martensite. These probability maps are then used to generate the final output from the model, the segmentation masks (3.1 (c)). They contain only three pixel values: Yellow for the matrix, blue for pearlite and red for bainite and martensite. In order to better evaluate the model's performance, the input image and the segmentation mask are overlayed, as shown in figure 3.1 (d). Finally, the last representation, shown in figure 3.1 (e), only displays the individual objects in different colors. These are used to calculate the morphological parameters of the particles which are calculated for both second phase classes. Therefore, only bainitic/martensitic or pearlitic objects are displayed.
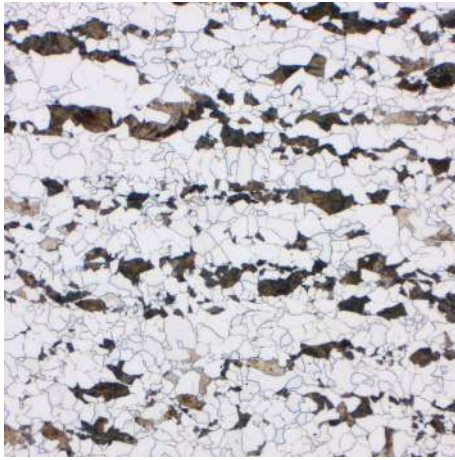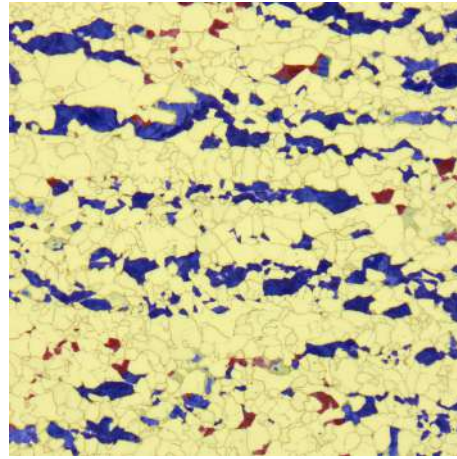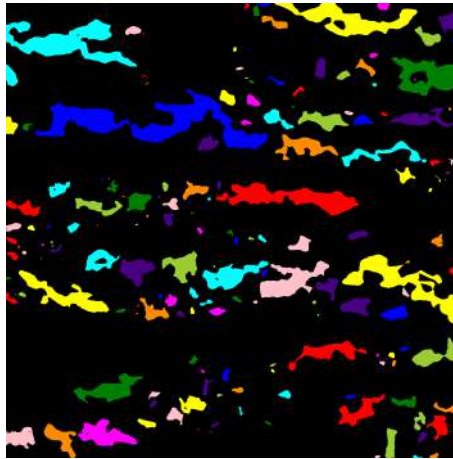
(a) Input image
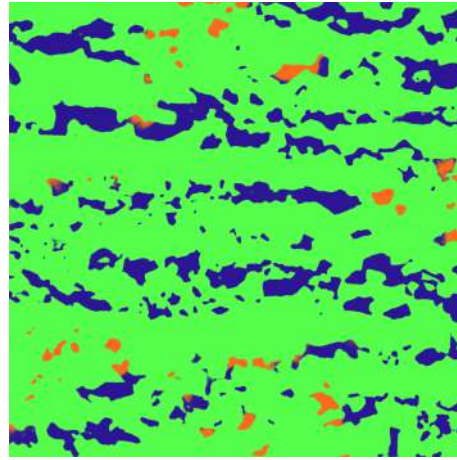
(b) Probability map
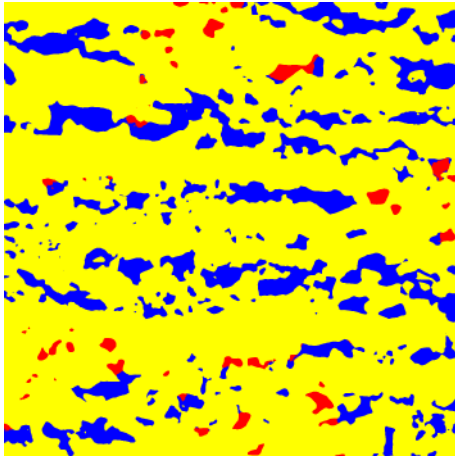
(c) Segmentation mask

(d) Overlay

(e) Detected pearlitic objects

Figure 3.1: Different visualizations employed.

3.2   Metallographic sample preparation

Metallographic specimens were prepared from different grades of rolled steels produced at the Dillinger Hütte steel mill . The samples selected contain a two-phase microstructure, which is the target of the models. Different thermomechanical treatments and chemical compositions among the selected samples make it possible to cover a wider range of appearance of the constituents, which is crucial to test the model's generalization capabilities. This means, the performance on unseen samples which are not exactly as the ones used for training. The samples used are detailed in table 3.1

Table 3.1: Samples analyzed.

Sample	Plate thickness (mm)	Carbon content (wt. %)	Second phase
1311	23.7	0.0525	Bainite / Martensite
1317	23.7	0.0525	Bainite / Martensite
1449	23.7	0.057	Bainite / Martensite
1453	23.7	0.057	Bainite / Martensite
B250	120	0.141	Pearlite
C925	100	0.174	Pearlite
E528	90	0.133	Pearlite
H687	20	0.05	Bainite / Martensite
M810	20.5	0.042	Bainite / Martensite

As explained before, it is expected to find a microstructural gradient across the sample thickness, originated due to segregation and differences in the cooling rate. In order to determine whether the model is capable of detecting these differences or not, the samples were cut perpendicular to the rolling direction, as shown in figure 3.2.
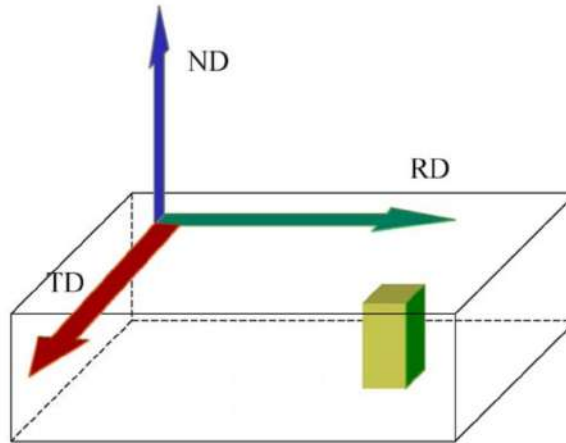
Figure 3.2: Sample extraction schema. The extracted probes include the whole plate thickness. RD=rolling direction, TD=transversal direction, ND=normal direction. Adapted from [64].

Multiple grinding and polishing steps are necessary to obtain an even surface, suitable for etching and microscopical evaluation of the samples. These steps are summarized in table 3.2. During the cutting process, damage is done to the specimen surface in the form of deep scratches and plastic deformation. Therefore, a sequence of abrasives is used to remove this damaged layer. With each step, progressively finer abrasives are used to eliminate the scratches from the previous stage, reducing the thickness of the deformed layer [24].

This process was carried out on a QATM Qpol 300 M2 manual grinding and polishing machine using a rotational speed of 150 RPM. The differences between grinding and polishing are shown in figure 3.3. Grinding is done with bonded abrasives. For this project, resin bonded diamond steel grinding discs were used. During grinding, the sample is held in a fixed position over the rotating disc. Once a uniform scratching pattern is achieved, the sample is rinsed in water and the next step is performed, rotating the sample 90° between steps. Grinding is followed by polishing. For polishing, a loose abrasive is used on top of a polishing cloth. In this case, diamond suspensions were employed. During this process, the sample is moved on an oval pattern over the rotating disc, counter to its rotation direction. Once all the scratches from the grinding are eliminated, the sample is rinsed using ethanol, dried with a hot air blower and a last polishing step is performed using a suspension with smaller particles, until mirror finish is achieved. The sample is one more time rinsed and dried and the results from the polishing are evaluated in an optical microscope, ensuring that no scratches are visible. The appearance of the surface after grinding and polishing is shown in figure 3.4.

Table 3.2: Metallographic sample preparation steps.

Process	Abrasive	Time (min)
Grinding	Struers MD Piano 220	2
	Struers MD Piano 500	2
	Struers MD Piano 1200	2
	Struers MD Piano 2000	2
	Struers MD Piano 4000	2
Polishing	3 µm Struers Diaduo 2	3
	1 µm Struers Diaduo 2	5
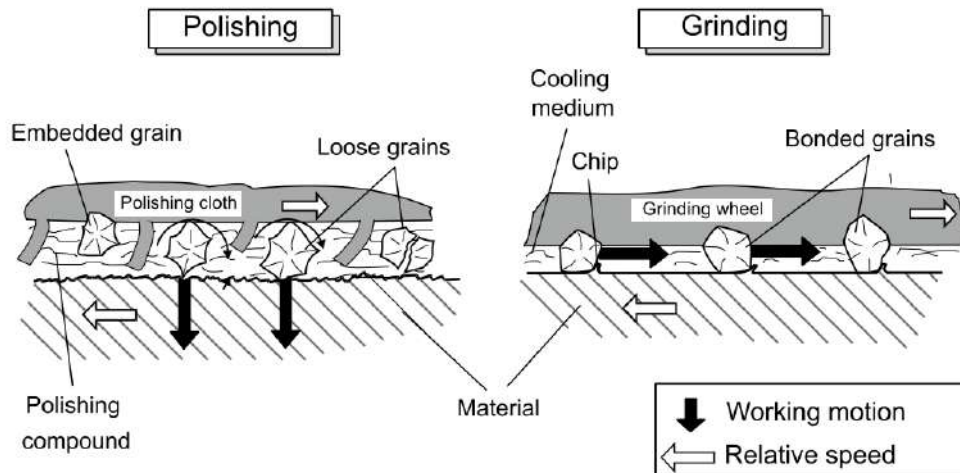
Figure 3.3: Working mechanisms in grinding and polishing. Adapted from [65].
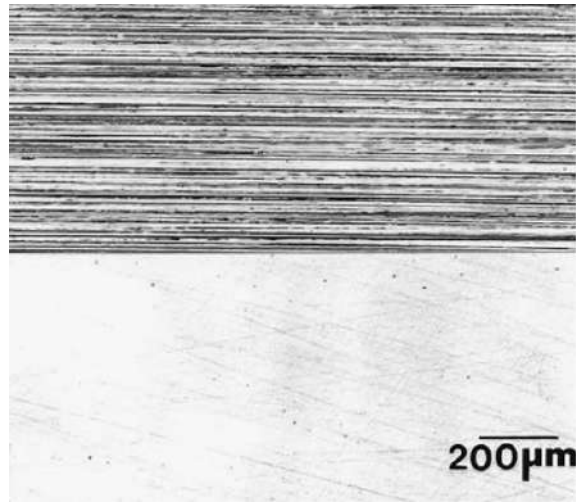
Figure 3.4: Micrographs of scratches from the metallographic preparation process. Top: grinding, bottom: polishing [24].

The polished samples were etched with a 2% nitric acid solution (nital) for 30s. In some samples, an irregular etching was observed, with higher intensity in the areas near the edges. This can be seen in figure 3.5 as a difference in reflectivity, where more opaque regions correspond to a higher etching intensity. The implications of this phenomenon will be discussed in the following chapter.

(a) Sample H687

(b) Sample M810
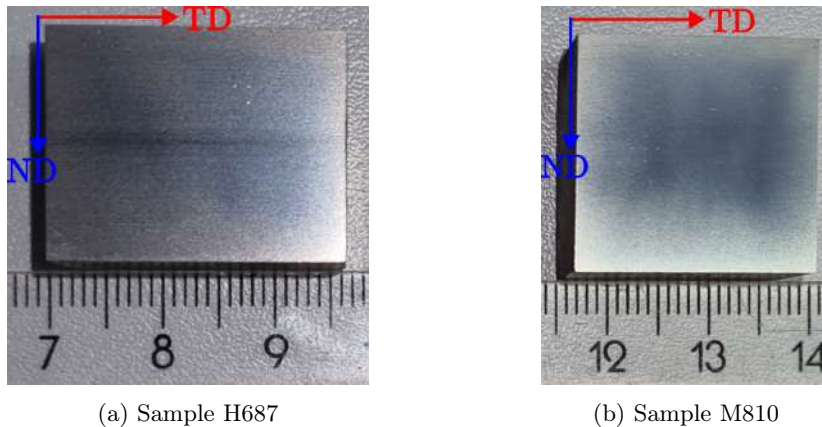
Figure 3.5: Irregular etching intensity. More etching is observed near the edges of the sample, especially close to the top and bottom surfaces of the plate (top and bottom of the images).

3.3   Image acquisition and processing

As explained before, due to the nature of the rolling process, it is expected to find a microstructural gradient across the plate thickness. To find out whether these differences could be detected and quantified by the model, the regions of interest (ROI) chosen were near the surface (S), at a quarter thickness (Q) and at half the plate thickness (H). For example, as it is shown in figure 3.6 for the sample C925, the second phase objects become bigger towards the center of the plate.

(a) Surface   (b) Quarter thickness   (c) Half thickness
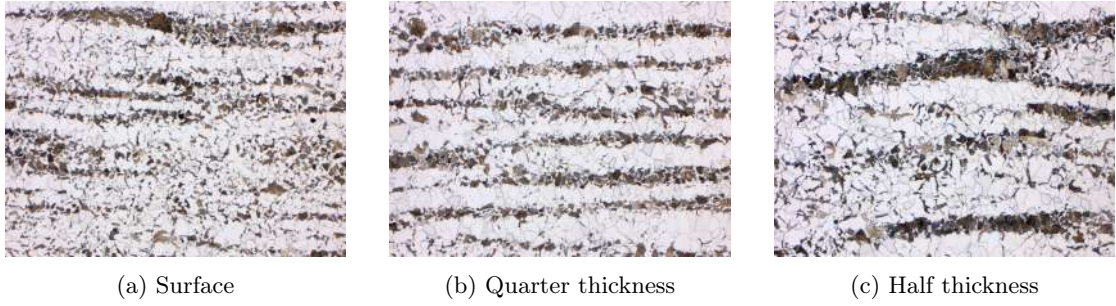
Figure 3.6: Microstructural gradient on different ROI. Sample C925, 200x magnification, Zeiss Axio Imager.M2m, optimal imaging settings.

The ROIs were marked in the samples using hardness indentations, as shown in figure 3.7. These easy to identify indentations were used to position the different microscopes at the same place, in order to compare the results from the different image sources.

(a) Schema   (b) Sample 1317
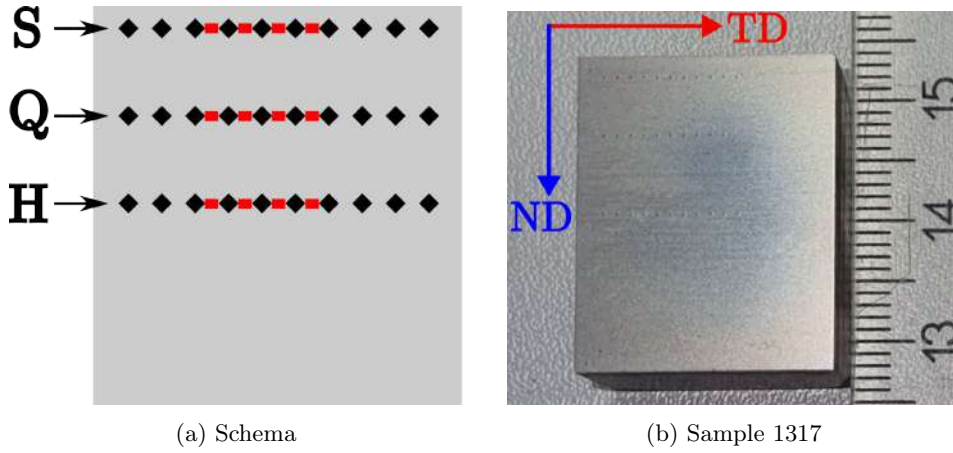
Figure 3.7: ROI determination. Indentations are shown as black rhombuses and the ROI as red rectangles (not to scale). S = surface, Q = quarter thickness, M = half thickness.

By including images from different microscopes into the training data, the variance from different cameras, optical and illumination systems was also introduced to the models. The 4 different microscopes used characteristics are shown in table 3.3, and image examples in figure 3.8.

Table 3.3: Utilized microscopes characteristics.

Microscope	Light source	Camera	Image resolution
Nikon Eclipse L200	100 W halogen lamp	Jenoptik ProgRes CT3	2048 x 1536 px
Reichert Jung Polyvar MET	100 W halogen lamp	Jenoptik ProgRes CT3	2048 x 1536 px
Zeiss Axio imager.M2m	100 W halogen lamp	Jenoptik Gryphax	2000 x 1500 px
Zeiss Axio imager.Z2m	100 W halogen lamp	Zeiss AxioCam HRc	1388 x 1040 px 4164 x 3120 px[1]

---

[1]Scanned color mode
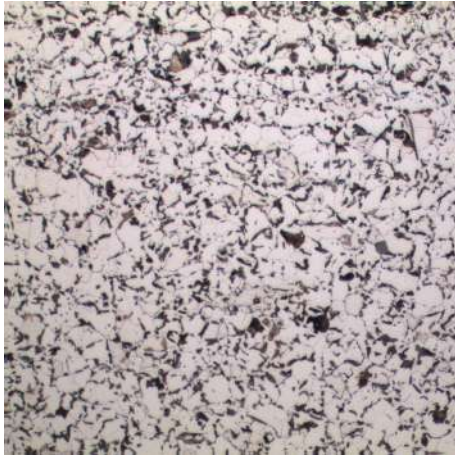
(a) Nikon Eclipse L200   (b) Reichert-Jung Polyvar MET
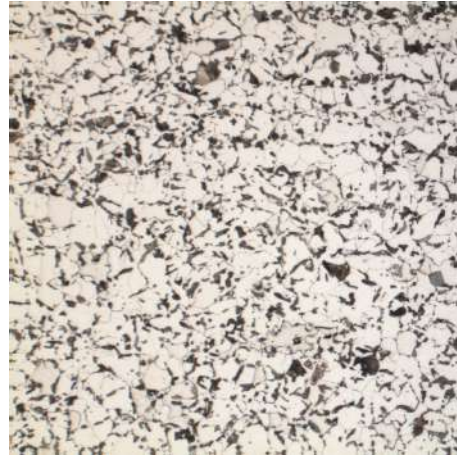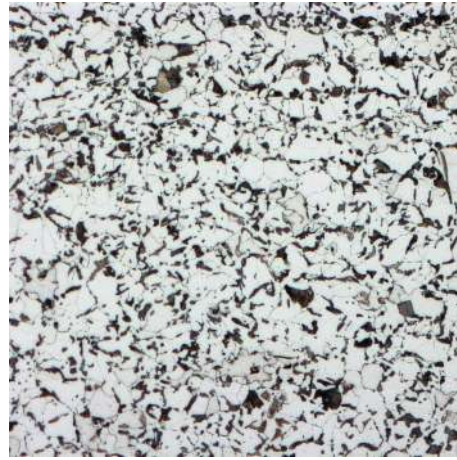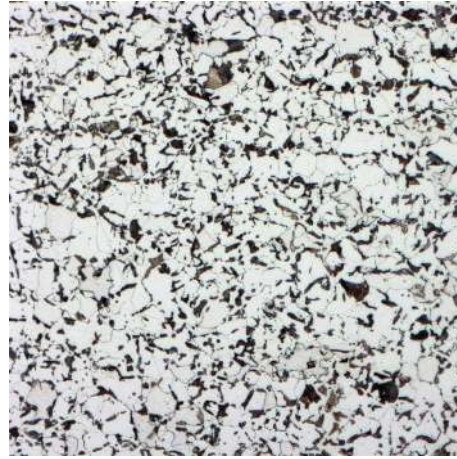
(c) Zeiss Axio Imager.M2m   (d) Zeiss Axio Imager.Z2m

Figure 3.8: Different microscopes image comparison. Sample E528, 200x magnification, optimal imaging settings.

One of the key aspects of the project is the robustness of the model. This means that the model should be able to handle not only perfect micrographs, but also those taken in suboptimal conditions. On an industrial scale, this variance is inevitable because of the high volume of samples produced and analyzed. To train and test this, images were taken using optimal settings as well as nonoptimal. The best conditions images were taken keeping the acquisition settings (exposure time, white balance, light intensity, aperture, gamma correction and gain) constant for each sample and microscope. Additionally, a variety of nonoptimal micrographs were taken under different conditions including variations in aperture, exposure time, focus mode, resolution, and etching intensity. Some examples are shown in figures 3.9 and 3.10. These additional pictures aim to increase the robustness of the models, improving their generalization capabilities.
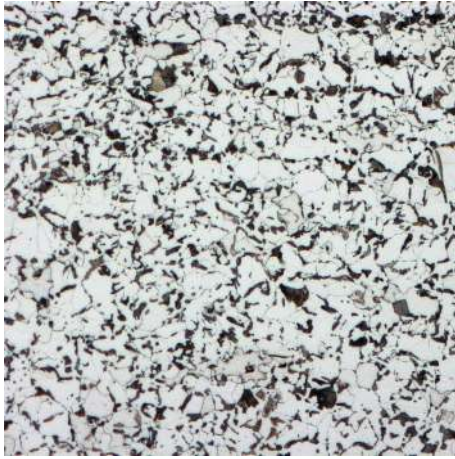
(a) Multi focus

(b) Single focus
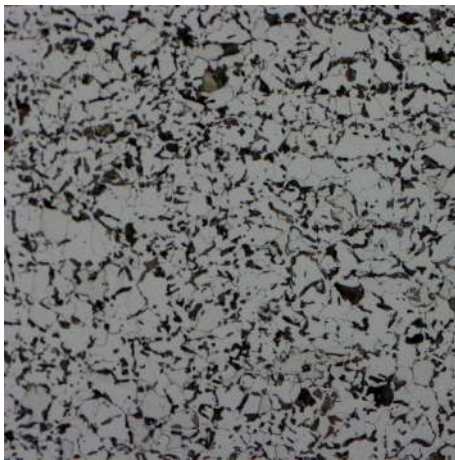
(c) Short exposure time
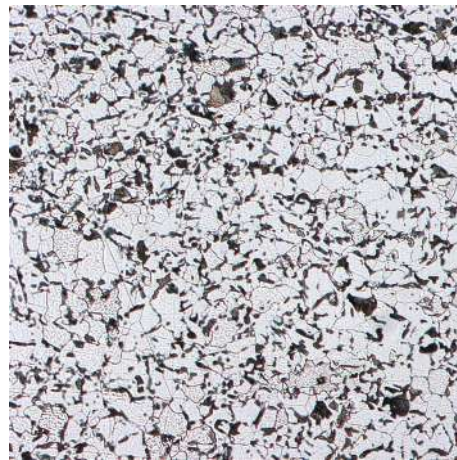
(d) Low aperture

Figure 3.9: Different acquisition conditions comparison. Sample E528, 200x magnification, Zeiss Axio Imager.Z2m.

(a) Surface

(b) Quarter thickness

(c) Half thickness

Figure 3.10: Different etching intensities comparison. Sample M810, 500x magnification, Zeiss Axio Imager.M2m.

Another desirable feature of the model is scale invariance. In other words, images at different magnifications of the same microstructure should be successfully segmented. To achieve this, images at 200x, 500x and 1000x magnifications were employed (see figure 3.11). Lower magnifications were not used as they did not reveal the microstructural features and further magnification was not considered as it would not capture more details due to the limit of resolution of the LOM.

(a) 200x   (b) 500x   (c) 1000x
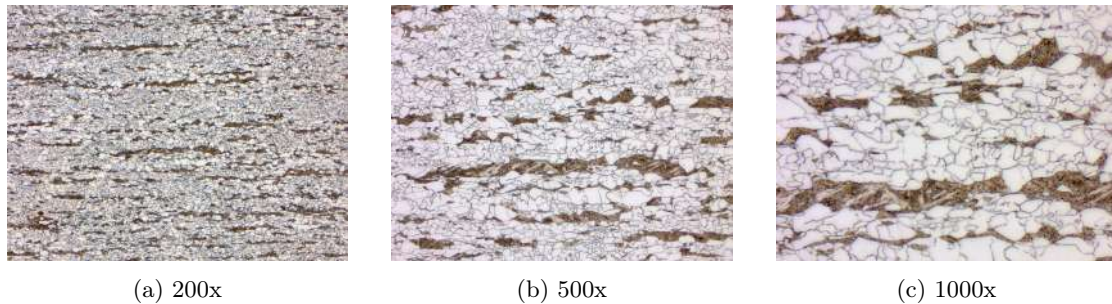
Figure 3.11: Different magnification comparison. Sample 1453, Zeiss Axio Imager.M2m., optimal imaging settings

Complimentary SEM micrographs were taken with a Zeiss Supra 55 microscope with the In-Lens secondary electrons detector. As shown in figure 3.12, the increased resolving power of the SEM allows a better identification of the substructures within the constituents, and this information is considered to assign the classes to the pixels in the images used for training (ground truth).

(a) LOM, 200x magnification. Sample E528

(b) SEM InLens, 2000x magnification. Sample E528

(c) LOM, 500x magnification. Sample M810

(d) SEM InLens, 5000x magnification. Sample M810
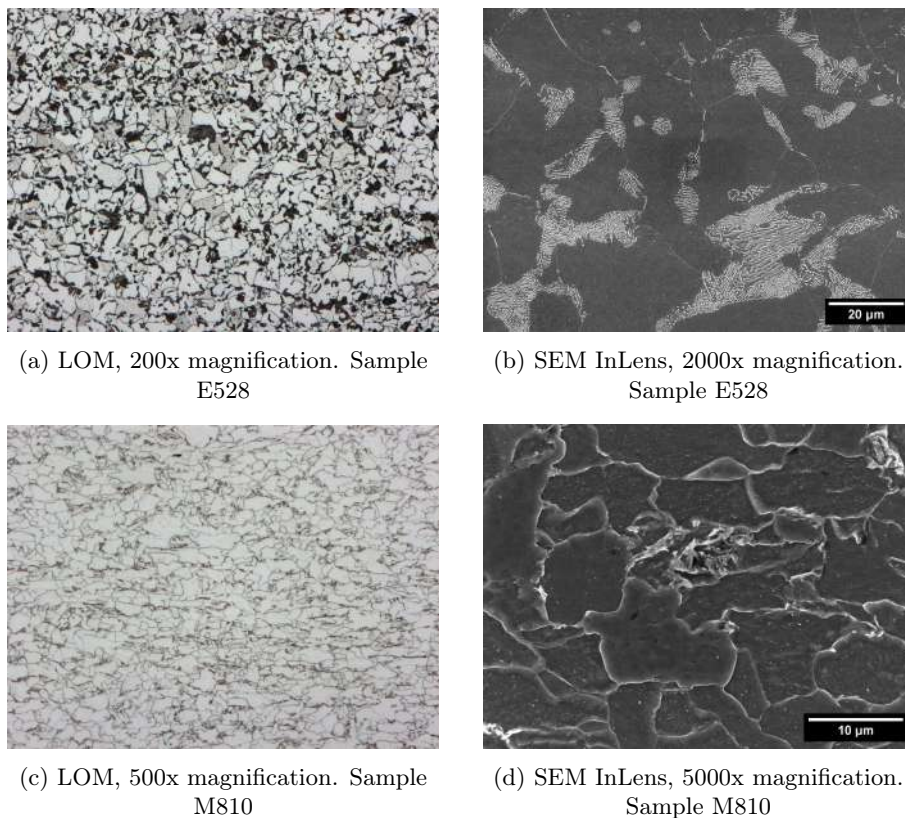
Figure 3.12: Different constituents in LOM and SEM. Sample E528 ((a) and (b)) shows a ferritic-pearlitic microstructure while the sample M810 ((c) and (d)) is bainitic.

The constituents were identified by comparing the appearance of the microstructure with the expected morphology found in literature as well as based on the guidance provided by specialists. The schematic representation of the microstructures shown in figure 3.12 found in bibliography are shown in figure 3.13

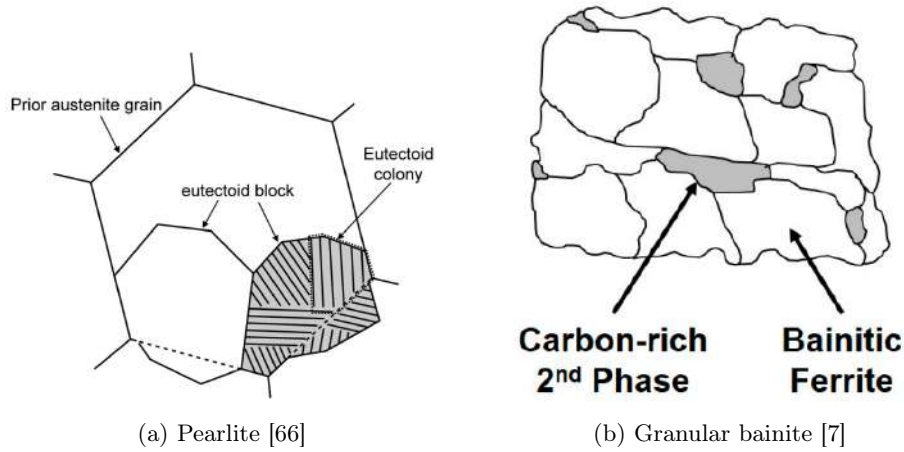(a) Pearlite [66]   (b) Granular bainite [7]

Figure 3.13: Schematic representation of steel microstructural constituents.

The images were cropped into squares for analysis. In the first generation models, a shading correction through the rolling ball background subtraction algorithm [67] was performed. The name of the algorithm comes from its working principle. As shown in figure 3.14, a sphere is used to estimate the background, defined by the minimum intensity encountered by the ball at every pixel. As shown in figure 3.15, this step aims to eliminate the shadings resulting from the illumination system, reducing the feature variance and consequently, the number of images required for training.
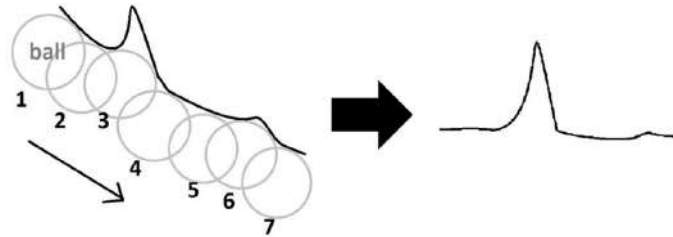
Figure 3.14: Rolling ball algorithm working principle (1D adaptation) [68].
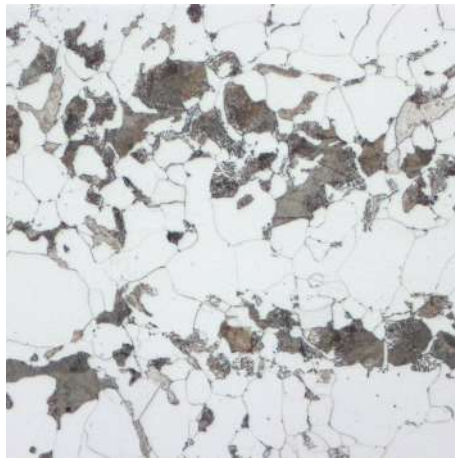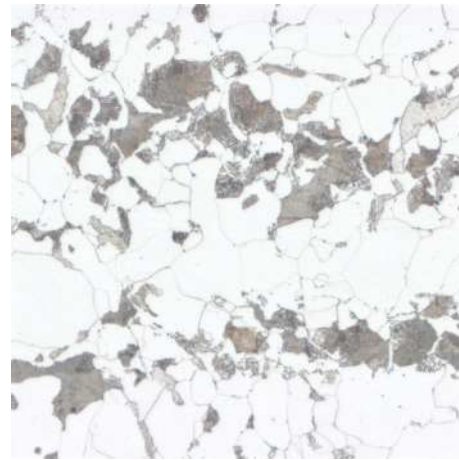
(a) Optimal imaging settings. Before shading correction
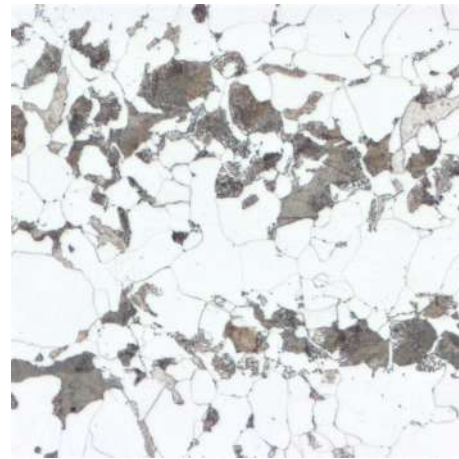
(b) Optimal imaging settings. After shading correction
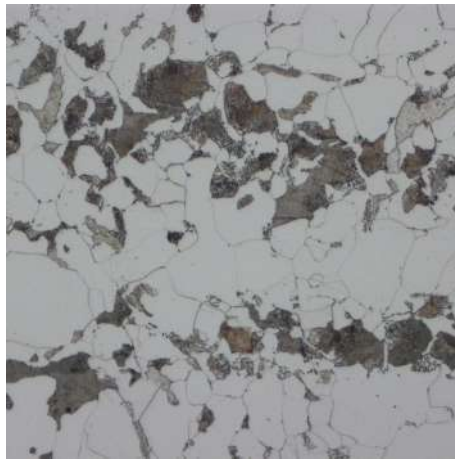
(c) Short exposure time. Before shading correction

(d) Short exposure time. After shading correction

Figure 3.15: Shading correction effect. The difference between the optimal and the dark images is smaller after shading correction. Sample C925, 500x magnification, Zeiss Axio Imager.Z2m.

In the second and third generation models, a threshold was applied to the matrix prediction. This threshold function (in contrast with threshold segmentation introduced before) works on the probability maps that the models produce as output. In this context, a threshold was applied to the matrix probability, so that if the probability of a given pixel of corresponding to the matrix class is higher than the threshold, it will be classified as matrix regardless of the existence of another class with higher probability. This process is shown in figure 3.16.
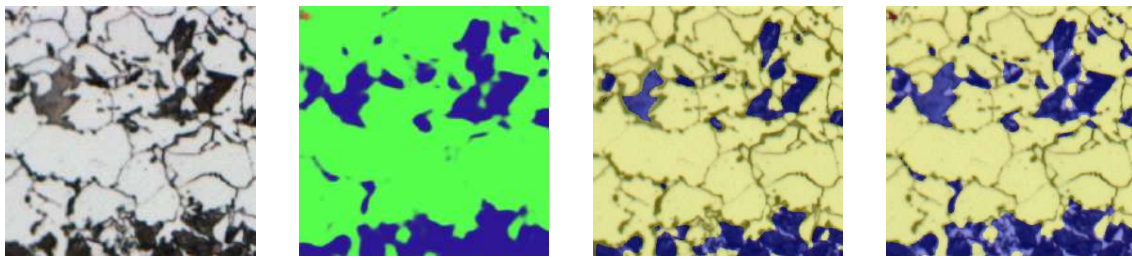
(a) Input image   (b) Probability map   (c) Threshold=0.08   (d) Threshold=0.8

Figure 3.16: Threshold function process. Sample E528, 200x magnification (zoomed).

Data augmentation was introduced to produce more data instances aiming to improve the robustness of the model and reduce the amount of annotation needed. An overview of some of the transformations is shown in figure 3.17.
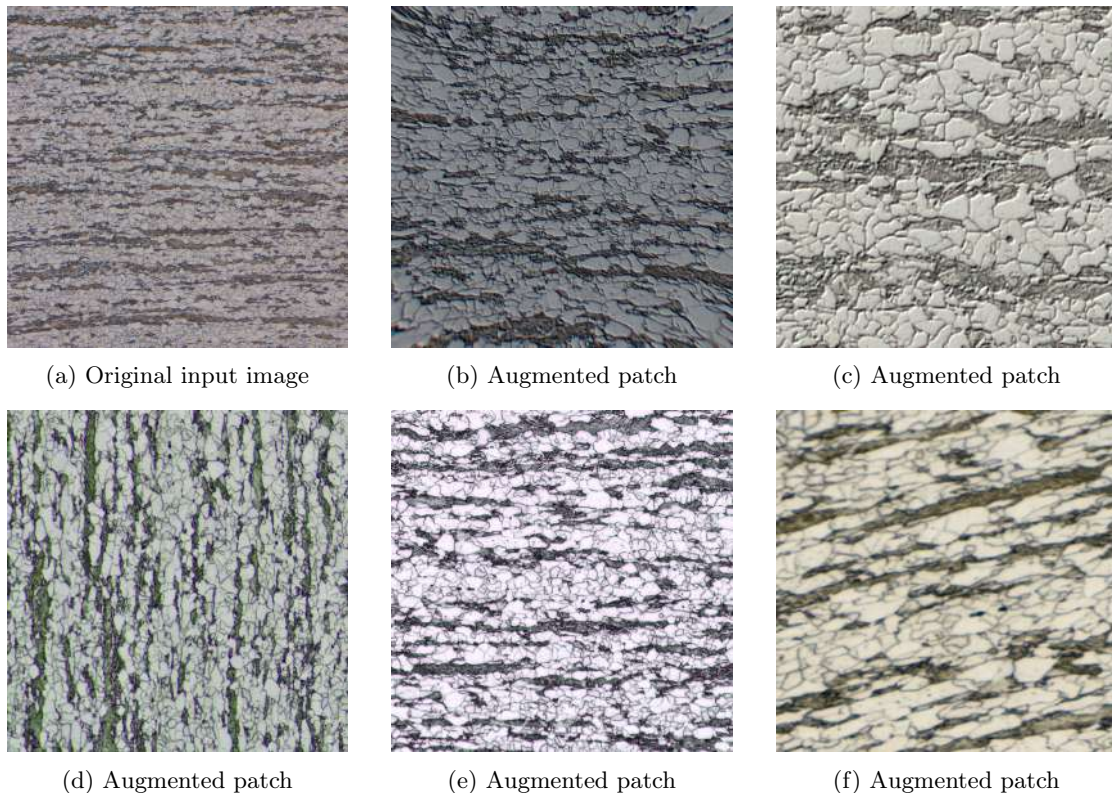
(a) Original input image   (b) Augmented patch   (c) Augmented patch

(d) Augmented patch   (e) Augmented patch   (f) Augmented patch

Figure 3.17: Training input image and augmented patches. Sample H687, 200x magnification, Zeiss Axio Imager.M2m

3.4   Iterative model optimization

An overview of the workflow of the project is shown in figure 3.18. As explained before, an iterative approach was employed. This resulted in three generations of models, that were tested using images from industrial grade steel samples. The best results from each generation were used as training data for the next generation. This minimized the necessity for hand annotation, a very time-consuming step in the model development. However, in some cases, manual corrections to the model generated masks were performed. Finally, the results from the last model were used to perform a quantitative microstructural analysis and to establish hardness correlations with the model output.
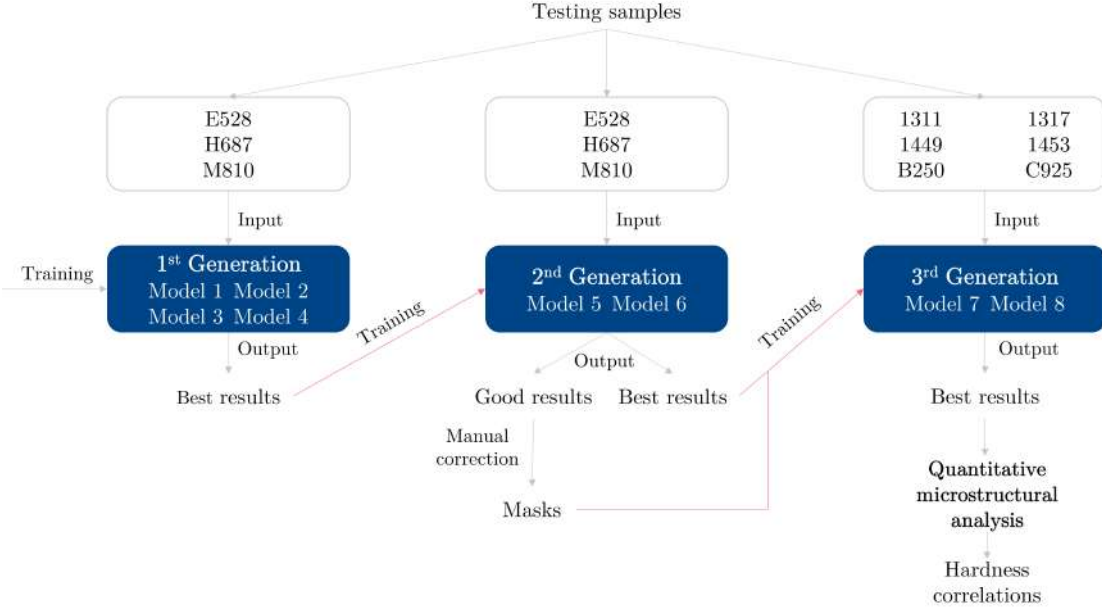
Figure 3.18: Workflow overview.

The deep learning segmentation models trained use the U-NET architecture with DenseNet-201 encoder as backbone. Due to the previously discussed limitations of the LOM, it is not possible to reliably distinguish bainite from martensite, therefore it was decided to concatenate these two constituents in one class. Moreover, one sample may have both bainitic and martensitic objects in different positions across the sample thickness, making it even more complex to classify them separately when assigning the ground truth for model training.

Four first-generation models were trained using images from the Dillinger Hütte database. Their characteristics are shown in the table 3.4. Testing of the performance of the models was done using pictures from the samples E528, H687 and M810. The effect of the image input size was also analyzed. The best performing model, model 4, will be used for comparison with the next generation models.

Table 3.4: Summary of the first generation models.

Model	Number of training images	Training input size	Validation IoU	Shading correction
1	515	256 x 256 px	0.9211	No
2	515	512 x 512 px	0.9133	No
3	515	256 x 256 px	0.9193	Yes
4	515	512 x 512 px	0.9109	Yes

The data collected during the tests was used to adjust the training parameters for the next generation models. The best segmentation results, including images taken under the aforementioned conditions, were used as input masks for training. The second-generation models are shown in the table 3.5.

Table 3.5: Summary of the second generation models

Model	Number of training images	Training input size	Validation IoU	Shading correction
5	629	1024 x 1024 px	0.7840	No
6	629	768 x 768 px	0.8839	No

The second-generation models were tested with unseen images from the samples E528, H687 and M810. The image input size was fixed to the closest multiple of 128 px and the shading correction was eliminated. The best performing model of the generation, model 6, will be further used for comparison with other generations models.

The best segmentation results were one more time used to train the third-generation models. In some cases, the masks were manually corrected using GIMP software [69]. A summary of the third-generation models can be seen in the table 3.6.

Table 3.6: Summary of the third generation models.

Model	Number of training images	Training input size	Validation IoU	Shading correction
7	760	768 x 768 px	0.8490	No
8	760	768 x 768 px	0.8917	No

These models were tested using images from the unseen samples 1311, 1317, 1449, 1453, B250 and C925. The best performing model, model 8, will be used for comparison as well as for quantitative microstructural analysis.

3.5 Quantitative microstructural analysis

For each sample, images from one microscope and one magnification were chosen to perform the quantitative microstructural analysis. 4 images were utilized for every ROI. The threshold to the prediction was manually selected to optimize the results, aiming to find a balance between regions where the segmented second phase object edges cover parts of the matrix, and areas where the opposite happens. Moreover, with higher threshold values an increased number of particles are detected. This can both improve the segmentation quality or introduce artefacts. It is important to note that since the threshold operates on the matrix prediction, it does not interfere with the second-phase classification. This means that, for example, if a pixel is classified as pearlite before thresholding, it may be reclassified as matrix afterwards, but never as bainite/martensite. A summary of the image selection and the threshold values can be seen in the table 3.7.

Table 3.7: Acquisition and processing parameters for quantitative microstructural analysis.

| Sample	Microscope	Magnification	Threshold
1311	Zeiss axio imager.M2m	500x	0.4
1317	Zeiss axio imager.M2m	500x	0.3
1449	Zeiss axio imager.M2m	200x	0.12
1453	Zeiss axio imager.M2m	200x	0.12
B250	Zeiss axio imager.M2m	200x	0.35
C925	Zeiss axio imager.M2m	200x	0.35

3.5.1 Morphological parameters calculation

Different morphological parameters were calculated from the segmentation mask, using the region properties algorithms from the Scikit-image library [70]. For each microscope, a pixel to µm conversion factor was computed. The object shown in figure 3.19 will be used as demonstration of the calculation.
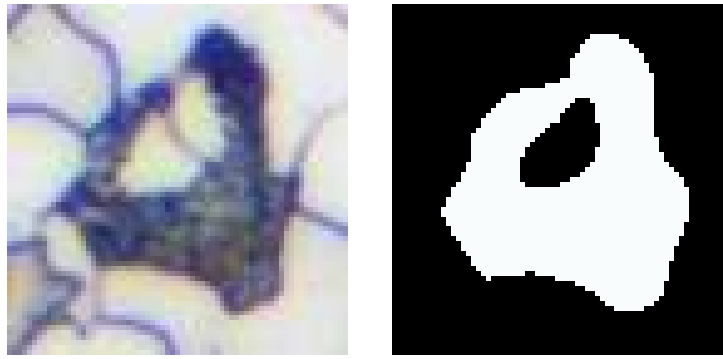
(a) LOM   (b) Segmentation mask

Figure 3.19: Sample pearlitic object. Sample C925.

The selected parameters are:

- Area: Three area-related parameters were calculated, as shown in figure 3.20. The area of the region, given by the number of pixels, the filled area, which is the area of the region with all the holes filled in and the convex area, which is the area of the smallest convex polygon that encloses the region.
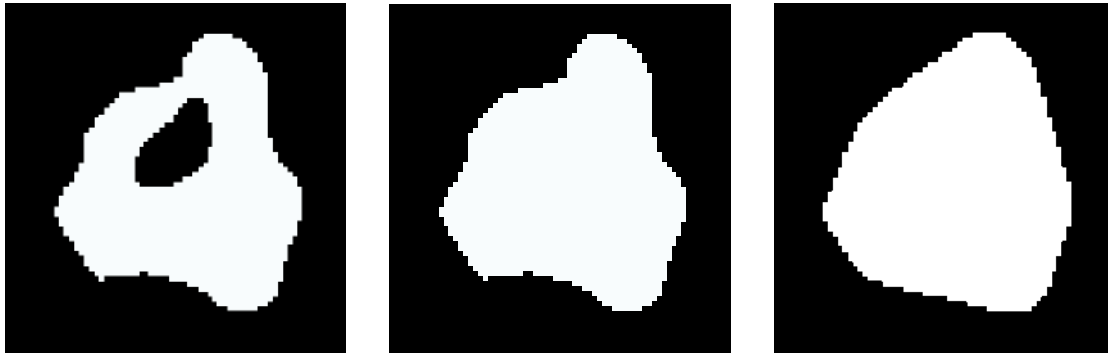
(a) Area   (b) Filled area   (c) Convex area

Figure 3.20: Different area-related parameters calculation (white areas).

- Perimeter: The perimeter of the object approximates the contour as a line through the centers of border pixels using a 4-connectivity. As shown in figure 3.21, this was computed both for the region and the convex hull.

(a) Perimeter   (b) Convex perimeter

Figure 3.21: Different perimeter-related parameters calculation (red lines).

- Equivalent diameter: the diameter of a circle with the same area as the region.

$$\text{Equivalent diameter} = \sqrt{\frac{4 \cdot \text{Area}}{\pi}} \qquad (3.1)$$
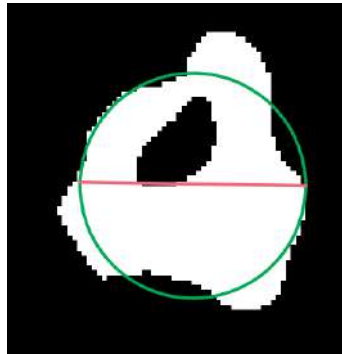

Figure 3.22: Equivalent diameter calculation (red line).

- Maximum feret diameter: the maximum Feret's diameter is computed as the longest distance between points around the region's convex hull contour.
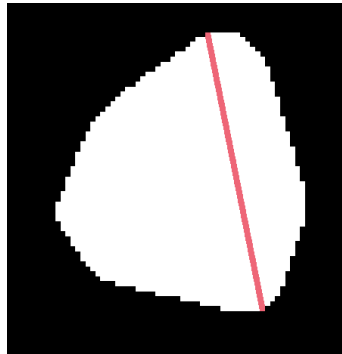

Figure 3.23: Maximum feret diameter calculation (red line).

- Axial ratio: the length of the major and minor axis of the ellipse that has the same normalized second central moments as the region were used to determine the axial ratio, as shown in equation 3.2.

$$\text{Axial ratio} = \frac{\text{Major axis length}}{\text{Minor axis length}} \qquad (3.2)$$
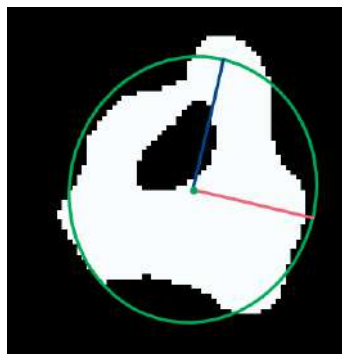

Figure 3.24: Axial ratio calculation. Blue: major axis, red: minor axis, green: ellipse.

- Orientation: defined as the angle between the horizontal and the major axis of the ellipse that has the same second moments as the region, ranging from -pi/2 to pi/2 counter-clockwise.
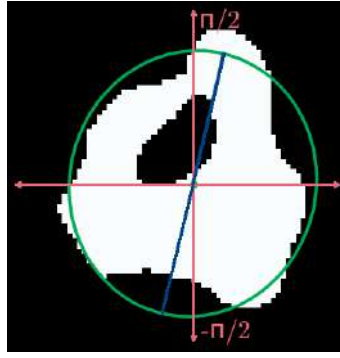
Figure 3.25: Orientation calculation. Blue: major axis, green: ellipse.

- Eccentricity: eccentricity of the ellipse that has the same second moments as the region. The eccentricity is the ratio of the focal distance (distance between focal points) over the major axis length. When it is 0, the ellipse becomes a circle.

$$\text{Eccentricity} = \frac{\text{focal length}}{\text{minor axis length}} = \sqrt{1 - \left(\frac{\text{minor axis length}}{\text{major axis length}}\right)^2} \qquad (3.3)$$

- Solidity: Ratio of pixels in the region to pixels of the convex hull.

$$\text{Solidity} = \frac{\text{Area}}{\text{Convex area}} \qquad (3.4)$$

The calculations were made twice, one considering all the objects in the image and one with clear borders, that means, that only the objects that were completely in the picture were computed.

3.5.2 Hardness testing

Hardness measurements were carried out to correlate with the quantitative results from the model prediction. 10 Vickers hardness tests were conducted on the specimens in each of the three regions of interest (S, Q and H). The test is carried out by pressing a pyramidal diamond indenter to the sample surface with a given load, according to the ASTM E92-17 standard [71]. Among the possible loads stipulated, 5 kgf was chosen to ensure an indentation size large enough to cover both constituents, attempting to minimize variance. The hardness was calculated according to the equation 3.5, where d is the average diagonal diameter of the indentation in millimeters, F the load in kgf and HV the resulting Vickers hardness. These results were used as a measure of mechanical properties to correlate the quantitative analysis from the best model results.

$$HV = 1.8544 \cdot \frac{F}{d^2} \qquad (3.5)$$

Chapter 4

Report and discussion of results

4.1   Iterative model optimization

The first-generation models had a satisfactory performance on good quality pictures. It was observed that as the testing input size increased, the results improved. However, once the original resolution of the image was reached, any further increase produced only minor differences, as it can be seen in the figure 4.1. This behaviour is related to the limitations of the scale invariance of the model. For very low testing input size, the size of the features in pixels is too big compared with the sizes used for training. Based on these observations, for the second generation models the script was modified to automatically adjust the input size to the closest multiple of 128 pixels from the original image resolution, aiming to improve efficiency, as the running time and the storage needed increased with larger input sizes.

Regarding the training input size, the best performing models were the ones with bigger training input size. However, this variable cannot be arbitrarily increased for two main reasons: first, the computational power needed increases with the training input size. Second, a larger input size translates into fewer patches produced from each image, and with limited training data, this can negatively affect the performance of the model. Therefore, an equilibrium training input size must be found to achieve the best performance.

<table>
<tr><td>(a) Input image</td><td>(b) 2048 x 2048 px</td><td>(c) 1536 x 1536 px</td></tr>
<tr><td>(d) 1024 x 1024 px</td><td>(e) 512 x 512 px</td><td>(f) 256 x 256 px</td></tr>
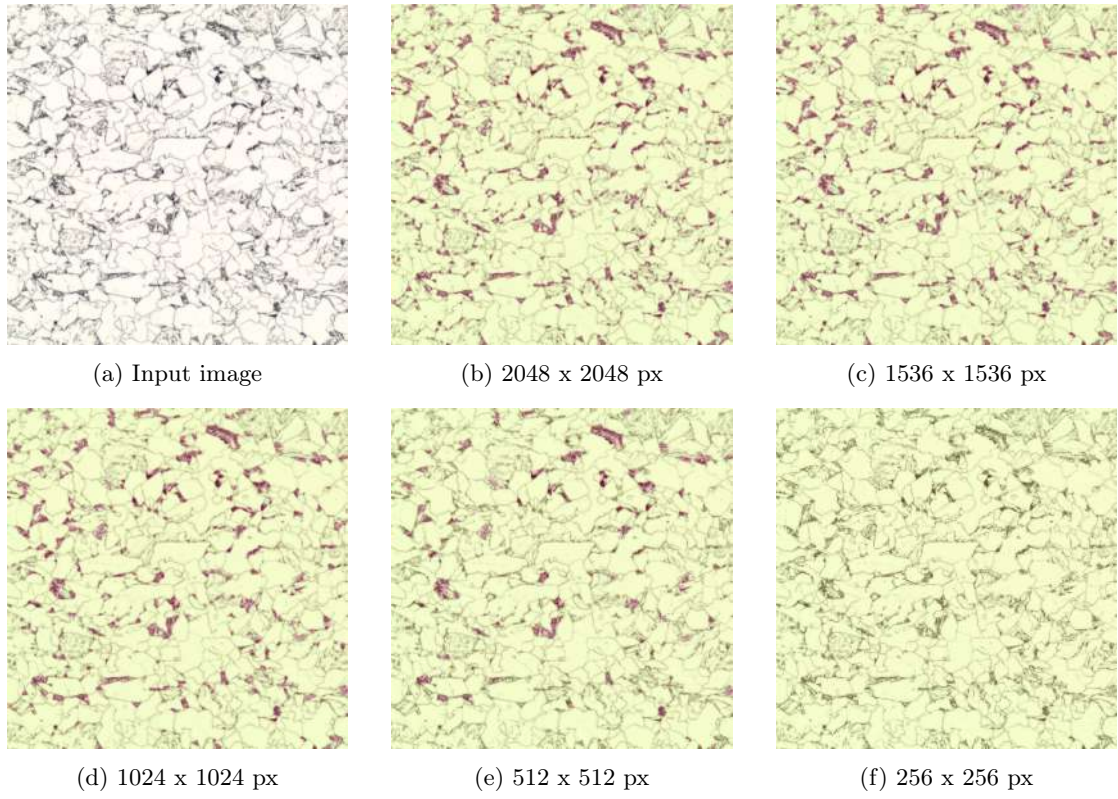</table>

Figure 4.1: Input size effect on the segmentation. Sample 6974, 200x magnification, Zeiss Axio Imager.M2m, shading correction, optimal imaging settings.
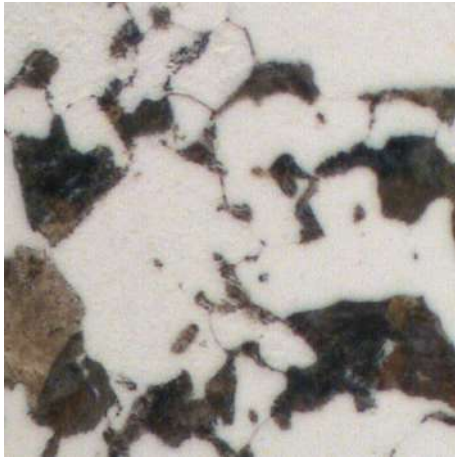
The limitations of the model were mostly related to edge detection and small particles recognition, as it can be seen in the figure 4.2. The consistency of the segmentation was also not optimal, as it can be seen on the results for the different microscopes tested in the figure 4.3.
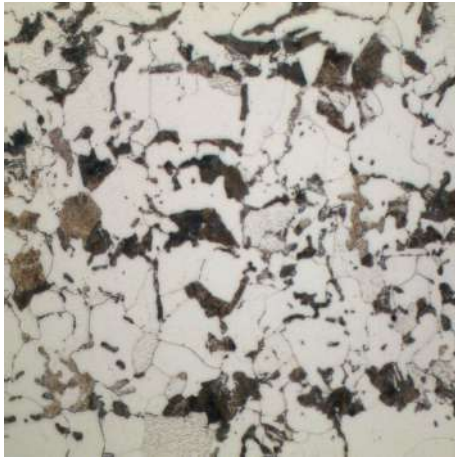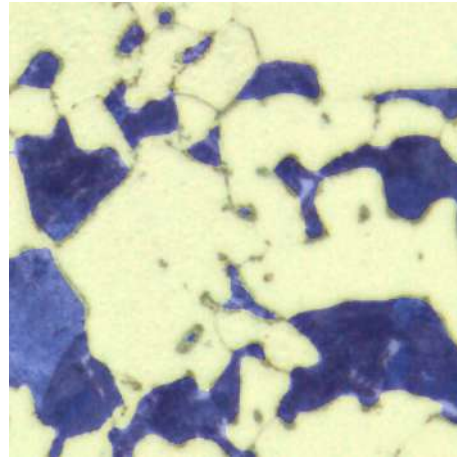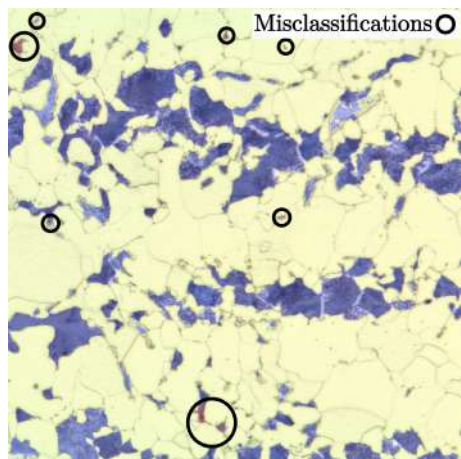
(a) Input image
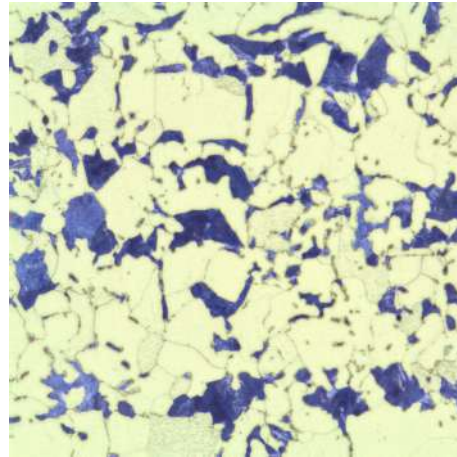
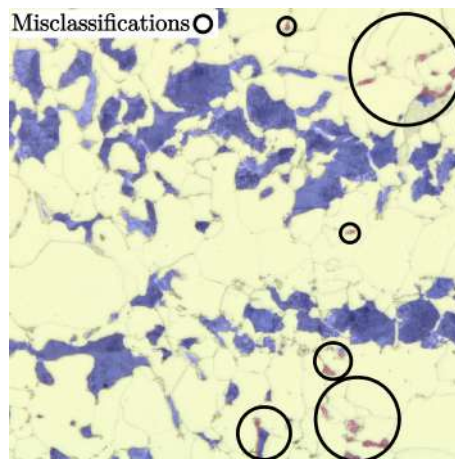(b) Segmentation

(c) Input image zoom
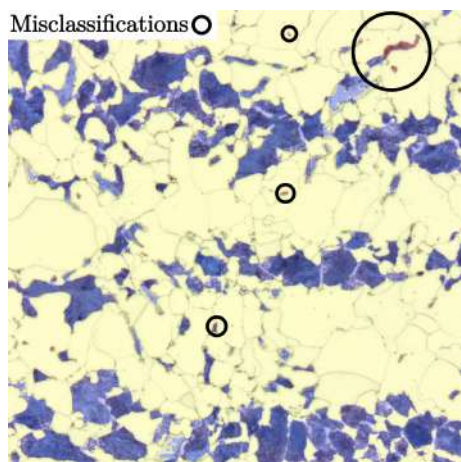
(d) Segmentation zoom

Figure 4.2: First generation segmentation results. Sample E528, 500x magnification, Nikon Eclipse L200, optimal imaging settings, 1536 x 1536 px input size.
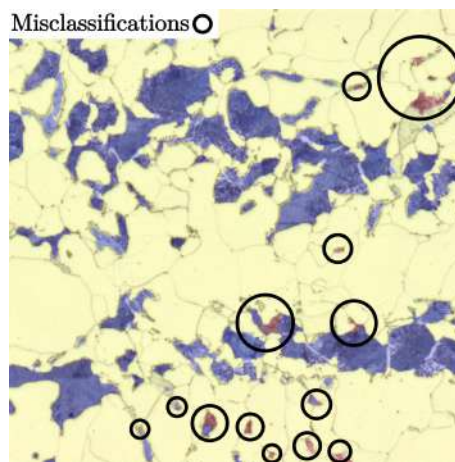
(a) Nikon Eclipse L200

(b) Reichert-Jung Polyvar MET

(c) Zeiss Axio Imager.M2m

(d) Zeiss Axio Imager.Z2m

Figure 4.3: First generation segmentation results. Sample C925, 500x magnification, 1536 x 1536 px input size.

Nonetheless the best segmentation results were used as masks to train the second-generation models. It was experimentally observed that even if the masks were not perfectly accurate, the benefit from a greater variance in the training dataset overcomes the error introduced by the miss-segmented pixels. Some examples of the images used, and the corresponding masks can be seen in the figures 4.4 and 4.5.
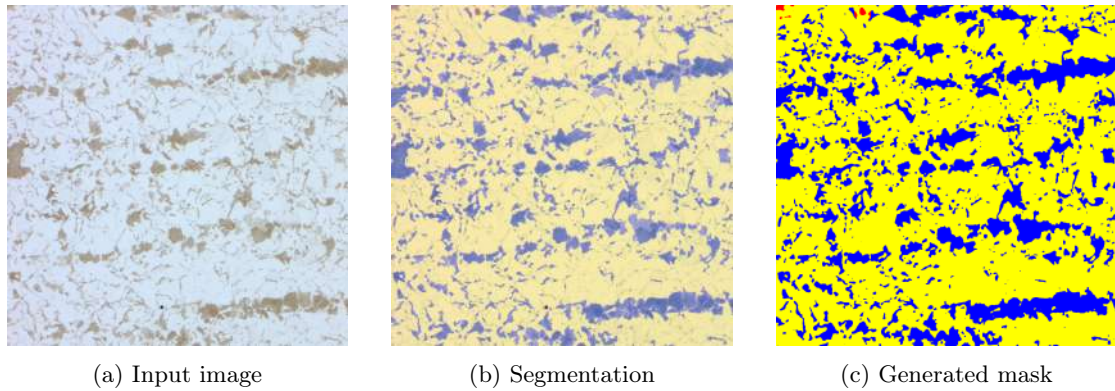

(a) Input image   (b) Segmentation   (c) Generated mask

Figure 4.4: Under etched image mask generation. Sample E528, 200x magnification, Zeiss Axio Imager.M2m.

(a) Input image   (b) Segmentation overlay   (c) Generated mask
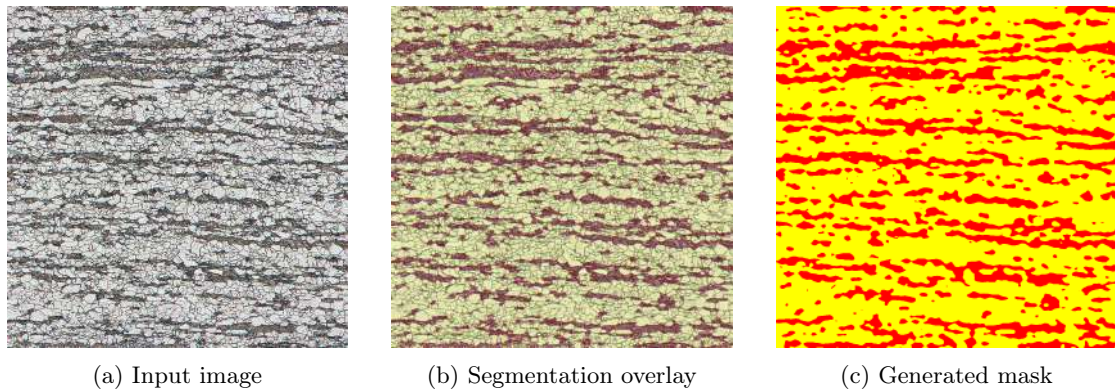
Figure 4.5: Low aperture image mask generation. Sample H687, 200x magnification, Zeiss Axio Imager.Z2m.

To train the second-generation models, bigger training input size images were used, as it was seen in the first generation that the models trained with patches of 512 x 512 px performed better than the ones with 256 x 256 px. This increase was effective due to the addition of more training data and more intense data augmentation, that allowed to achieve enough training patches to reach a good performance.

For the second-generation models, a threshold function was implemented to improve the second phase object edge detection, as it is shown in figure 4.6. Before, the pixels were assigned to the class with the highest probability. In the new version, the pixels assigned to the matrix class are defined by applying a threshold to the probability maps that the models produce as output. For example, if a threshold of 0.1 is set, every pixel with a probability higher than 10% of corresponding to the matrix class, will be assigned to this class, regardless of the existence of another class with higher probability. By doing so, the edges of the objects, where the classification was problematic, could be better adjusted.

(a) Threshold = 0.008   (b) Threshold = 0.08   (c) Threshold = 0.8

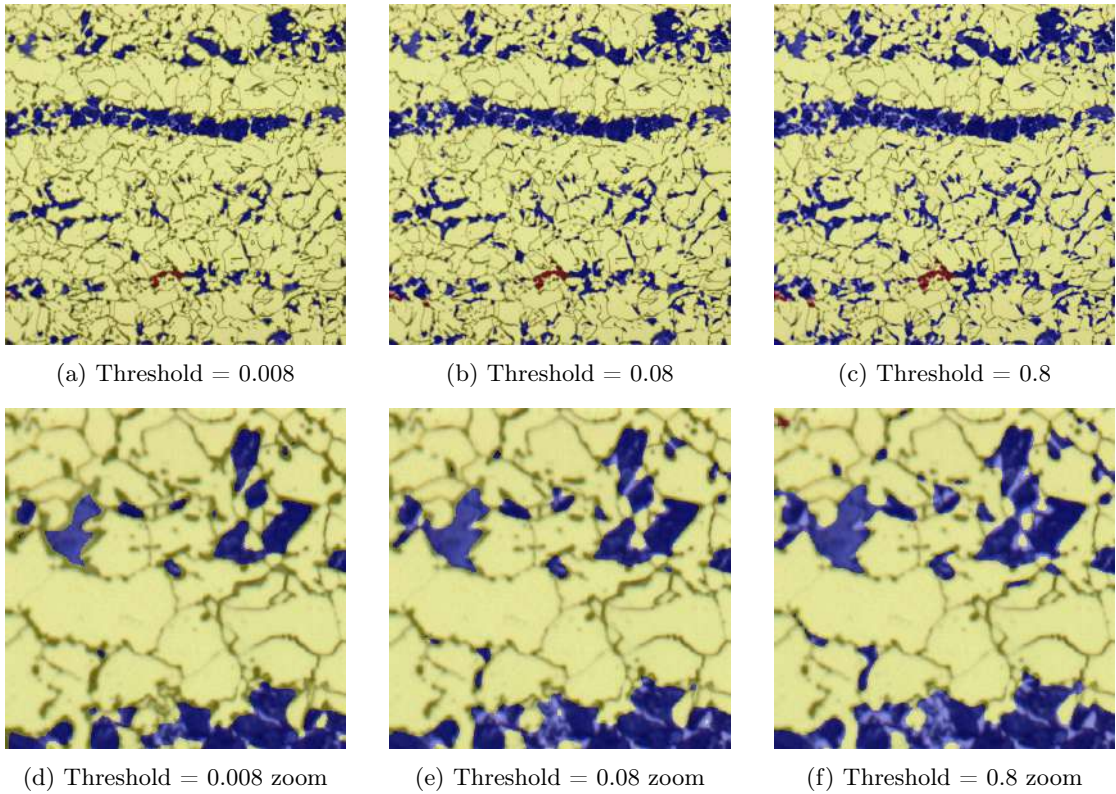(d) Threshold = 0.008 zoom   (e) Threshold = 0.08 zoom   (f) Threshold = 0.8 zoom

Figure 4.6: Threshold function effect on the model prediction. Sample E528, 200x magnification, Zeiss Axio Imager.Z2m.

Another problem with the segmentation in the first-generation models was the uneven illumination in the edges of the pictures. The figure 4.7 shows that the shading intensity is higher on the sides of the image. Considering this and that the models work with square pictures, it was decided to crop the images to be segmented in the middle instead of the side. The initial strategy was also to mitigate this problem through shading correction pre-processing. However, this process is computationally costly, even more than the segmentation itself. Moreover, the improvement of the results was not consistent and the adequate radius for background subtraction had to be manually selected and was dependent on the image resolution and the second phase object size. Therefore, it was not convenient, and it was decided to eliminate this step and aim to improve the robustness of the models by training them with a broader range of images without shading correction.

(a) Input image   (b) Shading estimated with rolling ball algorithm
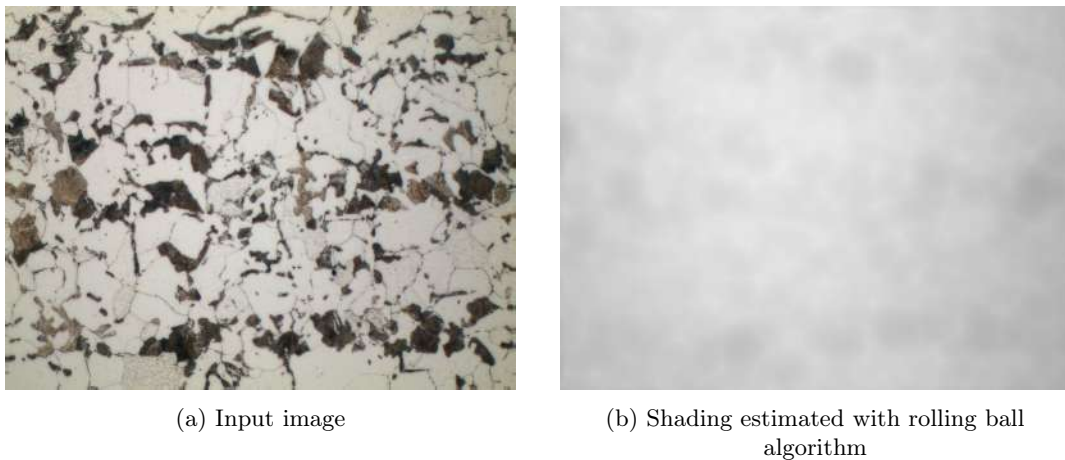
Figure 4.7: illumination distribution. Sample E528, 500x magnification, Nikon Eclipse L200.

As a result of the higher variance of the images used to train the second-generation models, their robustness improved. The second-generation models performed better than their predecessors. However, weak contrast and dark images still proved to be difficult to segment, as it is shown in the figures 4.8 and 4.9. To target this problem, hand corrected masks of images taken under these conditions were used to train the third-generation models. The same approach was used to improve the recognition of small particles. Two examples of the hand corrected masks are shown in the figure 4.10.

In this generation, the model with the smallest training input size showed a better performance. This could be a consequence of computational power limitations. To use 1024 x 1024 px patches during training, the batch size had to be reduced. As a consequence, it was probably too small to be representative of the entire data set and led to an inefficient update of the weights. Another possible reason for this can be the smaller number of patches that conformed the data set due to the higher resolution, as explained before.
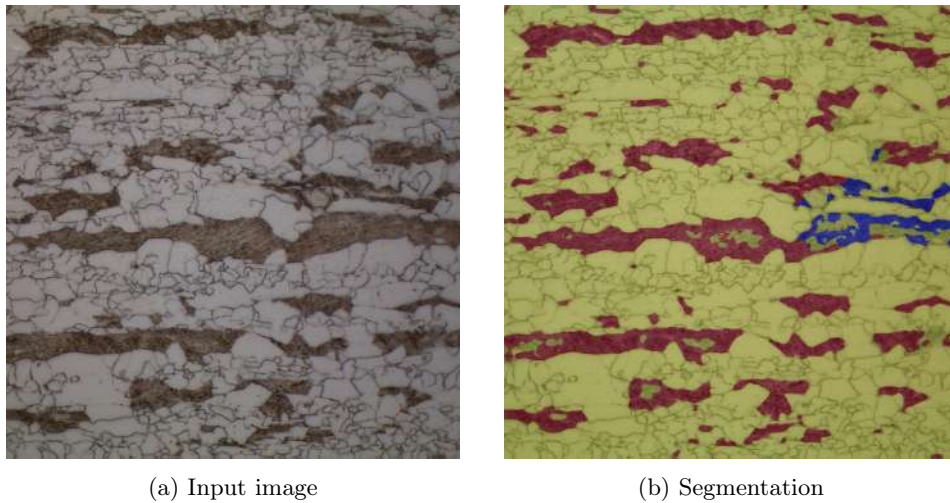

(a) Input image   (b) Segmentation

Figure 4.8: Model 6 performance in short exposure time image. Sample 1453, 500x magnification, Nikon Eclipse L200, 1536 x 1536 px input size.
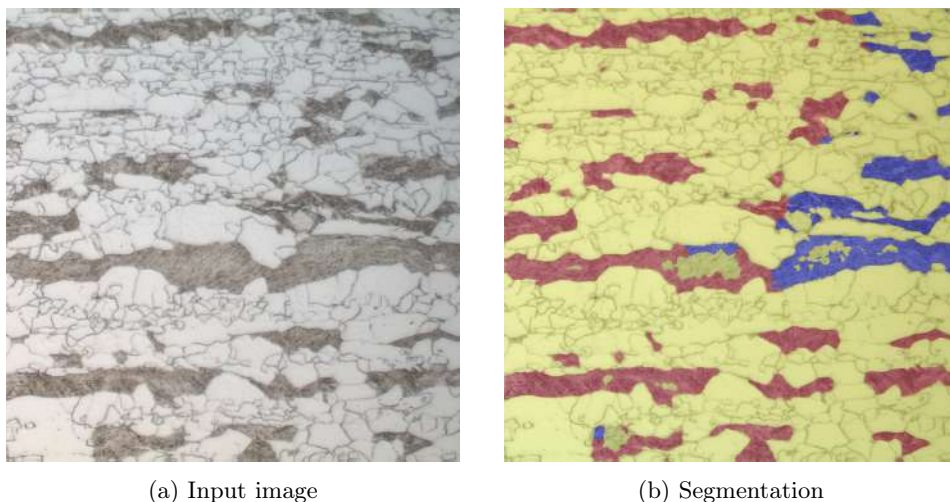

(a) Input image   (b) Segmentation

Figure 4.9: Model 6 performance in weak contrast image. Sample 1453, 500x magnification, Reichert-Jung Polyvar MET, 1536 x 1536 px input size.

(a) Input image

(b) hand corrected mask

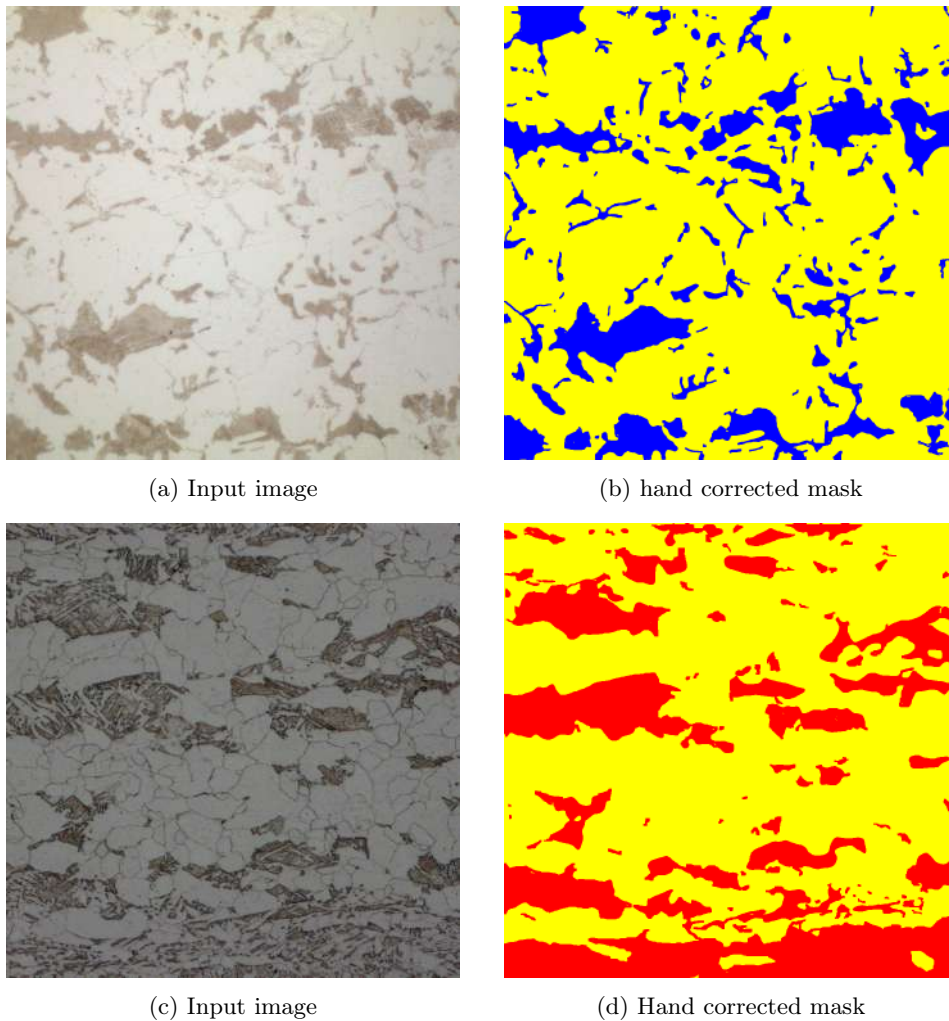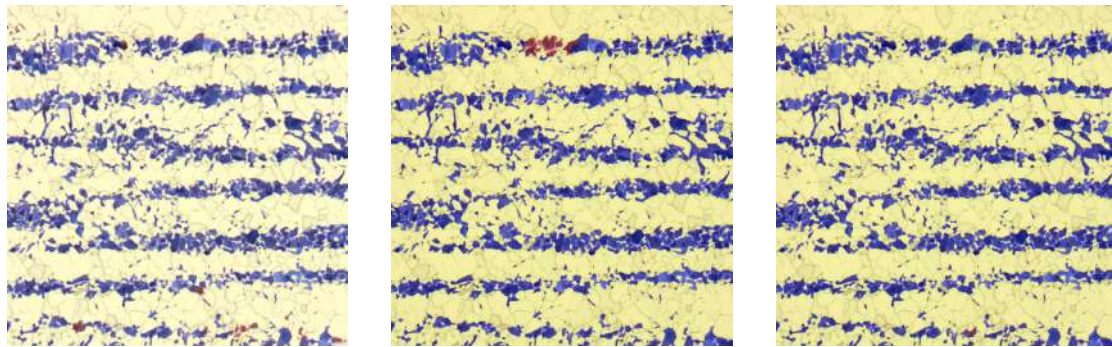(c) Input image

(d) Hand corrected mask

Figure 4.10: Not optimal images and hand corrected masks for third generation model training. Top: sample E528, 500x magnification, Nikon Eclipse L200, under etched. Bottom: Sample H687, 500x magnification, Zeiss Axio Imager.Z2m, short exposure time.

With the addition of these images to the training data set, the performance achieved by the third-generation models is superior to its predecessors. Both models were trained with an input size of 768 x 768 px, as this produced the best results in the previous generation. The main difference between the two models is the data augmentation parameters. As explained in the second chapter, data augmentation techniques make it feasible to train convolutional neural networks with fewer images. However, the transformations chosen, and their intensity must be carefully selected so that there is a wider representation of the classes without altering their identity features. For example, basic transformations such as crop, flip, and rotate contribute to the robustness of the model in relationship with scale invariance and sensitivity to image orientation. At the same time, color and contrast modifications aim to target the differences in acquisition conditions and etching intensity but must be controlled to avoid overlapping the features from the different classes, which would result in lower performance.

A comparison of the segmentation results from each generation can be seen in the figures 4.11 and 4.12. It is important to emphasize that these samples were not part of the training dataset, ensuring an unbiased evaluation of the generalization capability from the models. The misclassification of the pearlitic second phase decreased in every generation. The change from the first generation (4.11 (a)) to the second (4.11 (b)) was not as big but the elimination of the shading

correction reduces the running time, improving efficiency. For the bainitic sample the holes inside the second phase were gradually smaller at every iteration. Nonetheless, they are not completely closed in the final model.

(a) Model 4   (b) Model 6   (c) Model 8

Figure 4.11: Segmentation results from the different models on the same input image. Sample C925, 200x magnification, Zeiss Axio Imager.M2m, optimal imaging settings.
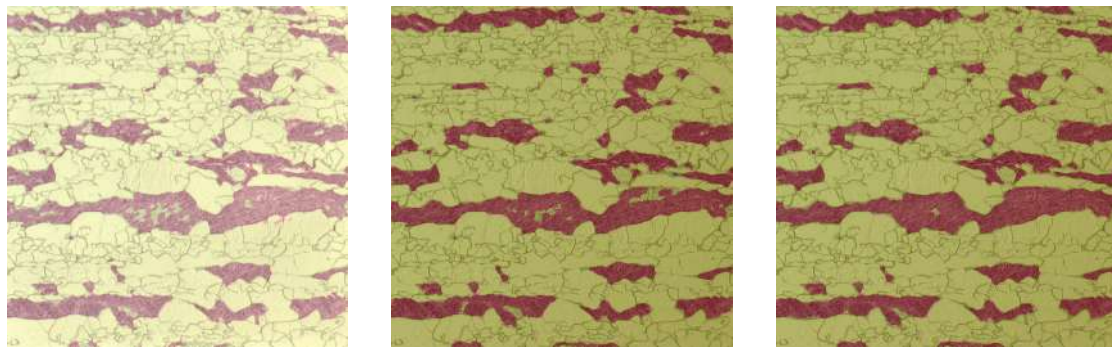
(a) Model 4   (b) Model 6   (c) Model 8

Figure 4.12: Segmentation results from the different models on the same input image. Sample 1453, 500x magnification, Zeiss Axio Imager.Z2m, low aperture.

The last model performs consistently good, as it can be seen in the figures 4.13 and 4.14. The segmentation is accurate in almost every condition tested. The exception is the 1000x magnification. One possible explanation for this is that the training data set did not include 1000x magnification images, and the model was not able to generalize the features from the other magnifications to this range. Furthermore, the sharpness of the micrographs taken at this magnification was never as good as with the other lenses, probably because of the smaller working distance and increased optical aberration. One possible way to improve the performance at 1000x would be to include it within the training data. However, the regions captured are too small to be statistically representative of the microstructure. Therefore, it was not included.

There are no misclassifications for the bainitic sample (1453). For the pearlitic sample, the algorithm falsely detected a 0.1% of bainite and martensite in the picture from Zeiss Axio Imager.M2m 200x, 0.3% in the short exposure time image and 13,6% in the 1000x.
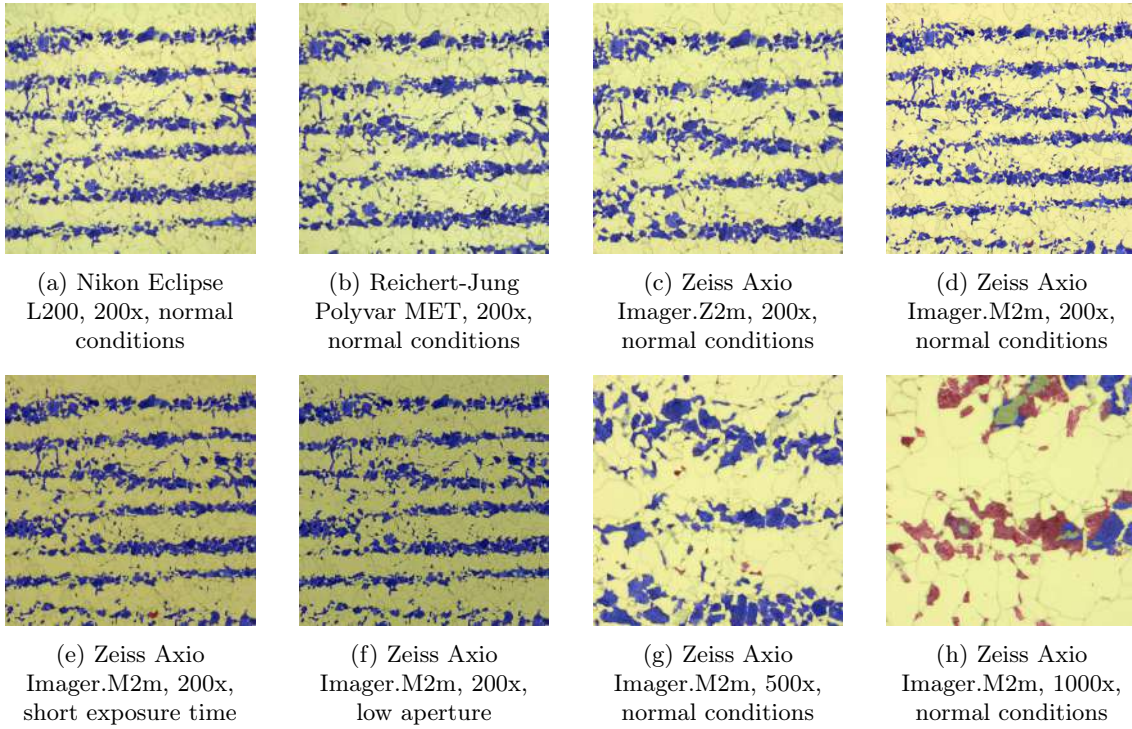
(a) Nikon Eclipse L200, 200x, normal conditions

(b) Reichert-Jung Polyvar MET, 200x, normal conditions

(c) Zeiss Axio Imager.Z2m, 200x, normal conditions

(d) Zeiss Axio Imager.M2m, 200x, normal conditions

(e) Zeiss Axio Imager.M2m, 200x, short exposure time

(f) Zeiss Axio Imager.M2m, 200x, low aperture

(g) Zeiss Axio Imager.M2m, 500x, normal conditions

(h) Zeiss Axio Imager.M2m, 1000x, normal conditions

Figure 4.13: Segmentation results in different conditions for the same ROI. Sample C925.

(a) Nikon Eclipse L200, 200x, normal conditions

(b) Reichert-Jung Polyvar MET, 200x, normal conditions

(c) Zeiss Axio Imager.Z2m, 200x, normal conditions

(d) Zeiss Axio Imager.M2m, 200x, normal conditions

(e) Zeiss Axio Imager.M2m, 200x, short exposure time

(f) Zeiss Axio Imager.M2m, 200x, low aperture

(g) Zeiss Axio Imager.M2m, 500x, normal conditions

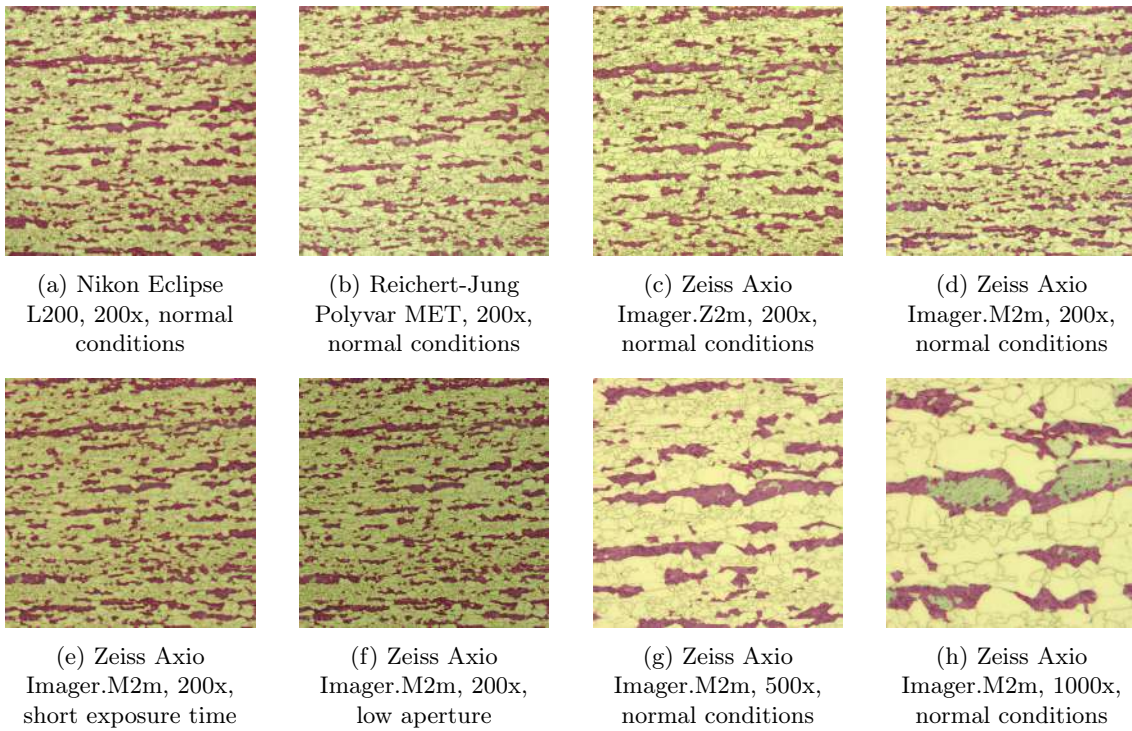(h) Zeiss Axio Imager.M2m, 1000x, normal conditions

Figure 4.14: Segmentation results in different conditions for the same ROI. Sample 1453.

The performance of the model is better at lower magnification, where it shows the highest consistency. Moreover, the defects at 500x are mostly related to big objects, which take up a considerable fraction of the image. For example, matrix holes inside the bainitic objects can be seen in figure 4.15. This is probably related to a limit in the scale invariance of the model. Even when the neural networks operate as a black box in which it is not possible to assure which features lead to the final pixel classification, the consideration of the context (surrounding pixels) is the elemental block of the convolution. Keeping this in mind, it is possible that the model associates large uniform areas with matrix class, leading to misclassification of exceptionally big objects at 500x and most objects at 1000x.

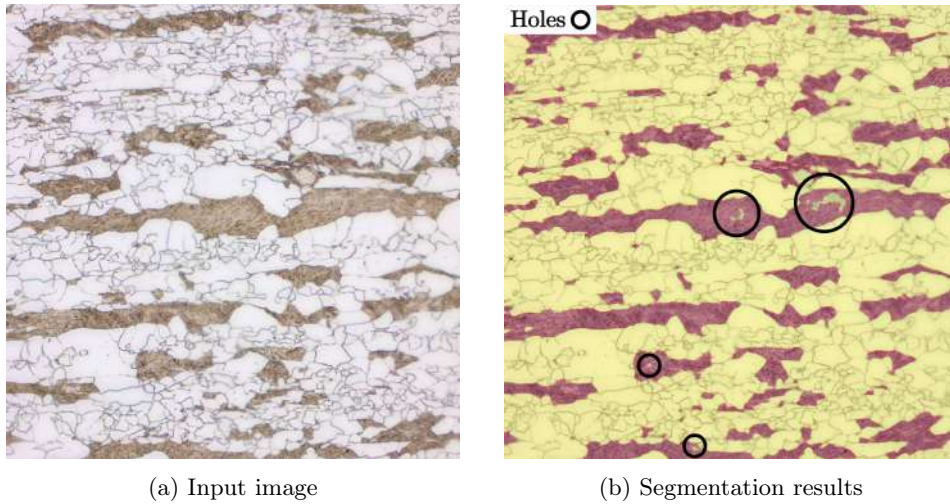(a) Input image (b) Segmentation results

Figure 4.15: Segmentation results. Sample 1453, 500x magnification, Zeiss Axio Imager.M2m, optimal imaging settings.

In most cases, the estimated second phase fraction is higher at lower magnification. This could be related to the capability of the model to distinguish close objects from the matrix. At 200x, matrix regions in between objects are sometimes classified as second phase, as it can be seen in the figure 4.16.

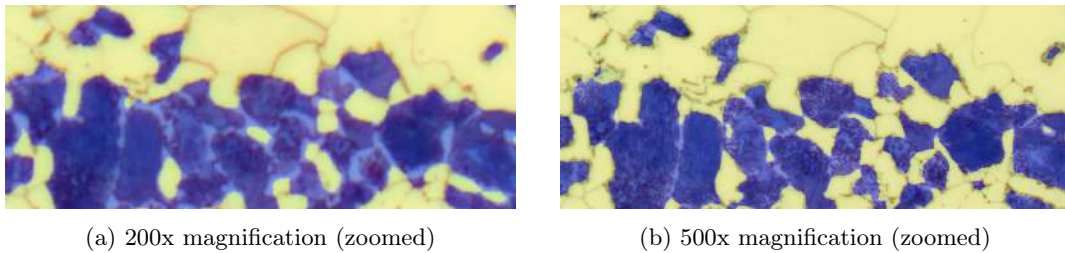(a) 200x magnification (zoomed) (b) 500x magnification (zoomed)

Figure 4.16: Segmentation results. Sample C925, Zeiss Axio Imager.M2m, optimal imaging settings.

Nonetheless, the segmentation results in two different magnifications, for different microstructures, microscopes, and acquisition conditions are very consistent, as it can be seen in the figure 4.17 and 4.18. Moreover, part of this variation can be attributed to the difference in the field of view from the camera-optical system of the different microscopes used.
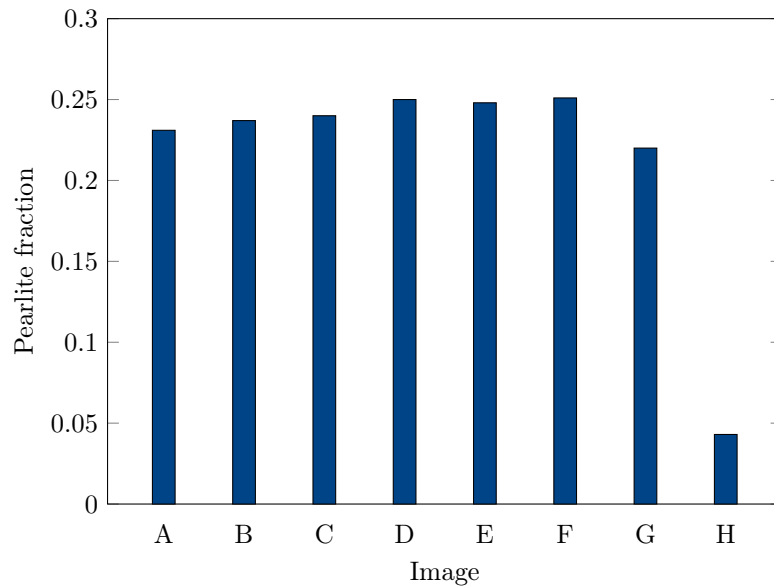
Figure 4.17: Pearlite fraction in different acquisition conditions images. Sample C925. The letters correspond to the images shown in the figure 4.13.
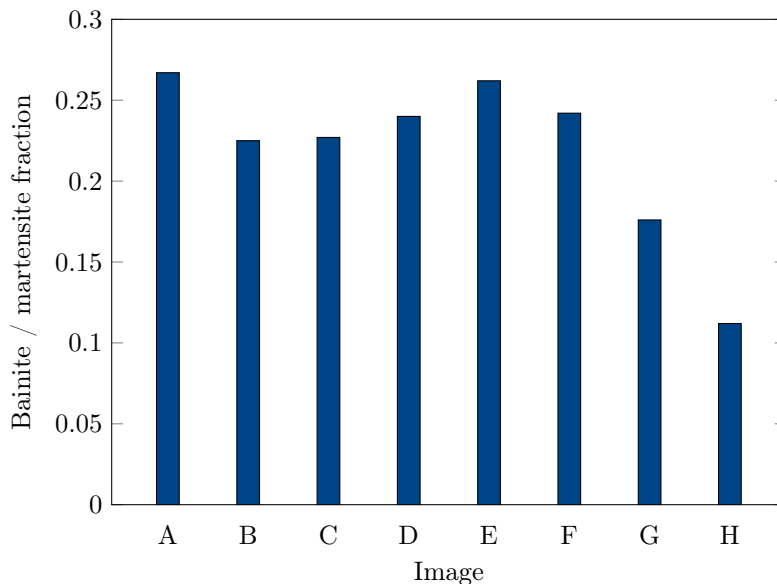

Figure 4.18: Bainite / martensite fraction in different acquisition conditions images. Sample 1453. The letters correspond to the images shown in the figure 4.14.

Although the performance of the last model is good, there are some cases where the results are not optimal. For example, in the figure 4.19, the misclassifications are mostly concentrated in objects that are not as dark as the typical pearlitic object. And the lamellas cannot be seen in any of the cases. It is possible that these errors may be due to the absence of objects with those characteristics in the training data, and that the model's generalization capability is not sufficient to recognize them. It can also be seen that the model considers the surroundings of the object for the classifications. As a result, if one object is classified as bainite, it is much more likely for the objects around it to also be misclassified as bainite. Examples of this can be seen in figure 4.20. In the case of 4.20 (b) the light appearance of the center of the second phase objects and its weaker contrast with the surrounding leads to the recognition as bainitic of the adjacent objects. In 4.20 (d), instead, the central object is recognized as bainite as well as the surroundings. These results

can be explained by considering how CNNs function: as the information flows through the layers, the down sampling of the feature maps helps to detect features on a bigger scale, as the filters cover a bigger fraction of the original image. However, this may also lead to the loss of the details of the location of the object [72]. U-NET specifically targets this problem by introducing the skip connections that concatenate the early feature maps with the later ones. However, as can be seen from these results, a negative influence from the context is still observed in some cases.
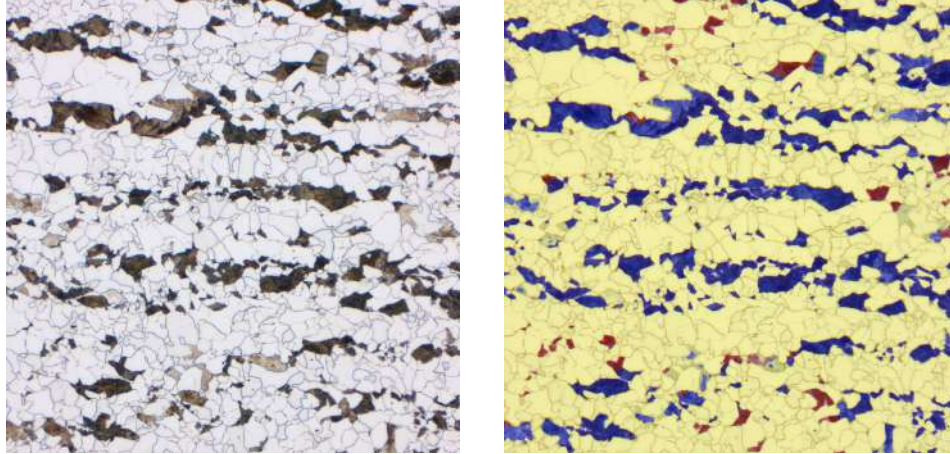
(a) Input image   (b) Segmentation

Figure 4.19: Model 8 performance. Sample B250, 200x magnification, Zeiss Axio Imager.M2m, 1536 x 1536 px input size.

(a) Input image   (b) Segmentation results

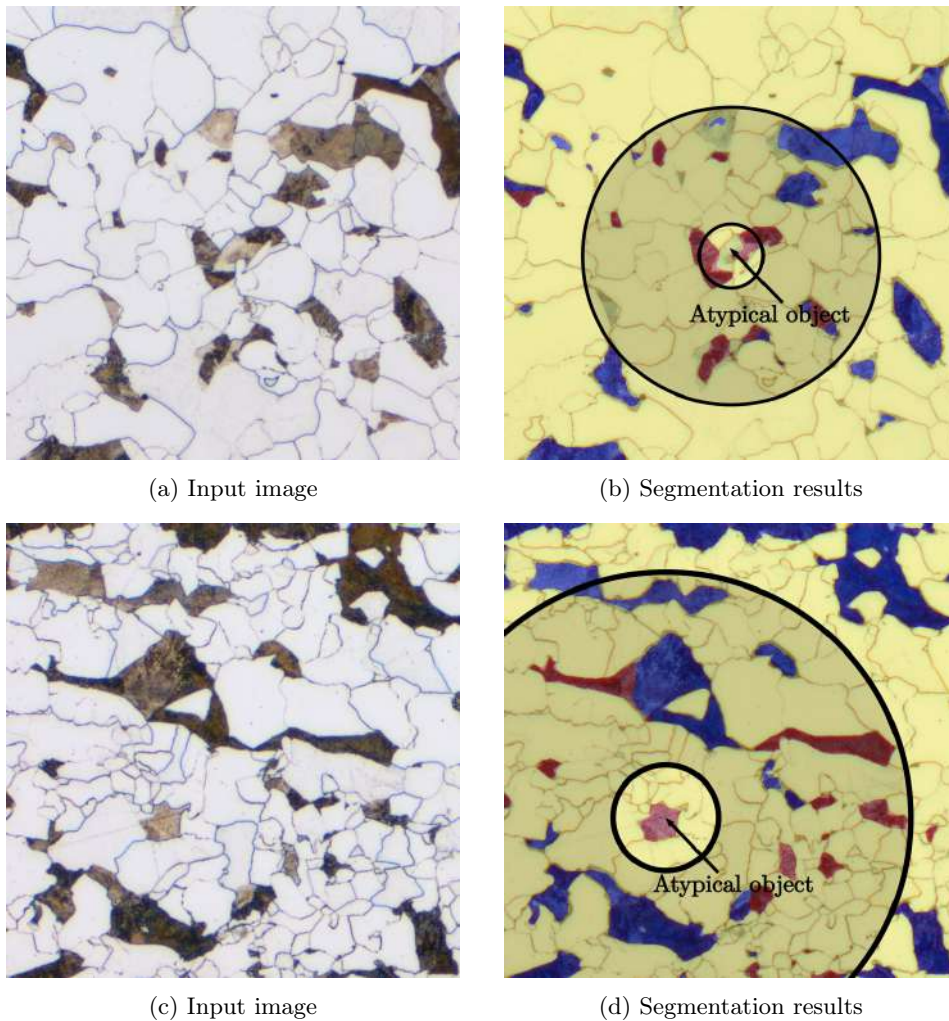(c) Input image   (d) Segmentation results

Figure 4.20: Segmentation results. Sample B250, 200x magnification (zoomed), Zeiss Axio Imager.M2m, optimal imaging settings. Green circles indicate atypical object and area of influence.

The use of high-resolution images as input also proved to give worse segmentation results than the lower resolution images. This can be attributed to the size of the features in pixels, which is very different as the resolution is higher. Another possible reason for this is that the camera uses a scanning color mode [73] to produce higher resolution images. This technology takes multiple pictures moving one pixel at a time allowing to capture RGB information for every pixel, leading to a higher resolution. However, this method is also very susceptible to displacements of the set-up during the micro scanning. The different acquisition process can affect the final intensity value of the pixels. Some examples of this can be seen in the figure 4.21. Moreover, using the high resolution mode results in pixel sizes smaller than the LOM resolving power, as it can be observed in the table 4.1. Then, it can be concluded that it does not add more detail to the picture to go beyond that point.

Table 4.1: Pixel size for Zeiss Axio Imager.Z2m microscope with Zeiss AxioCam HRc camera in different acquisition modes.

| Resolution	Pixel size (μm)	
	200x magnification	500x magnification
Standard (1388 x 1040 px)	0.33	0.13
High (4164 x 3120 px)	0.11	0.04
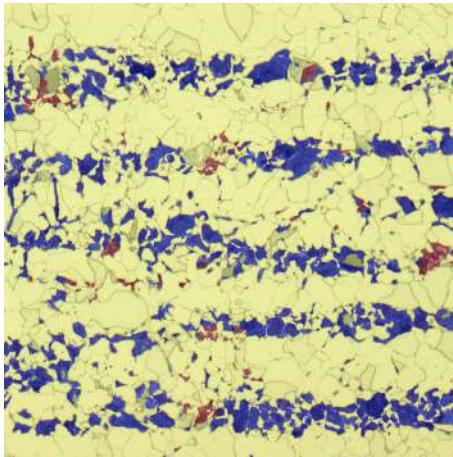
(a) 200x magnification.
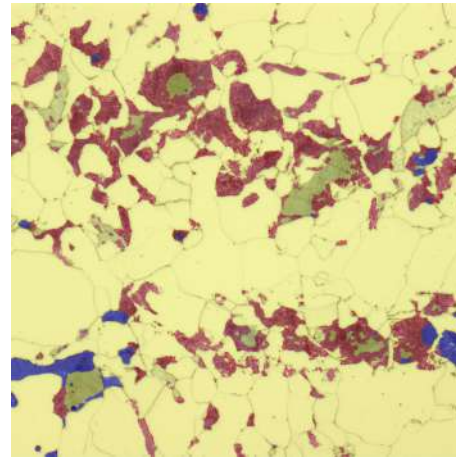
(b) 500x magnification.

Figure 4.21: Misclassifications in high resolution images from the Zeiss Axio Imager.Z2m. Sample C925.

1000x magnification images were also not correctly segmented, as it can be seen on the figure 4.22. As explained before, this might be related to the absence of instances of this magnification in the data set or to the lower quality of the images taken with these lenses.
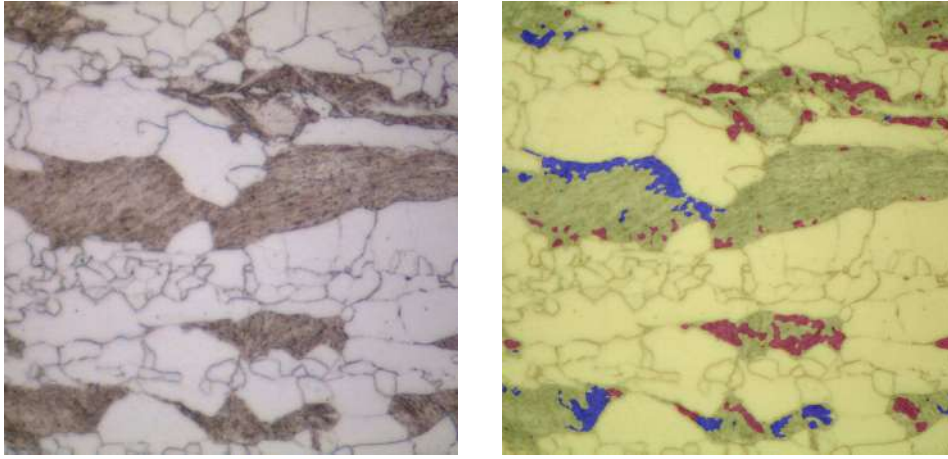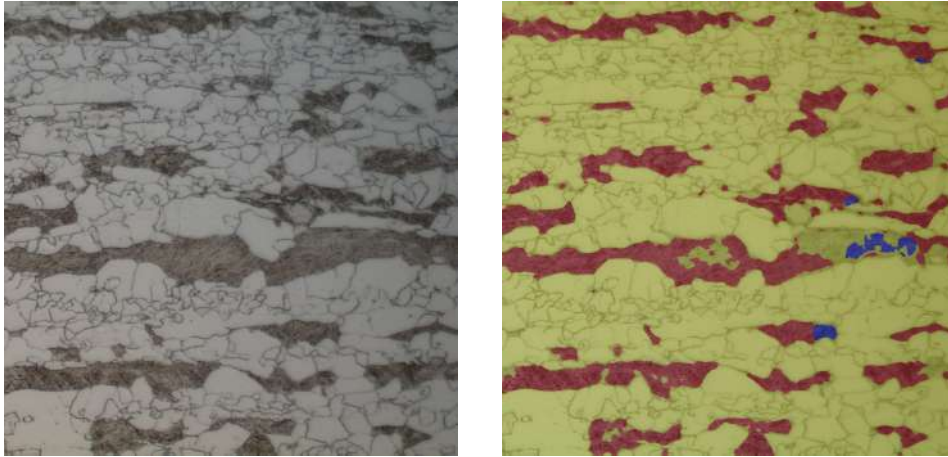
(a) Input.　　　　　　　　　　　　　　　(b) Segmentation.

Figure 4.22: Misclassifications in 1000x images. Sample 1453, Nikon Eclipse L200.

Lastly, in some cases of sub optimal images, such as the one shown in the figure 4.23, the model was not able to detect the second phase accordingly. However, given the bad quality of the micrograph, it is possible that the features of the second phase objects necessary for the segmentation are not reflected in the image.

(a) Input image　　　　　　　　　　　　(b) Segmentation

Figure 4.23: Misclassifications in bad images. Sample 1453, 500x magnification, Reichert-Jung Polyvar MET, short exposure time and under etched.

Based on these observations it is possible to conclude that the final model was able to successfully segment light optical micrographs from different microscopes and acquisition conditions consistently. Compared with the previous generations, a better detection of the second phase objects as well as less variation related to the image acquisition conditions has been observed. The cases where the performance is not as good as expected could be related to the lack of images taken under those conditions in the training data set, which shows the limit in the generalization capability of the model. Given the observed trend, it is possible that the incorporation of the last results as masks to the training data could lead to further improvement of the model in a subsequent generation.

4.2 Quantitative microstructural analysis

4.2.1 Second phase fraction

The second phase fractions for every sample, calculated from the segmentation results can be seen on the figure 4.24. The comparison between microscopes shows that the results were more consistent for the microstructures with bigger second phase objects (1449, 1453, B250 and C925), as there is less difference between microscopes and a lower standard deviation for each one. However, part of the deviation is a consequence of the inherent different second phase content on every picture, as well as from the second phase fraction difference between the different positions across the samples thickness. As explained before, the thicker the sample and the faster the cooling rate, the bigger the temperature gradient across the sample thickness during cooling. This difference is a consequence of the heat transfer process and leads to differences in the microstructure across the different positions of the sample. The figure 4.25 displays the same results but only for the quarter thickness region and 200x magnification and the deviation is lower for most of the samples. In the case of the samples 1311 and 1317, 200x magnification is not enough to resolve the microstructure, thus resulting in bigger variations, as shown in figure 4.26. In all cases, only images taken under optimal acquisition conditions were considered (four images for each ROI and microscope).
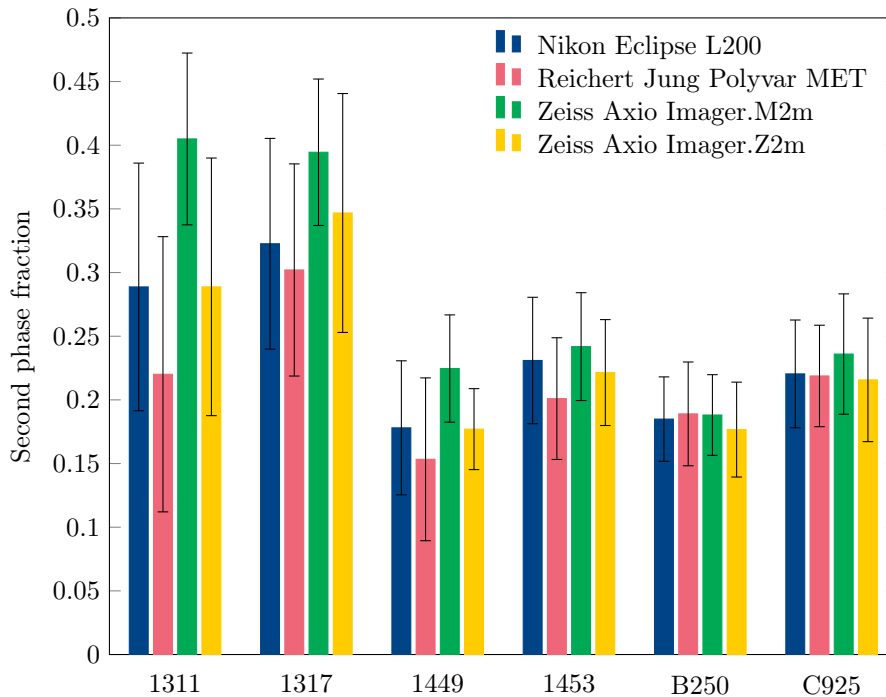

Figure 4.24: Second phase fraction and standard deviation calculated from the selected segmented images for every sample and microscope.
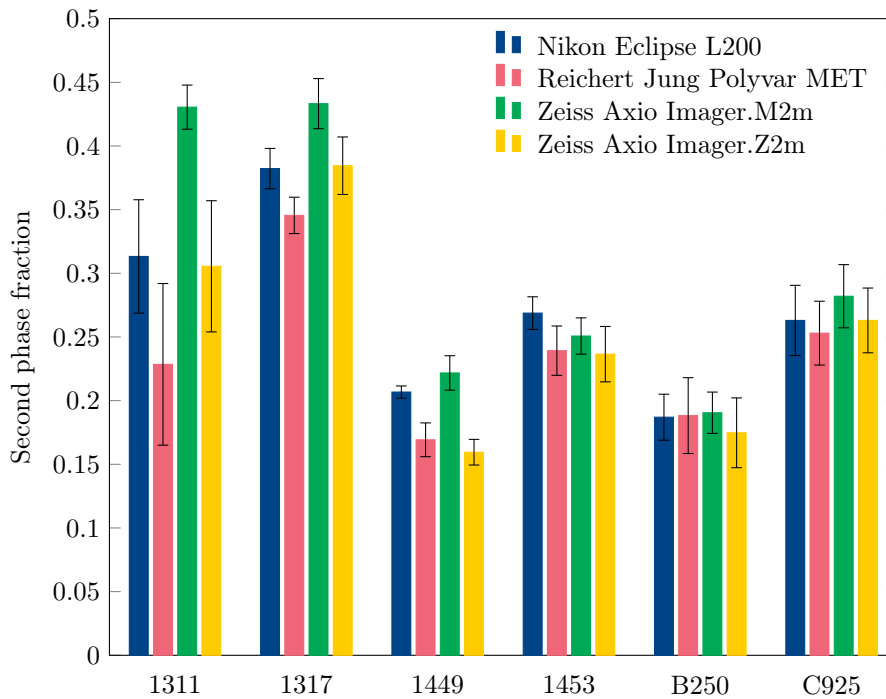
Figure 4.25: Second phase fraction and standard deviation calculated from the selected segmented images for every sample and microscope. 200x magnification, quarter thickness.
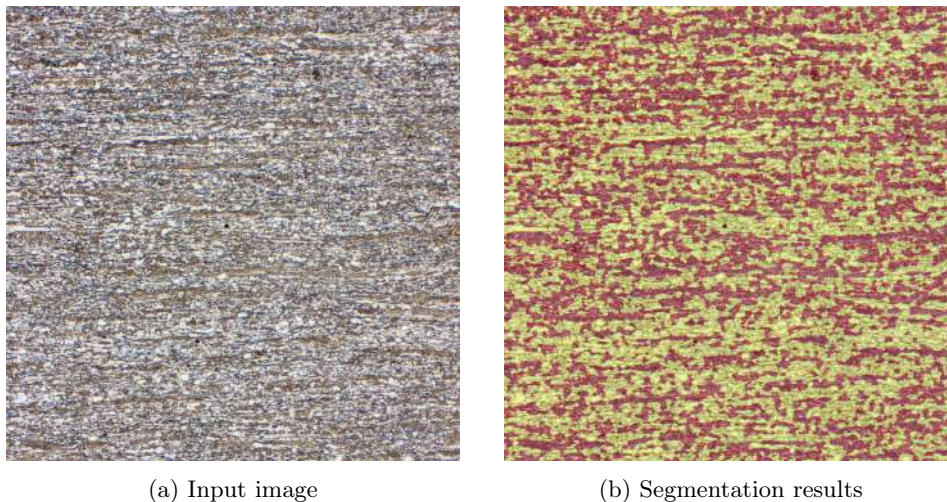

(a) Input image

(b) Segmentation results

Figure 4.26: Segmentation results in complex fine microstructure. Sample 1311, 200x magnification, Zeiss Axio Imager.M2m, optimal imaging settings.

The same trend can be observed when analyzing the effect of the different acquisition conditions, as shown in the figure 4.27. The figure 4.27 (a) shows the second phase fraction and standard deviation calculated from images including every microscope, ROI and 200x and 500x magnification. In this case, as the images portrait the exact same region (by averaging the results from every microscope) so the difference in the second phase fraction between the different conditions can only be attributed to differences in the segmentation. Nonetheless, the standard deviation is partly attributed to the different fields of view on every lens and the microstructural gradient across the sample thickness. A comparison between the segmentation results at 200x and 500x magnifications for the sample 1317 can be seen in the figure 4.28. The results at 200x are not optimal due to the limited resolution of the objects in the image.
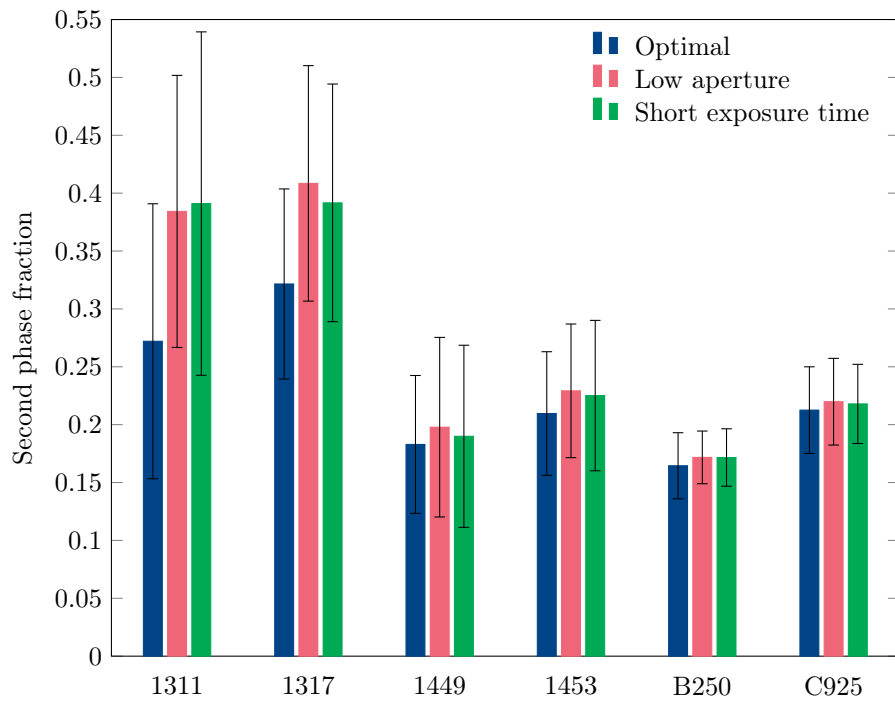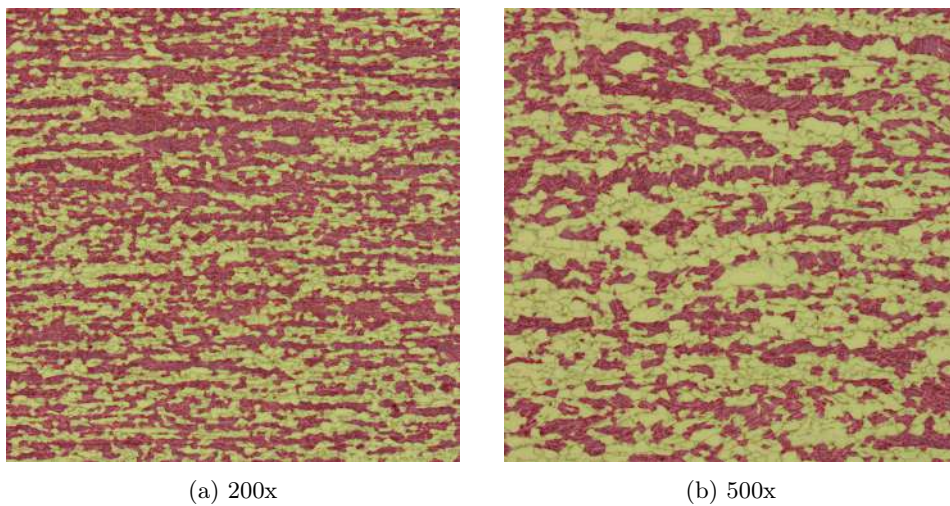
Figure 4.27: Acquisition conditions effect on second phase fraction.

(a) 200x   (b) 500x

Figure 4.28: Segmentation results in complex fine microstructure. Sample 1317, Zeiss Axio Imager.M2m, short exposure time.

In order to compare with the segmentation results, the manual point counting method was implemented, as shown in figure 4.29. A circular grid of 92 equidistant point was employed to counter the orientation effects resulting from the rolling, and the average between 4 images was calculated for every ROI with images from the Zeiss Axio Imager.M2m microscope, under optimal imaging settings. The standard suggests the utilization of a grid size close to one half of the second phase object size. However, due to the wide distribution of sizes, this was difficult to determine. The results obtained, summarized in the table 4.2, are mostly consistent with the segmentation results, confirming the performance of the model.
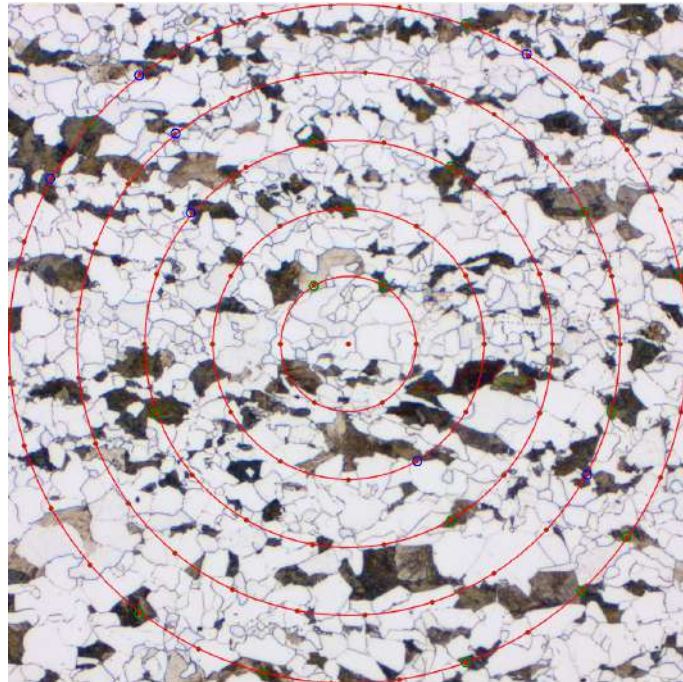

Figure 4.29: Manual point count implementation. Red dots represent the grid, blue circles indicate intersections with edges of the second phase objects and green circles intersection with second phase objects. Sample B250, 200x magnification, Zeiss Axio Imager.M2m, optimal imaging settings.

Table 4.2: Second phase fraction for every sample and position.

Sample	Position	Segmentation	Manual Point Count
1311	S	0.33 ± 0.02	0.27 ± 0.02
	Q	0.33 ± 0.01	0.32 ± 0.04
	H	0.39 ± 0.00	0.40 ± 0.06
1317	S	0.40 ± 0.03	0.37 ± 0.03
	Q	0.35 ± 0.03	0.38 ± 0.02
	H	0.31 ± 0.01	0.29 ± 0.03
1449	S	0.21 ± 0.02	0.21 ± 0.04
	Q	0.22 ± 0.01	0.24 ± 0.04
	H	0.30 ± 0.01	0.32 ± 0.02
1453	S	0.19 ± 0.03	0.25 ± 0.03
	Q	0.25 ± 0.01	0.28 ± 0.04
	H	0.30 ± 0.03	0.32 ± 0.04
B250	S	0.19 ± 0.01	0.22 ± 0.01
	Q	0.19 ± 0.02	0.24 ± 0.03
	H	0.15 ± 0.01	0.21 ± 0.02
C925	S	0.27 ± 0.03	0.32 ± 0.02
	Q	0.28 ± 0.02	0.30 ± 0.05
	H	0.25 ± 0.02	0.29 ± 0.02

As it is shown in figure 4.30, the second phase fraction intervals from both methods overlap for every ROI from the samples 1317, 1449, 1453 and C925. The largest discrepancy, for the sample B250, might be a consequence of second phase objects with a weaker contrast than the average that are sometimes undetected by the model. For this reason, the manual point count estimation might be more accurate in this case, as it yields a higher second phase fraction.

For the sample 1311 S, the manual point count method resulted in a lower second phase fraction. However, the complexity of the microstructure hindered the method's implementation. Taking this into account, it is uncertain which technique produced more accurate results for this ROI.
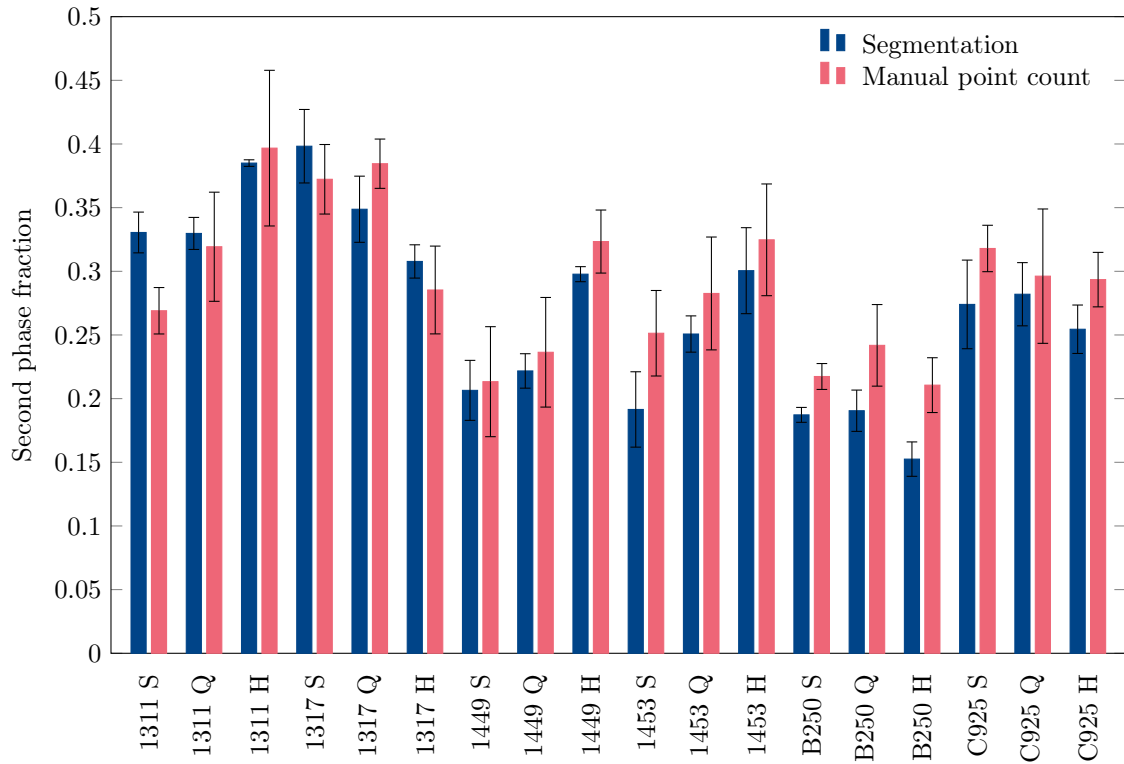
Figure 4.30: Manual point count and segmentation results comparison.

4.2.2 Morphological parameters

The segmentation results can also be used to calculate morphological parameters of the particles, where the second phase objects are analyzed individually. There are two different proposed approaches for this: with clear borders (4.31 (b)) the objects at the edges of the images are not considered in the calculation, as they are not representative of the true size and shape of the whole object. Alternatively, this criterion may be disregarded, and the parameters can be computed by considering every object (4.31 (c)).

(a) Input image   (b) Objects detected (clear borders)   (c) Objects detected (no clear borders)

Figure 4.31: Computation of second phase objects for morphological parameters calculation. Sample C925, 200x magnification, Zeiss Axio Imager.M2m

Calculations were carried out on the same 4 selected pictures for every ROI, taken under optimal imaging settings. Considering the limit of the resolving power from the LOM, particles smaller than $0.5\ um^2$ were considered segmentation artefacts and therefore filtered before the calculation. One limitation of the calculation is that objects that are adjacent to each other are segmented as one

(see Fig 4.32), as the model is trained for semantic segmentation instead of instance segmentation. This leads to a wider distribution, with clusters of particles counted as one resulting in higher averages for size related parameters.

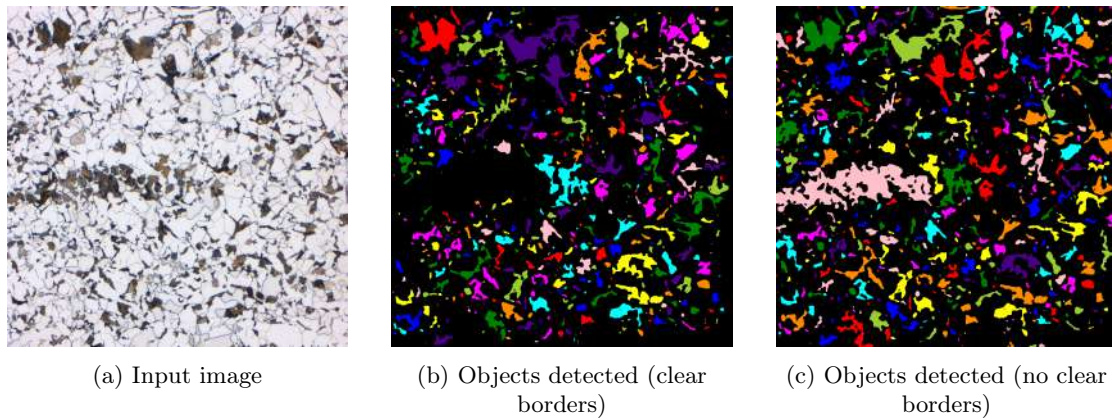(a) Input image   (b) Overlay   (c) Objects detected (no clear borders).
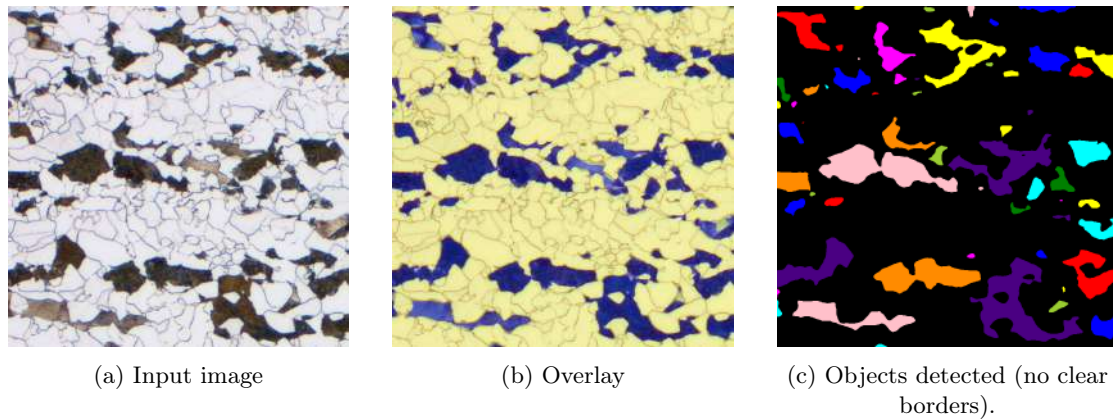
Figure 4.32: Computation of second phase objects for morphological parameters calculation. Sample B250, 200x magnification, Zeiss Axio Imager.M2m (zoomed).

The wide selection of morphological parameters is an useful tool to help characterize complex microstructures. For example, orientation and axial ratio values may influence the tensile properties in the different directions respect to rolling, and the size and distribution of the second phase objects also affects the hardness across the sample thickness, as it will be discussed in the next section. A complete report of the results for the sample C925 is shown in the appendix as reference. The distribution plots of the parameters show that the area of the objects follows a logarithmic distribution, as it is shown in figures 4.33 and 4.34. To put this data into perspective, an individual particle of the average area, orientation, and axial ratio together with the upper limit of the standard deviation is shown. While these results provide additional information about the microstructure, they would be more representative of the samples if adjacent objects were considered separately. However, the development of an instance segmentation model also constitutes one step further in the complexity of the task.

(a) Second phase object area distribution   (b) Average second phase object elliptical approximation (red) and standard deviation range (blue)
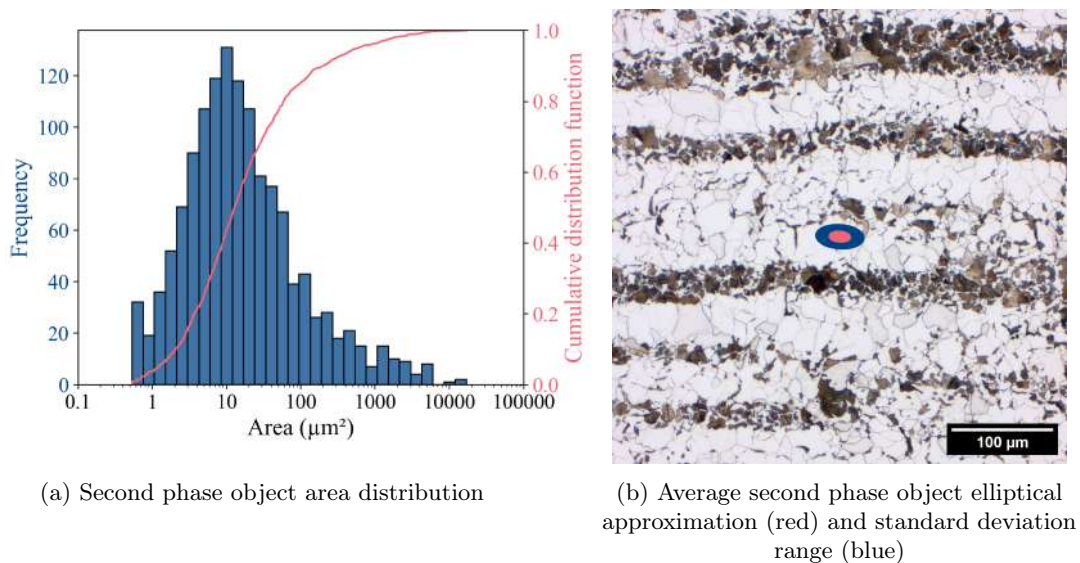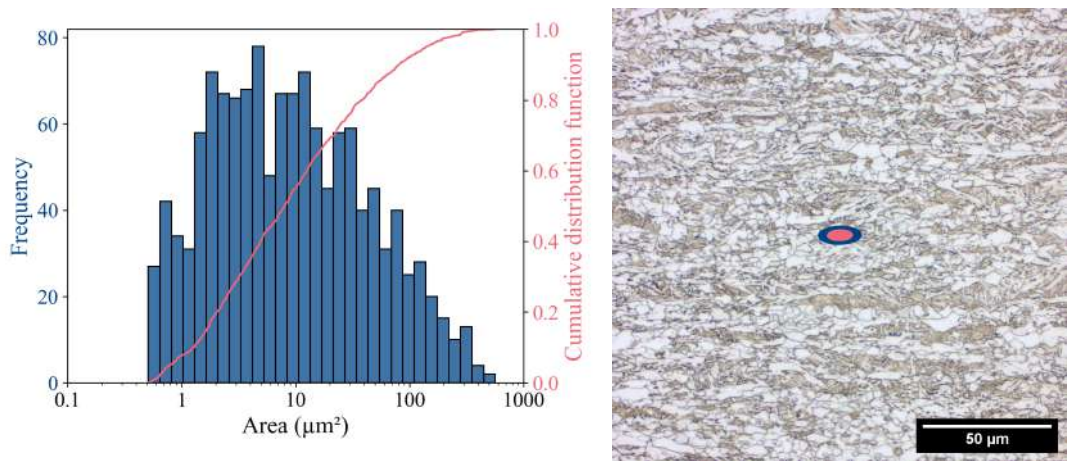
Figure 4.33: Sample C925, 200x magnification, Zeiss Axio Imager.M2m, optimal imaging settings, quarter thickness, no clear borders.

67

(a) Second phase object area distribution

(b) Average second phase object elliptical approximation (red) and standard deviation range (blue)

Figure 4.34: Sample 1311, 500x magnification, Zeiss Axio Imager.M2m, optimal imaging settings, quarter thickness, no clear borders.

4.2.3 Hardness correlations

To establish hardness correlations, the second phase fractions for every position (S, Q and H) were calculated, using the segmentation results from the Zeiss Axio imager.M2m microscope and the magnification that better suited the microstructure. For the samples 1311 and 1317, with a finer microstructure, 500x was used, whereas for 1449, 1453, C925 and B250, 200x magnification was preferred. It is important to note that for the pearlitic samples there were some misclassifications (pearlitic objects were recognized by the model as bainitic). However, the amount of second phase is accurate, calculated as one minus the matrix fraction, as shown by the comparison with the manual point count method.

Hardness tests were carried out using a 5 kgf force, to ensure an indentation size enough to cover both constituents, trying to minimize variance. The smallest indentation, in the sample 1317 had a diagonal of approximately 190 μm, which translates into a superficial indentation area bigger than 18 000 μm^2, more than one order of magnitude bigger than the highest average for the second phase object area across all the ROIs, which was 368 μm^2 measured in the sample B250. However, hardness calculations show a noticeable variance that can be partly attributed to the 3% uncertainty reported by the manufacturer of the testing machine as well as to the intrinsic variation of the microstructure from point to point.

The table 4.3 summarizes the results, including the area calculation as selected morphological parameter.

Table 4.3: Second phase fraction and object area for every sample and ROI.

Sample	Position	Hardness	Second phase fraction	Area
	S	232 ± 4	0.33 ± 0.02	31 ± 68
1311	Q	230 ± 4	0.33 ± 0.01	30 ± 58
	H	241 ± 4	0.39 ± 0.00	45 ± 161
	S	244 ± 3	0.40 ± 0.03	70 ± 252
1317	Q	230 ± 3	0.35 ± 0.03	43 ± 114
	H	219 ± 3	0.31 ± 0.01	45 ± 118
	S	207 ± 5	0.21 ± 0.02	104 ± 281
1449	Q	201 ± 3	0.22 ± 0.01	131 ± 351
	H	199 ± 5	0.30 ± 0.01	252 ± 907
	S	204 ± 7	0.19 ± 0.03	81 ± 177
1453	Q	210 ± 7	0.25 ± 0.01	157 ± 364
	H	210 ± 5	0.30 ± 0.03	285 ± 1328
	S	150 ± 2	0.19 ± 0.01	192 ± 399
B250	Q	150 ± 6	0.19 ± 0.02	368 ± 874
	H	145 ± 6	0.15 ± 0.01	304 ± 748
	S	151 ± 4	0.27 ± 0.03	100 ± 555
C925	Q	146 ± 2	0.28 ± 0.02	167 ± 873
	H	138 ± 4	0.25 ± 0.02	111 ± 688

Looking at the appearance of the microstructure from the sample B250, shown in figure 4.35, the second phase objects are smaller near the surface, with similar sizes in the quarter and half thickness. In this case, the mean second phase object area does not show a correlation with the hardness values, as shown in figure 4.36. The surface and quarter position have almost the same second phase fraction and hardness, but the lowest and highest object area, respectively. The second phase fraction, on the other hand, shows a linear correlation with the hardness values. The thickness of the plate (120 mm) and the similarity between the quarter and the center suggests that the cooling was slow, leading to a uniform second phase precipitation across the thickness, with the region close to the surface being the main difference.

Another observed characteristic from this sample is the smaller grain size near the surface. This is probably a consequence of the rolling process, where the surface experiences more plastic deformation, leading to an increased driving force for recrystallization and smaller grain size [74]. However, the current model is not able to segment grain boundaries to quantify this effect. For this reason, grain boundary segmentation can help to achieve a more integral understanding of the microstructure.
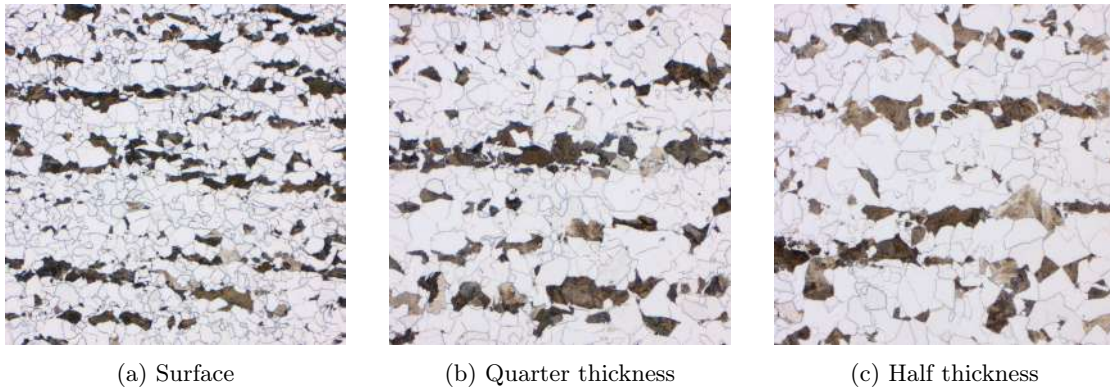
(a) Surface   (b) Quarter thickness   (c) Half thickness

Figure 4.35: Microstructural gradient. Sample B250, 200x magnification, Zeiss Axio Imager.M2m, optimal imaging settings.
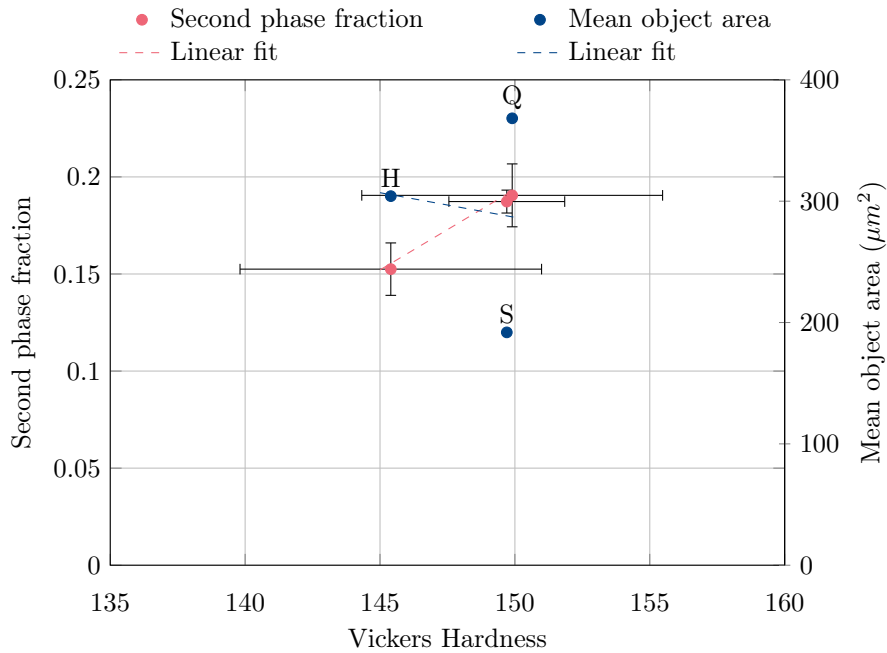

Figure 4.36: Hardness correlations with segmentation results. Sample B250.

For the sample C925 the highest hardness value is close to the surface, with the smallest objects. In this case, the limitations of the semantic segmentation translate in a higher average 8and deviation for the object size in the quarter position. As shown in the figures 4.37 and 4.38, the big clusters of pearlite are segmented as one object, resulting in a bias in the estimation towards bigger sizes. As it happened in the other pearlitic sample, B250, no apparent correlation between the second phase object area and the hardness can be established (see figure 4.39). Regarding the second phase fraction, a positive correlation can be seen, with a higher second phase fraction leading to higher hardness measurements. This observation confirms the assumption found in literature [75], [76]. The difference in second phase fraction between the surface and the quarter is small, which might suggest that the difference in hardness is a consequence of a faster cooling rate close to the surface, that leads to a smaller interlamellar spacing and a harder pearlite. This hypothesis could be evaluated by taking SEM images from the sample. Nonetheless, this is outside the scope of the current work. Moreover, smaller objects are a more effective barrier against dislocation movement, resulting in a higher hardness.
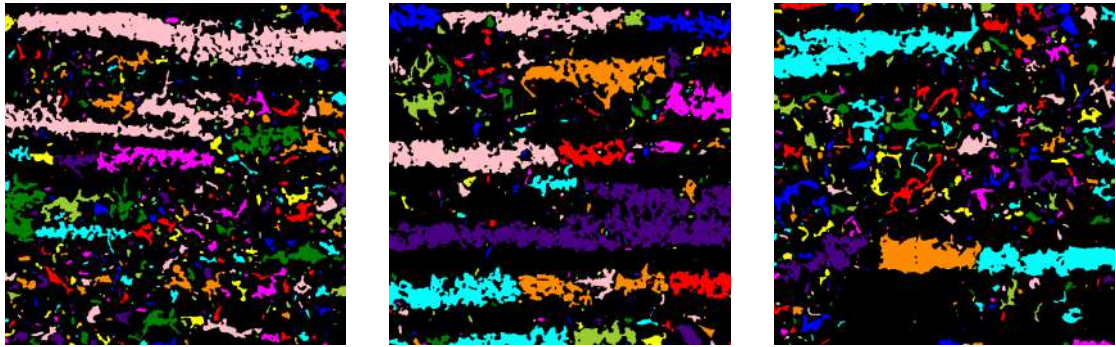
70

(a) Surface (b) Quarter thickness (c) Half thickness

Figure 4.37: Microstructural gradient. Sample C925, 200x magnification, Zeiss Axio Imager.M2m, optimal imaging settings.

(a) Surface (b) Quarter thickness (c) Half thickness

Figure 4.38: Detected second phase objects. Sample C925, 200x magnification, Zeiss Axio Imager.M2m, optimal imaging settings.
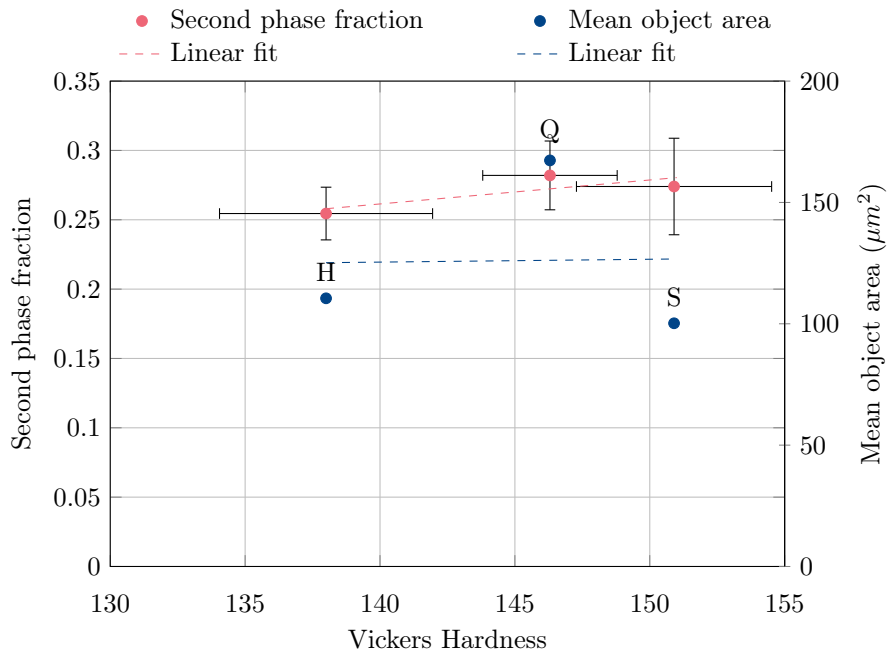
Figure 4.39: Hardness correlations with segmentation results. Sample C925.

The sample 1317 follows the expected trend, showing a linear relationship between the second phase fraction and the hardness, as shown in figure 4.42. The darker etching response in the surface (see figure 4.40) might indicate the presence of martensite, with a microstructural gradient leading to bainite in the core of the plate. This is also backed up by the higher hardness in the surface. The second phase object area measurements reflect the nature of the microstructure, with more interwoven second phase objects in the quarter-thickness position, and more separated from the ferritic background in the center of the plate. The difference with the surface, with the highest average and deviation, is also visible in the detected objects plot, shown in figure 4.41.

(a) Surface　　　　　　(b) Quarter thickness　　　　　　(c) Half thickness

Figure 4.40: Microstructural gradient. Sample 1317, 500x magnification, Zeiss Axio Imager.M2m, optimal imaging settings.

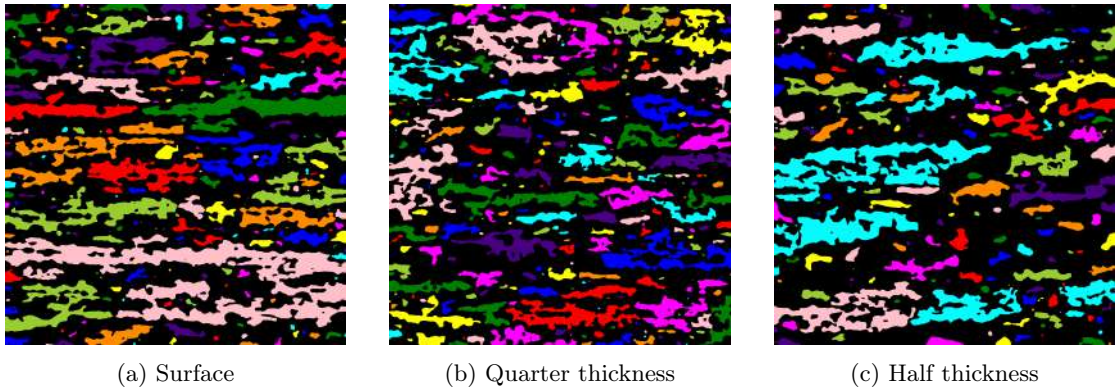(a) Surface   (b) Quarter thickness   (c) Half thickness

Figure 4.41: Detected second phase objects. Sample 1317, 500x magnification, Zeiss Axio Imager.M2m, optimal imaging settings.
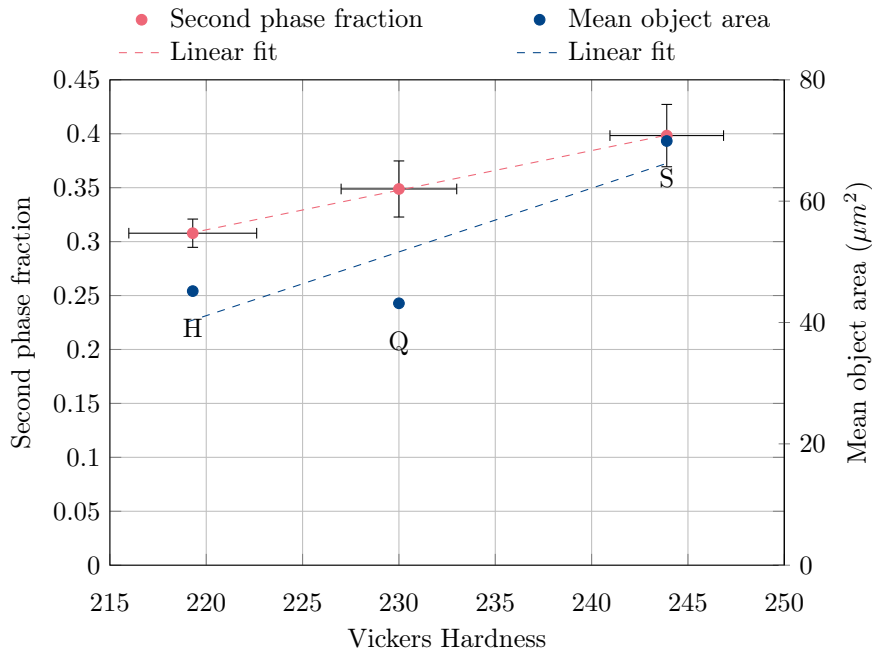

Figure 4.42: Hardness correlations with segmentation results. Sample 1317.

Sample 1311 contains the most complex microstructure from the set. The darker etching response close to the surface as well as the more defined boundaries between the second phase objects and the matrix might be indicators of a ferritic-martensitic microstructure in this region (see figure 4.43). Towards the center of the plate, the microstructure turns more complex, with highly interwoven second phase objects.

The correlations between both the mean area and the second phase fraction fit perfectly with the hardness measurements, as shown in figure 4.44. However, these results do not correlate with the expected gradient across the thickness, as the surface shows properties in between the quarter and the center values. Given the similarity in area and second phase fraction values between the surface and the quarter, the difference in hardness might be explained by a difference in the second phase constituent, backing up the idea of a martensitic surface.

The highest hardness measured in the half of the plate might be a consequence of the centerline segregation effect, with the partition of the alloying elements leading to a more complex and harder microstructure. This results in a higher second phase fraction as well as in a higher deviation of the area of the particles.

73

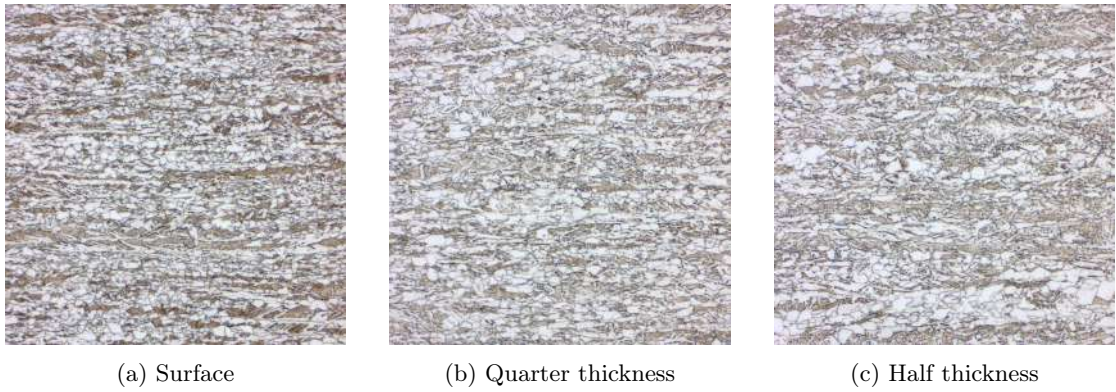(a) Surface   (b) Quarter thickness   (c) Half thickness

Figure 4.43: Microstructural gradient. Sample 1311, 500x magnification, Zeiss Axio Imager.M2m, optimal imaging settings.
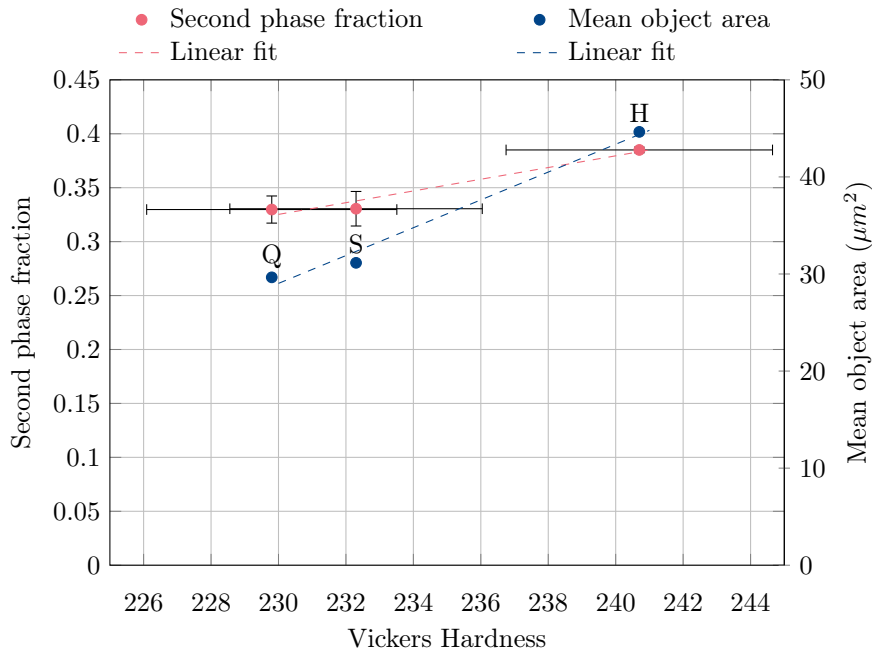

Figure 4.44: Hardness correlations with segmentation results. Sample 1311.

The images from the sample 1449, in figure 4.45, show a different etching response at the surface and bigger second phase objects towards the core of the plate. These could be indicators of a microstructural gradient, with martensitic second phase at the surface and bainite in the center. This is backed up by the hardness measurements, that show a higher hardness in the surface even though the second phase fraction is lower, as it can be seen in figure 4.46. This results in negative correlation coefficients between the hardness and the segmentation results. The smaller second phase object size in the surface probably contributes to the higher hardness in this position too.

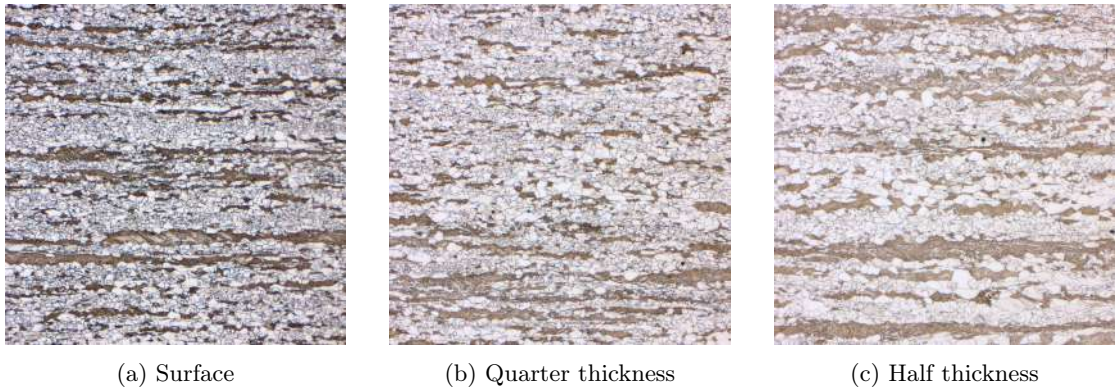(a) Surface   (b) Quarter thickness   (c) Half thickness

Figure 4.45: Microstructural gradient. Sample 1449, 200x magnification, Zeiss Axio Imager.M2m, optimal imaging settings.
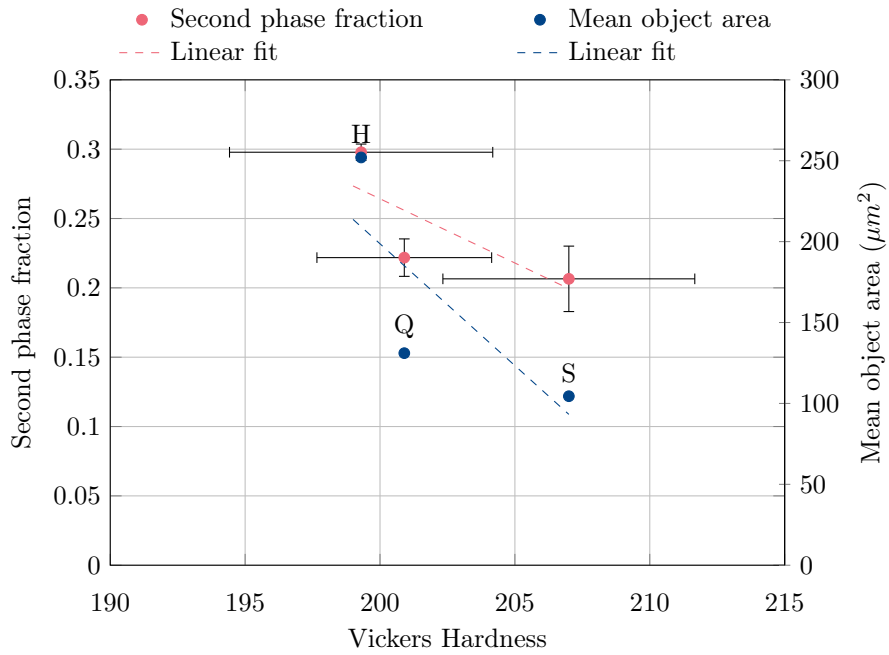

Figure 4.46: Hardness correlations with segmentation results. Sample 1449.

The appearance of the microstructure from the sample 1453 is similar to the 1449. The sample 1453 also shows a similar tendency to 1449 regarding the size of the second phase objects and the second phase fraction: they both increase with depth, as it can be seen in figures 4.47 and 4.48. Hardness on the other hand shows the opposite trend, with lower values at the surface. In this case, the influence of the centerline segregation probably explains these results. This effect was more noticeable in this sample, as it is shown in figure 4.47 (c). The concentration of solute that leads to big bands of second phase in the half of the plate could have influenced the hardness measurements, as these objects can take up a significant fraction of the indentation. This is also reflected in the object area estimation, where the mean and the standard deviation for the center of the sample is the highest among all the ROI analyzed.

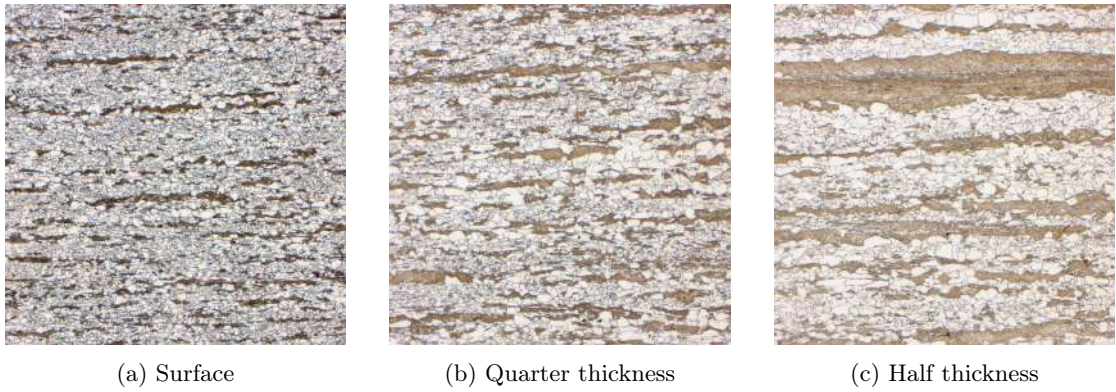(a) Surface   (b) Quarter thickness   (c) Half thickness

Figure 4.47: Microstructural gradient. Sample 1453, 200x magnification, Zeiss Axio Imager.M2m, optimal imaging settings.
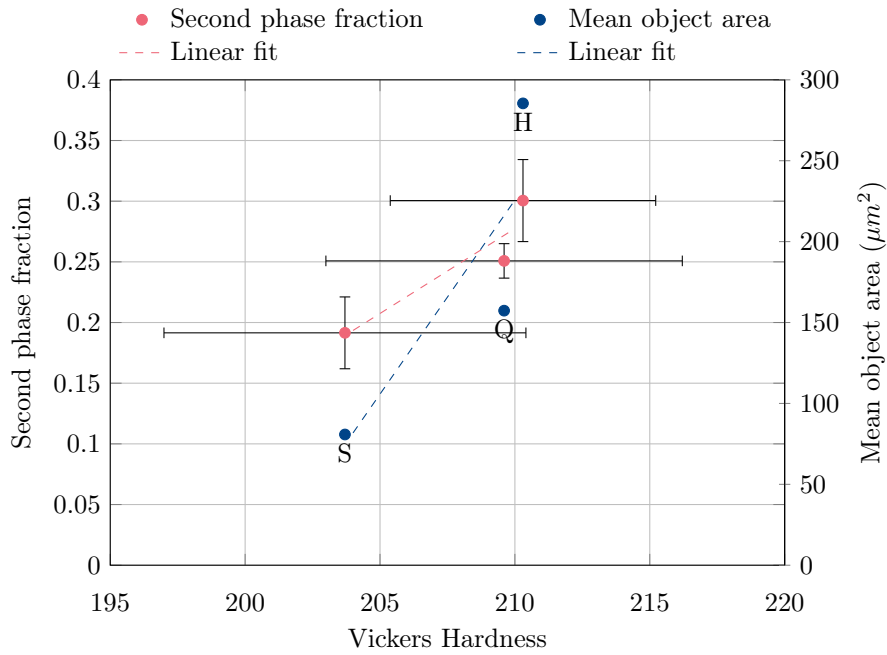

Figure 4.48: Hardness correlations with segmentation results. Sample 1453.

As shown in the figures above, these results were used to calculate a simple linear regression model between the hardness and the selected microstructural features. The linear fit equations are shown in table 4.4.

For the samples 1311 and 1317, a stronger dependence between the area of the second phase objects and the hardness was observed. This can possibly be linked to the higher complexity observed in the microstructure, with presence of difference constituents and an uneven distribution in the matrix.

In the samples 1449 and 1453, on the other hand, the second phase fraction has a higher correlation with hardness. Nonetheless, a correlation with the second phase object mean area was also observed. A possible reason for this is the interaction between two opposing effects: the segregation, leading to a higher second phase fraction towards the core, and a faster cooling at the surface that results in harder constituents. When the segregation effect prevails, as seen in sample 1453, the result is higher center hardness. On the other hand, when faster cooling dominates, as in sample 1449, the surface exhibits higher hardness.

Lastly, for the pearlitic samples, B250 and C925, the mean second phase object area did not show a correlation with the hardness values. In these cases, the second phase fraction still yielded

a good correlation fit. This behaviour can be related to a higher uniformity inside the pearlitic class, that resulted in a hardness value dependent primarily on the amount of second phase at each spot.

Table 4.4: Hardness correlations linear fit. (HV=vickers hardness, SPF=second phase fraction, A=mean object area).

Sample	Equation	R^2
1311	$HV = 173 + 176 \cdot SPF$	0.96
	$HV = 210 + 0.69 \cdot A$	0.98
1317	$HV = 135 + 272 \cdot SPF$	1
	$HV = 193 + 0.72 \cdot A$	0.76
1449	$HV = 218 - 64 \cdot SPF$	0.59
	$HV = 209 - 0.04 \cdot A$	0.61
1453	$HV = 193 + 62 \cdot SPF$	0.86
	$HV = 203 + 0.03 \cdot A$	0.71
B250	$HV = 127 + 121 \cdot SPF$	1
	$HV = 149 + 0 \cdot A$	0.01
C925	$HV = 45 + 369 \cdot SPF$	0.64
	$HV = 145 + 0 \cdot A$	0

A variety of correlations could be observed as a result of the model predictions. For some samples, the trends follow the expected tendency, backing up the idea of a microstructural gradient across the sample thickness. This is the result of the partition of the alloying elements leading to segregation and also consequence of the thermal gradient produced during the cooling phase. Both effects depend largely on the thickness of the plate and the cooling rate.

In the pearlitic samples, the biggest differences were found at the surface, with the quarter and half thickness positions displaying more uniform properties. This is probably a consequence of the slower cooling rate and higher thickness of these samples compared to the bainitic ones. While the surface inevitably cools down faster, at a quarter and half thickness (around 25 and 50 mm from the surface respectively) a more even distribution of the alloying elements as well as of the heat results in a more uniform microstructure.

The samples classified as bainitic / martensitic are more complex to analyze. Even if the thickness of these plates (23.7 mm) is much smaller than the pearlitic ones, the faster cooling rate leads to more pronounced gradients in the microstructure. Moreover, the limitation of the model to distinguish martensite from bainite is also a limiting factor, as the presence of both constituents is highly likely in these samples. Even the bainitic class itself encompasses a variety of constituents with different properties and morphology.

However, the decision to merge these constituents into the same class responds to the objective of developing a model capable of working on only LOM images. The inherent limitation of this technique regarding the resolving power makes it impossible to distinguish these constituents consistently and reliably, as their features are too small. Nonetheless, by considering this heterogeneous group in a single class, the model is able to produce predictions precise enough to establish correlations between the results and mechanical properties.

Moreover, this is achieved by using only light optical micrographs, without information about the thermal history of the sample or chemical composition. For this reason, the results are still very valuable. However, in order to make a more detailed interpretation of the results, these other

factors cannot be ignored, as they might explain the differences in the trends observed between the samples.

In most samples, larger second phase object areas correlate with increased hardness. Yet, the opposite behaviour might be expected, as smaller objects are more effective barriers to dislocation movement, which translate into a harder material. However, in all cases the area and second phase correlations have the same sign. Therefore, it is possible that the effect of the second phase fraction has a bigger impact on the hardness, making it impossible to separate the effect of the object area. One possible way to further analyze this would be to include more ROI across the sample thickness, to have more data points and calculate a multi variable linear regression model, incorporating a term that accounts for the interaction effect, as shown in equation 4.1.

$$HV = m_1 \cdot SPF + m_2 \cdot A + m_3 \cdot SPF \cdot A + b \tag{4.1}$$

These results validate the idea that is possible to establish correlations between the quantitative evaluations carried out by the machine learning model and the mechanical properties of the steel. This technique ensures that the analysis is done objectively, efficiently, and reproducibly. Further efforts are required to develop an instance segmentation model able to tell apart adjacent objects in order to produce more accurate results, especially regarding the morphological parameters of the particles. Nonetheless, these results by themselves are not only useful but also feasible to implement at an industrial scale.

Chapter 5

Conclusions

Convolutional neural networks have been applied to many different tasks and achieved outstanding performances. The use of data augmentation and application-tailored network architectures has proven that they can also be implemented in fields where the amount of annotated data is limited. In this study, the feature extractor from DenseNet 201 trained with the ImageNet database was successfully employed as encoder for the U-NET architecture. Three generation of models were trained for semantic segmentation of the matrix and second phase objects from two-phase steel light optical micrographs.

Traditional microstructural characterization done by human experts is a complex, time consuming and costly task. Furthermore, as the microstructures continue to become more and more complex, the subjectivity and experience of the metallographer introduces more variance to the results.

To address this issue, several models have been trained and tested. The final model can consistently and objectively segment the microstructure using only light optical micrographs. This is extremely valuable as light optical micrographs are relatively simple and cheap to produce, thus making it feasible for implementation on an industrial scale.

The incorporation of industrial data to the models together with the variance introduced by the images taken with different microscopes, cameras and acquisition conditions greatly enhanced the robustness and overall performance of the final model. Moreover, the iterative optimization approach, with the utilization of the segmentation results as masks for the training of the next generation models, proved to be effective and efficient. Not only did this strategy improve the performance, but also reduced the amount of manual annotation necessary, which is both expensive and time consuming. However, it is worth noting that for some images, hand-correction of the masks was still necessary.

The final model was able to successfully segment light optical micrographs from different microscopes and acquisition conditions consistently. A better detection of the second phase objects as well as less variation related to the image acquisition conditions has been observed.

However, there are still cases where the performance is not as good as expected. The segmentation results for 1000x magnification and for high resolution images were not satisfactory. This might be related to the lack of images taken under these conditions in the training data set. Given the observed trend, it is possible that the incorporation of the last results as masks to the training data could lead to further improvement of the model in a subsequent generation.

The results from the model were used to identify and quantify the second phase fraction on unseen samples. Morphological parameters of the objects could also be calculated from the segmentation masks. However, the intrinsic limitation of the semantic segmentation model lies in its

inability to detect adjacent particles as separated. This constrains the representation of individual objects, which is necessary to achieve more accurate and meaningful results.

Nonetheless, a correlation between the hardness, the second phase fraction and mean object area could be determined. The results were accurate enough to detect variations in the microstructure across the plate thickness, which originate due to segregation and cooling dynamics. This backs up the idea that it is possible to use the results from the model for correlation with mechanical properties. On the same line, the results may also be used for correlation with thermomechanical treatment parameters, thus providing valuable information in the ever-changing industrial processes.

The next logical step in the model development would be to incorporate the results from the last iteration as masks to train a new generation, trying to improve the performance, especially in high magnification and high-resolution images. In addition to this, the next challenge in computer vision artificial intelligence applied to microstructural analysis is to develop an instance segmentation model, aiming to increase the precision in the morphological parameters' measurement. Lastly, the combination of this model with a grain boundary detection model could contribute to a more integral understanding of the microstructure.

At the same time, the possibility of including more ROIs across the sample thickness is a promising approach to further test the model predictions, trying to establish more complex correlations with the hardness. On the same direction, the realization of other mechanical tests on the samples might be useful to test the validity of other parameters such as the axial ratio and orientation of the second phase objects.

The implementation of artificial intelligence in the materials science field has already proved to be very valuable and still has a lot of room for further development and improvement. These models constitute only a demonstration of what these techniques can accomplish.

Machine learning is a powerful tool to visualize, process and interpret data. In this context, it can act as a link between the microstructure, the processing steps, the chemical composition, and more importantly, the steel properties.

The importance of these developments lies not only in the possibility to automate work, but also in making microstructural characterization more objective, consistent, and efficient. Moreover, the rapid development of these techniques can also lead to the establishment of unseen correlations, making it possible to innovate in steel processing and product development.

Bibliography

[1] "World Steel Association." https://worldsteel.org/, accessed 2024-02-16.

[2] P. Hodgson, I. Timokhina, and H. Beladi, "Multiscale microstructure engineering of steels," *Materials science and technology*, vol. 29, pp. 1152–1157, 10 2013.

[3] M. Militzer and T. Garcin, *Microstructure Engineering of High-Performance Steels.* 1 2018.

[4] K. Tsutsui, H. Terasaki, K. Uto, T. Maemura, S. Hiramatsu, K. Hayashi, K. Moriguchi, and S. Morito, "A methodology of steel microstructure recognition using SEM images by machine learning based on textural analysis," *Materials Today Communications*, vol. 25, p. 101514, 12 2020.

[5] M. Müller, D. Britz, T. Staudt, and F. Mücklich, "Microstructural classification of Bainitic subclasses in Low-Carbon Multi-Phase steels using machine learning techniques," *Metals*, vol. 11, p. 1836, 11 2021.

[6] B.-I. Bachmann, M. Müller, D. Britz, A. R. Durmaz, M. Ackermann, O. Shchyglo, T. Staudt, and F. Mücklich, "Efficient reconstruction of prior austenite grains in steel from etched light optical micrographs using deep learning and annotations from correlative microscopy," *Frontiers in materials*, vol. 9, 10 2022.

[7] M. Müller, D. Britz, L. Ulrich, T. Staudt, and F. Mücklich, "Classification of Bainitic structures using textural parameters and machine learning techniques," *Metals*, vol. 10, p. 630, 5 2020.

[8] S. M. Azimi, D. Britz, M. Engstler, M. Fritz, and F. Mücklich, "Advanced Steel microstructural classification by deep learning methods," *Scientific reports*, vol. 8, 2 2018.

[9] O. Theobald, *Machine learning for absolute beginners.* Independently Published, 1 2018.

[10] J. Gola, J. Webel, D. Britz, A. Guitar, T. Staudt, M. Winter, and F. Mücklich, "Objective microstructure classification by support vector machine (SVM) using a combination of morphological parameters and textural features for low carbon steels," *Computational Materials Science*, vol. 160, pp. 186–196, 4 2019.

[11] H. Bhadeshia and R. Honeycombe, *Steels: Microstructure and properties.* Butterworth-Heinemann, 1 2017.

[12] R. W. Hertzberg, R. P. Vinci, and J. L. Hertzberg, *Deformation and Fracture Mechanics of Engineering Materials, 5th Edition.* Wiley, 4 2012.

[13] K.-E. Thelning, *Steel and its heat treatment.* Butterworth-Heinemann, 10 1984.

[14] "Wikipedia." /https://en.wikipedia.org/wiki/Steel accessed 2024-04-05.

[15] G. Thewlis, "Classification and quantification of microstructures in steels," *Materials Science and Technology*, vol. 20, pp. 143–160, 2 2004.

[16] S. Zając, V. Schwinn, and K.-H. Tacke, "Characterisation and quantification of complex Bainitic microstructures in High and Ultra-High Strength Linepipe Steels," *Materials Science Forum*, vol. 500-501, pp. 387–394, 11 2005.

[17] H. K. D. H. Bhadeshia, "The Bainite Transformation: Unresolved issues," *Materials Science and Engineering: A*, vol. 273-275, pp. 58–66, 12 1999.

[18] D. Porter and K. E. Easterling, *Phase Transformations in Metals and Alloys (Revised Reprint)*. 2 2009.

[19] J. D. Verhoeven, *Steel metallurgy for the Non-Metallurgist*. ASM International eBooks, 11 2007.

[20] A. Streißelberger and V. V. Schwinn, "Die Grobblechherstellung aus verfahrenstechnischer Sicht," *Dillinger Hütte*.

[21] D. Li, L. Qing-Liang, and T. Emi, "Microstructure and mechanical properties in Hot-Rolled extra High-Yield-Strength steel plates for offshore structure and shipbuilding," *Metallurgical and materials transactions. A, Physical metallurgy and materials science*, vol. 42, pp. 1349–1361, 12 2010.

[22] C. Beckermann, *Macrosegregation*. 1 2001.

[23] F. Guo, X. Wang, W. Liu, S. Chen, R. Misra, H. Wang, T. Zhao, and C. Peng, "The influence of centerline segregation on the mechanical performance and microstructure of X70 pipeline steel," *Steel research international*, vol. 89, 10 2018.

[24] B. L. Bramfitt and A. O. Benscoter, *Metallographer's Guide: Practices and Procedures for irons and Steels*. ASM international, 12 2001.

[25] "Zeiss Campus: Education in Microscopy and Digital Imaging." https://zeiss-campus.magnet.fsu.edu/articles/basics/reflected.html accessed 2024-04-20.

[26] "University of Cambridge: Dissemination of IT for the Promotion of Materials Science." https://www.doitpoms.ac.uk/tlplib/optical-microscopy/preparation.php accessed 2024-04-20.

[27] N. Yamamoto, *Analytical methods*. 1 2023.

[28] H. Xu, G. Zhai, X. Wu, and X. Yang, "Generalized Equalization model for image enhancement," *IEEE transactions on multimedia*, vol. 16, pp. 68–82, 1 2014.

[29] "Leica: Technical Terms for Digital Microscope Cameras and Image Analysis." https://www.leica-microsystems.com/science-lab/microscopy-basics/technical-terms-for-digital-microscope-cameras-and-image-analysis/ accessed 2024-04-09.

[30] M. Müller, D. Britz, and F. Mücklich, "Machine Learning for Microstructure Classification: How to assign the ground truth in the most objective way," *Advanced materials and processes*, vol. 179, 1 2021.

[31] B. J. Griffin, "A comparison of conventional Everhart-Thornley style and in-lens secondary electron detectors—a further variable in scanning electron microscopy," *Scanning*, vol. 33, pp. 162–173, 5 2011.

[32] P. E. Rossi, "Quantitative Classification and Assessment of Modification in Hypoeutectic Aluminum-Silicon Alloys," 2015.

[33] ASTM E562-19, "Standard Test Method for Determining Volume Fraction by Systematic Manual Point Count," 2019.

[34] G. V. Voort, "Using microstructural analysis to solve practical problems," *Tech-Notes*, vol. 1, no. 5, 1997.

[35] P. K. Sahoo, S. Soltani, and A. Wong, "A survey of thresholding techniques," *Computer vision, graphics, and image processing*, vol. 41, pp. 233–260, 2 1988.

[36] P. Yang, W. Song, X. Zhao, R. Zheng, and L. Qingge, "An improved Otsu threshold segmentation algorithm," *International journal of computational science and engineering*, vol. 22, p. 146, 1 2020.

[37] A. L. Samuel, "Some studies in machine learning using the game of checkers," *IBM journal of research and development*, vol. 3, pp. 210–229, 7 1959.

[38] R. Y. Choi, A. S. Coyner, J. Kalpathy-Cramer, M. F. Chiang, and J. P. Campbell, "Introduction to machine learning, neural networks, and deep learning.," *Translational Vision Science & Technology*, vol. 9, p. 14, 1 2020.

[39] A. Géron, *Hands-On machine Learning with SciKit-Learn and TensorFlow: Concepts, tools, and techniques to build intelligent systems.* O'Reilly Media, 3 2017.

[40] S. Ghosh, N. Das, I. Das, and U. Maulik, "Understanding deep learning techniques for image segmentation," *ACM Computing Surveys*, vol. 52, pp. 1–35, 8 2019.

[41] A. García-García, S. Orts-Escolano, S. Oprea, V. Villena-Martínez, and J. García-Rodríguez, "A review on deep learning techniques applied to semantic segmentation.," *arXiv (Cornell University)*, 4 2017.

[42] K. O'Shea and R. Nash, "An introduction to convolutional neural networks," *arXiv (Cornell University)*, 11 2015.

[43] G. Huang, Z. Liu, L. Van Der Maaten, and K. Q. Weinberger, "Densely Connected Convolutional Networks," *arXiv (Cornell University)*, 8 2016.

[44] J. Deng, W. Dong, R. Socher, L. Li, K. Li, and F. Li, "ImageNet: A large-scale hierarchical image database," *2009 IEEE Conference on Computer Vision and Pattern Recognition*, 6 2009.

[45] O. Ronneberger, P. Fischer, and T. Brox, "U-NET: Convolutional Networks for Biomedical Image Segmentation," *arXiv (Cornell University)*, 5 2015.

[46] S. Napel, W. Mu, B. V. Jardim-Perassi, H. J. Aerts, and R. J. Gillies, "Quantitative imaging of cancer in the postgenomic era: Radio(geno)mics, deep learning, and habitats," *Cancer*, vol. 124, pp. 4633–4649, 11 2018.

[47] "Segmentation Models documentation." https://github.com/qubvel/segmentationmodels, accessed 2024-03-01.

[48] "Albumentations documentation." https://albumentations.ai/docs/, accessed 2024-03-05.

[49] S. C. Wong, A. Gatt, V. Stamatescu, and M. D. McDonnell, "Understanding Data Augmentation for Classification: When to Warp?," *IEEE*, 11 2016.

[50] S. Minaee, Y. Boykov, F. Porikli, A. Plaza, N. Kehtarnavaz, and D. Terzopoulos, "Image segmentation using Deep Learning: A survey," *IEEE transactions on pattern analysis and machine intelligence*, p. 1, 1 2021.

[51] K. Choudhary, B. DeCost, C. Chen, A. Jain, F. Tavazza, R. Cohn, C. WooPark, A. Choudhary, A. Agrawal, S. J. L. Billinge, E. Holm, S. P. Ong, and C. Wolverton, "Recent advances and applications of deep learning methods in materials science," *npj computational materials*, vol. 8, 4 2022.

[52] M. Müller, M. Stiefel, B.-I. Bachmann, D. Britz, and F. Mücklich, "Overview: Machine learning for segmentation and classification of complex steel microstructures," *Metals*, vol. 14, p. 553, 5 2024.

[53] H. Eshet, R. Z. Khaliullin, T. D. Kühne, J. Behler, and M. Parrinello, "Ab initioquality neural-network potential for sodium," *Physical review. B, Condensed matter and materials physics*, vol. 81, 5 2010.

[54] L. Ward, R. Liu, A. Krishna, V. I. Hegde, A. Agrawal, A. Choudhary, and C. Wolverton, "Including crystal structure attributes in machine learning models of formation energies via Voronoi tessellations," *Physical review. B./Physical review. B*, vol. 96, 7 2017.

[55] J. Schmidt, M. R. G. Marques, S. Botti, and M. A. L. Marques, "Recent advances and applications of machine learning in solid-state materials science," *npj computational materials*, vol. 5, 8 2019.

[56] Y. Suzuki, H. Hino, T. Hawai, K. Saito, M. Kotsugi, and K. Ono, "Symmetry prediction and knowledge discovery from X-ray diffraction patterns using an interpretable machine learning approach," *Scientific reports*, vol. 10, 12 2020.

[57] E. A. Holm, R. Cohn, N. Gao, A. R. Kitahara, T. P. Matson, B. Lei, and S. R. Yarasi, "Overview: Computer Vision and Machine learning for microstructural characterization and analysis," *Metallurgical and materials transactions. A, Physical metallurgy and materials science*, vol. 51, pp. 5985–5999, 9 2020.

[58] R. Sawada, Y. Iwasaki, and M. Ishida, "Boosting material modeling using game tree search," *Physical review materials*, vol. 2, 10 2018.

[59] C. Zingarelli, "Aplicación de una metodología de machine learning para optimizar el proceso de fabricación aditiva," 2022.

[60] F. Jaime and T. Martinez Ostormujof, "Automatic detection of second phases in ferritic steels by means of support vector machines," 2019.

[61] J. Vega, "Design and training of bainite and martensite object classifiers using machine learning," 2023.

[62] B.-I. Bachmann, "Prozess-Gefüge-Eigenschaftskorrelationen an ATP blechen mit modernen Methoden der Gefügeanalyse unter Zuhilfenahme von maschinellem Lernen," 2021.

[63] "Dillinger Hütte Webpage." https://www.dillinger.de/referenzen/ accessed 2024-05-17.

[64] G. A. Castello Branco, "Effect of thermo-mechanical treatment on texture evolution of poly-crisstalline alpha titanium," 2005.

[65] B. Denkena and H. K. Tönshoff, *Schleifen.* 1 2011.

[66] M. Murakami, Y. Takanaga, N. Nakada, T. Tsuchiyama, and S. Takaki, "Microstructure and mechanical property of copper bearing eutectoid steel," *ISIJ international*, vol. 48, pp. 1467–1472, 1 2008.

[67] Sternberg, "Biomedical image processing," *IEEE Computer*, vol. 16, pp. 22–34, 1 1983.

[68] Y. Zheng, R. Speller, and J. Griffiths, "A novel method to remove the background from x-ray diffraction signal," *Physics in medicine & biology/Physics in medicine and biology*, vol. 63, p. 06NT03, 3 2018.

[69] "GIMP software." https://www.gimp.org/, accessed 2024-03-18.

[70] "skimage.measure 0.22.0 documentation." https://scikit-image.org/docs/stable/api/skimage.measure.html, accessed 2024-02-19.

[71] ASTM E92-17, "Standard Test Methods for Vickers Hardness and Knoop Hardness of Metallic Materials," 2017.

[72] Q. Zhou, W. Yang, G. Gao, W. Ou, H. Lu, J. Chen, and L. J. Latecki, "Multi-scale deep context convolutional neural networks for semantic segmentation," *World wide web (Print)*, vol. 22, pp. 555–570, 4 2018.

[73] "Zeiss: AxioCAM HR datasheet."

[74] H. Li, T. Li, M. Gong, Z. Wang, and G. Wang, "Finite Element Analysis of Dynamic Recrystallization of Casting Slabs during Hot-Core Heavy Reduction Rolling Process," *Metals*, vol. 10, p. 181, 1 2020.

[75] H. Ashrafi, M. Shamanian, R. Emadi, and N. Saeidi, "Correlation of Tensile Properties and Strain Hardening Behavior with Martensite Volume Fraction in Dual-Phase Steels," *Transactions of the Indian Institute of Metals*, vol. 70, pp. 1575–1584, 9 2016.

[76] B. E. Q'Donnelly, R. L. Reuben, and T. N. Baker, "Quantitative assessment of strengthening parameters in ferrite-pearlite steels from microstructural measurements," *Metals technology*, vol. 11, pp. 45–51, 1 1984.

Appendices

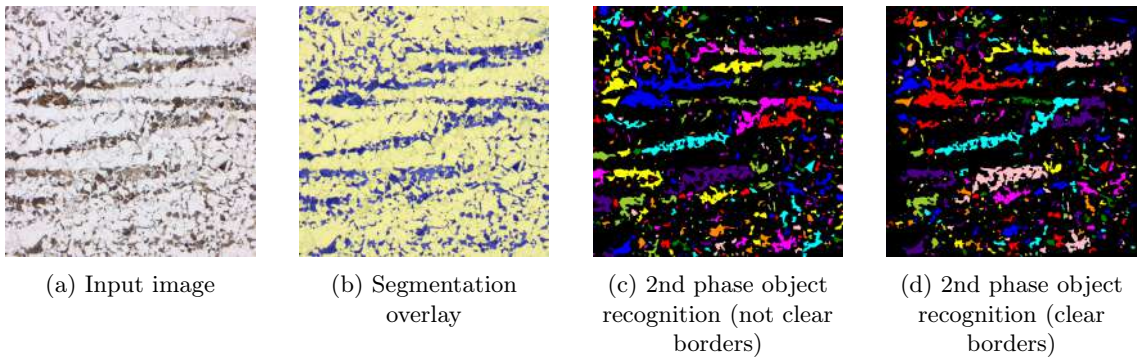# I Complete report of results for the sample C925

(a) Input image

(b) Segmentation overlay

(c) 2nd phase object recognition (not clear borders)

(d) 2nd phase object recognition (clear borders)

Figure 1: Model results. Sample C925, 200x magnification, surface, Zeiss Axio Imager.M2m, optimal imaging settings.

(a) Input image

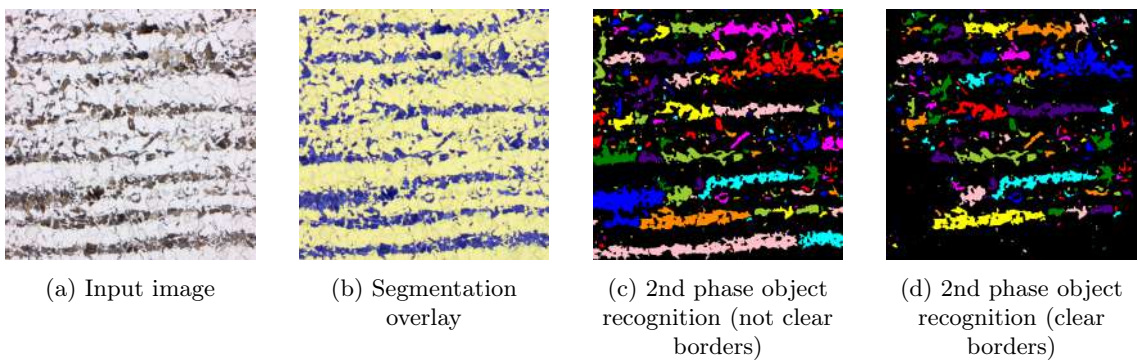(b) Segmentation overlay

(c) 2nd phase object recognition (not clear borders)

(d) 2nd phase object recognition (clear borders)

Figure 2: Model results. Sample C925, 200x magnification, quarter thickness, Zeiss Axio Imager.M2m, optimal imaging settings.

(a) Input image

(b) Segmentation overlay

(c) 2nd phase object recognition (not clear borders)

(d) 2nd phase object recognition (clear borders)
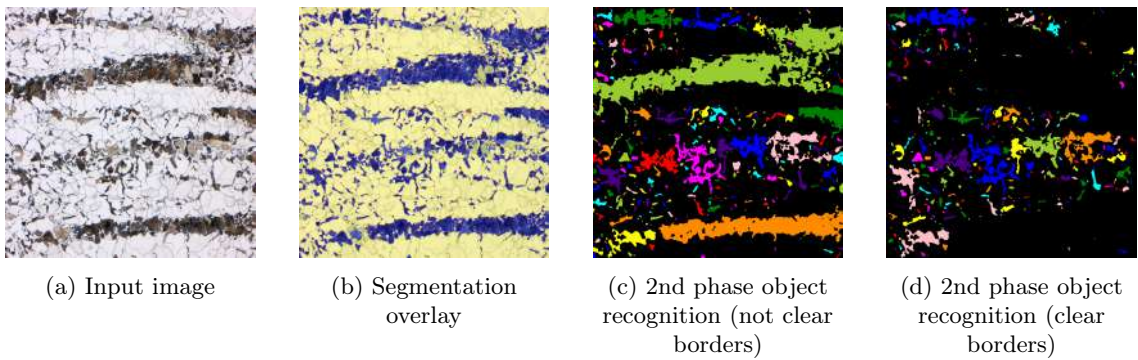
Figure 3: Model results. Sample C925, 200x magnification, half thickness, Zeiss Axio Imager.M2m, optimal imaging settings.

Table 1: Second phase fraction segmentation results. Sample C925, 200x magnification, Zeiss Axio Imager.M2m, optimal imaging settings.

Position	Image number	Matrix	Pearlite	Bainite / martensite
S	1	0.682	0.318	0
	2	0.725	0.274	0
	3	0.767	0.233	0
	4	0.73	0.27	0
Q	1	0.712	0.288	0
	2	0.69	0.31	0
	3	0.72	0.28	0
	4	0.75	0.25	0
H	1	0.761	0.238	0
	2	0.759	0.237	0.004
	3	0.72	0.279	0.001
	4	0.742	0.257	0

Table 2: Quantitative analysis. Sample C925, not clear borders

|	Surface	Quarter	Half
Segmentation 2nd phase fraction	0.27 ± 0.03	0.28 ± 0.02	0.25 ± 0.02
Manual Point Count Second phase fraction	0.32 ± 0.02	0.30 ± 0.05	0.29 ± 0.02
Hardness	150.90 ± 3.62	146.30 ± 2.49	138.00 ± 3.95
Area	100.21 ± 554.95	167.32 ± 873.35	110.5 ± 687.66
Convex Area	184.74 ± 1239.01	303.32 ± 1755.83	197.28 ± 1448.57
Equivalent Diameter	7.05 ± 8.83	7.73 ± 12.38	7.39 ± 9.28
Major Axis Length	12.71 ± 25.15	15.18 ± 38.16	13.6 ± 25.81
Minor Axis Length	5.56 ± 6.85	5.81 ± 8.35	5.84 ± 7.15
Perimeter	44.17 ± 158.14	59.19 ± 226.01	44.93 ± 139.12
Filled Area	103.33 ± 598.95	174.56 ± 934.28	112.83 ± 719.26
Max Feret	12.52 ± 23.62	14.8 ± 34.84	13.43 ± 24.16
Solidity	0.86 ± 0.13	0.86 ± 0.13	0.84 ± 0.14
Eccentricity	0.79 ± 0.15	0.79 ± 0.15	0.81 ± 0.15
Orientation	0.0 ± 0.97	-0.06 ± 0.97	-0.01 ± 0.94
Convex Perimeter	8.4 ± 12.84	9.36 ± 17.28	8.88 ± 13.13
Axial Ratio	2.05 ± 0.93	2.1 ± 1.14	2.21 ± 1.14
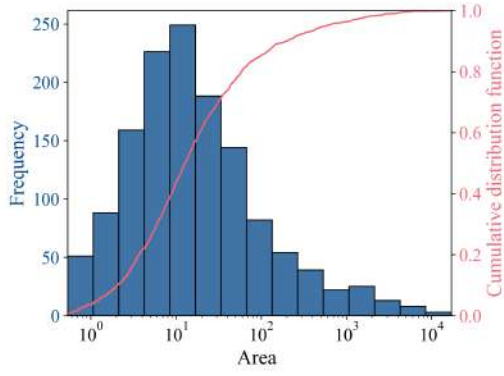
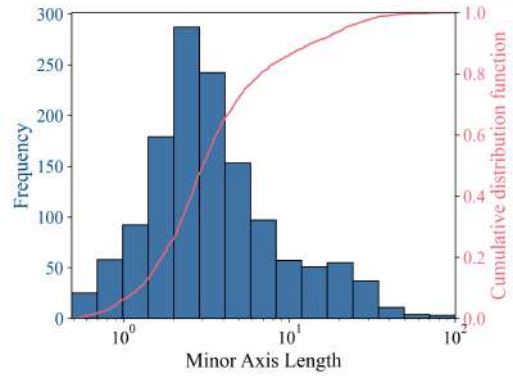(a) Area
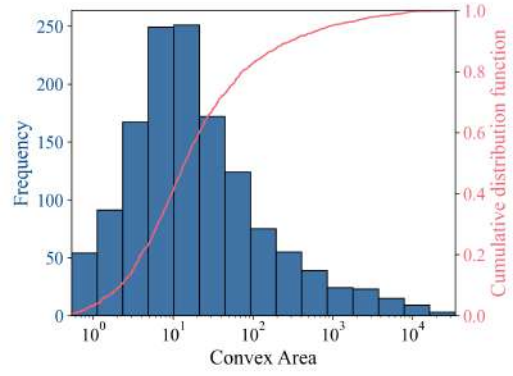
(b) Convex Area
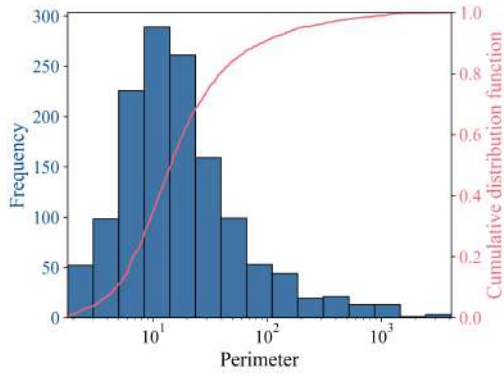
(c) Perimeter
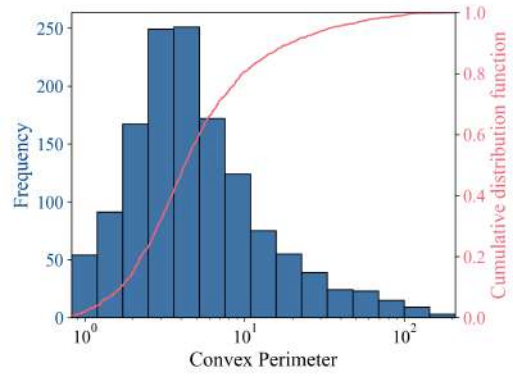
(d) Convex perimeter
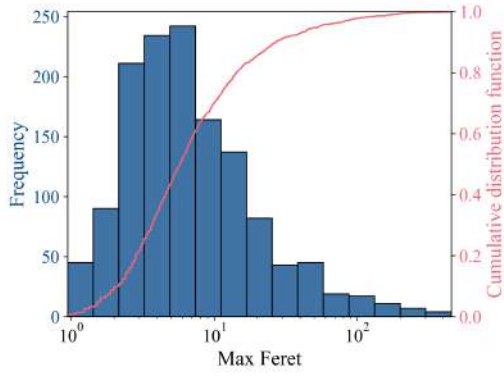
(e) Max Feret diameter
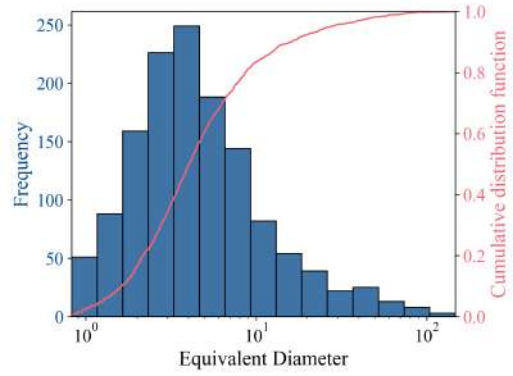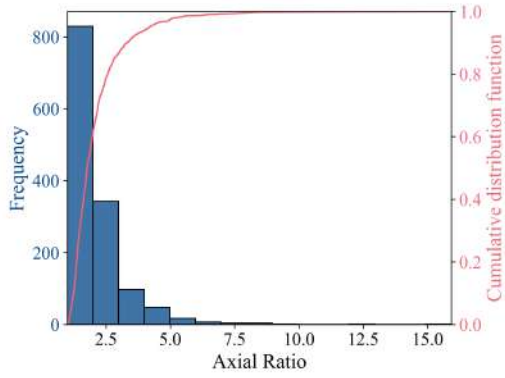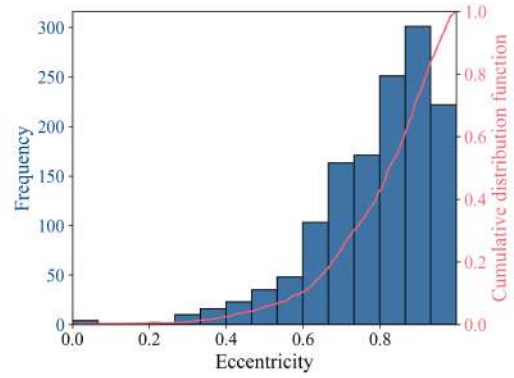
(f) Equivalent diameter
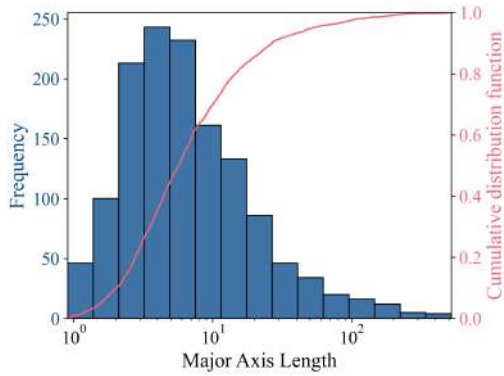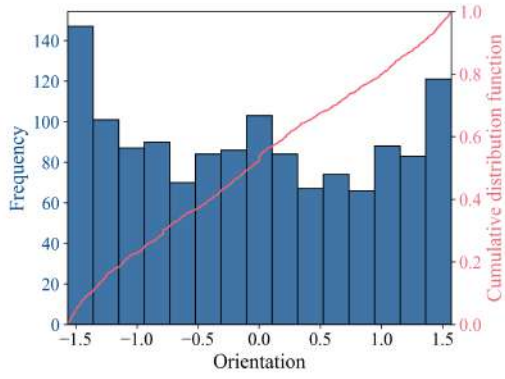
(g) Major axis length

(h) Minor axis length

Figure 4: Morphological parameter distribution plots. Sample C925, quarter thickness, not clear borders.
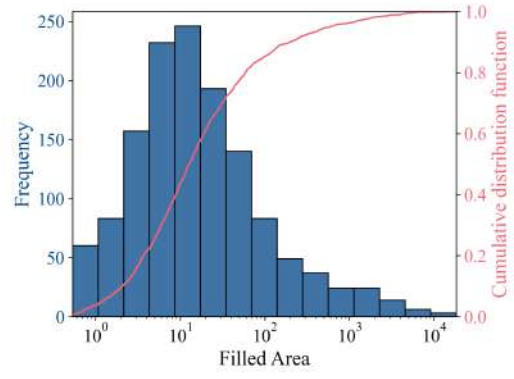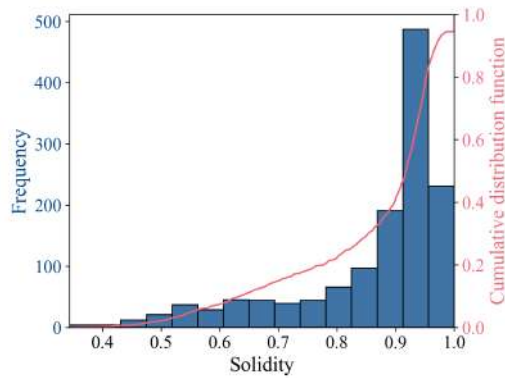
(i) Axial ratio

(j) Eccentricity

(k) Orientation

(l) Filled area

(m) Solidity

Figure 4: Morphological parameter distribution plots. Sample C925, quarter thickness, not clear borders. (cont.)